Order Number 9411811

Studies of magnetic vortices in superconductor networks and clusters by scanning SQUID microscopy

Vu, Lan Ngoc, Ph.D.

University of Illinois at Urbana-Champaign, 1993

U·M·I
300 N. Zeeb Rd.
Ann Arbor, MI 48106

STUDIES OF MAGNETIC VORTICES IN SUPERCONDUCTOR NETWORKS AND CLUSTERS BY SCANNING SQUID MICROSCOPY

BY

LAN NGOC VU

B.S., The University of Texas at Austin, 1987
M.S., University of Illinois at Urbana-Champaign, 1990

THESIS

Submitted in partial fulfillment of the requirements
for the degree of Doctor of Philosophy in Physics
in the Graduate College of the
University of Illinois at Urbana-Champaign, 1993

Urbana, Illinois

UNIVERSITY OF ILLINOIS AT URBANA-CHAMPAIGN

THE GRADUATE COLLEGE

JULY 1993

WE HEREBY RECOMMEND THAT THE THESIS BY

Lan Ngoc Vu

ENTITLED Studies of Magnetic Vortices in Superconductor Networks and Clusters by Scanning Squid Microscopy

BE ACCEPTED IN PARTIAL FULFILLMENT OF THE REQUIREMENTS FOR

THE DEGREE OF Doctor of Philosophy

Director of Thesis Research

Head of Department

Committee on Final Examination†

Chairperson

† Required for doctor's degree but not for master's.

O-517

STUDIES OF MAGNETIC VORTICES IN SUPERCONDUCTOR NETWORKS AND CLUSTERS BY SCANNING SQUID MICROSCOPY

Lan Ngoc Vu, Ph.D.
Department of Physics
University of Illinois at Urbana-Champaign, 1993
Dale J. Van Harlingen, Advisor

We have developed a Scanning SQUID Microscope (SSM) to study the configuration of trapped magnetic vortices in two-dimensional superconductor arrays and clusters. The SSM scans a dc SQUID detector over the array surface, achieving better than 10μm spatial resolution over a scan range up to 1cm x 1cm and a magnetic flux sensitivity of about $10^{-4}\Phi_0$. We have obtained images of large square arrays cooled at different values of applied magnetic flux per cell Φ. For low rational values (1/2, 2/5, 1/3, 1/4, ...) of the frustration parameter $f \equiv \Phi/\Phi_0$, we find regions of periodically-arranged vortices separated by domain walls; at other values of the field, the vortex pattern is disordered. We also present observations of trapped vortex-antivortex pairs in arrays and vortex patterns in ensembles of 1x1, 2x2, and 3x3 clusters. The physics of clusters can be explained by statistical processes. Dynamics of vortices in large arrays by current injection have also been investigated. As the array is current biased, most vortices are pinned to the grids with a few vortices hopping perpendicular to the direction of current due to the Lorentz force. Some vortices move in parallel and anti-parallel to the direction of current. Creation and annihilation of vortex-antivortex pairs are also observed.

To my parents

ACKNOWLEDGMENTS

This thesis would never have been completed without the help and guidance of my advisor, Dale Van Harlingen. He is the kindest and most knowledgeable advisor I have had. He has taught me all the experimental techniques I know.

I would like to thank my lab mates Mark Wistrom, Subashri Rao, Ralph Schweinfurth, Joe Walko, Stuart Tessmer, Dave Wollman, and Joe Tien for helping out so much in my research. Their presence in lab have made research more bearable. Special thanks to Mark Wistrom and Joe Walko for getting my research on track. I also want to thank Suba for proof-reading my thesis.

I am grateful to professor Mochel for many useful discussions and guidance. Others who have helped me in my research include: Fred Sharifi, Xinling, Bud, Darrell, Spencer, Ken, Nick, Cliff, Dick, Bill T., Thao Tran, Ming Tang, Matt Hauser, Fang Yu, and Bill McMahon. I want to thank my social buddies for keeping me from going insane. They are Thao Tran, Hao Tran, Vinh Tat, Nim Tea, Bill McMahon, Eric Hirschhorn, Mark Teepe, B. J. Park, and Mark Wistrom. The gang at Stony Brook during my first year of graduate school deserves special mention. They include Claudio Coriano, Teddy Tse, Felix Liang, Lie Ping, Rajesh Parwani, Jerritt Gluck and Dan Koller. I also want to thank Jeff Shields and Mark Ramsbey for their friendship and their help in getting me a job.

I would like to thank my parents, my brothers (Son, Linh, and Chau) and sister (Quynh) for their love and understandings during my 6 years of graduate school. Without their supports none of these would have been possible.

Finally, I would like to thank Doan Nghiem for her love and encouragement during my last two years at Illinois. Without her, I would have never had the incentive to finish graduate school.

This work is supported by the National Science Foundation under grant NSF-DMR91-15411. I would also like to acknowledge extensive use of the thin film microfabrication facilities of the Federick Seitz Materials Research Laboratory at the University of Illinois.

TABLE OF CONTENTS

Chapter 1

Introduction

In recent years, intense efforts have been made in understanding the superconducting-to-normal transition in weakly-coupled arrays and thin-wire networks of superconductors. Both systems exhibit extremely interesting phase diagrams when a magnetic field is applied. From the application point of view, weakly-coupled arrays and networks are simple models for understanding granular superconductor thin films and high T_c superconducting films[1] (Figure 1.1). Granular and high T_c superconductor thin films are modeled as a random array of superconducting islands, which interact with neighboring islands through Josephson coupling. To the first-order of approximation, the random array can be treated as a periodic array of uniform junction couplings. By understanding the interaction of magnetic vortices in these simple arrays, scientists can gain insight into how films interact with magnetic fields. This knowledge can assist scientists to grow higher quality films and to make better superconducting devices. On the physics side, both arrays and networks are beautiful systems (in the sense that crucial parameters such as critical current, Josephson coupling energy, and geometry can be carefully controlled by microfabrication process) in which to study two-dimensional phase transitions, phase coherence, frustration, commensurability, and vortex dynamics.

In a magnetic field, both the weakly-coupled arrays and wire networks trap magnetic vortices as they are cooled through their transition temperatures. These vortices tend to repel one another and rearrange themselves such that the free energy of the system reaches a minimum. Theorists[2-4] predicted that at T=0K for rational values of f (defined as the frustration parameter $f \equiv \Phi_a/\Phi_0$ where Φ_a is the applied flux per cell and $\Phi_0 \equiv h/2e$ is the flux quantum) the vortices arrange themselves in periodic patterns commensurate with the underlying superconductor lattice. The free energies of theses distributions are lower than

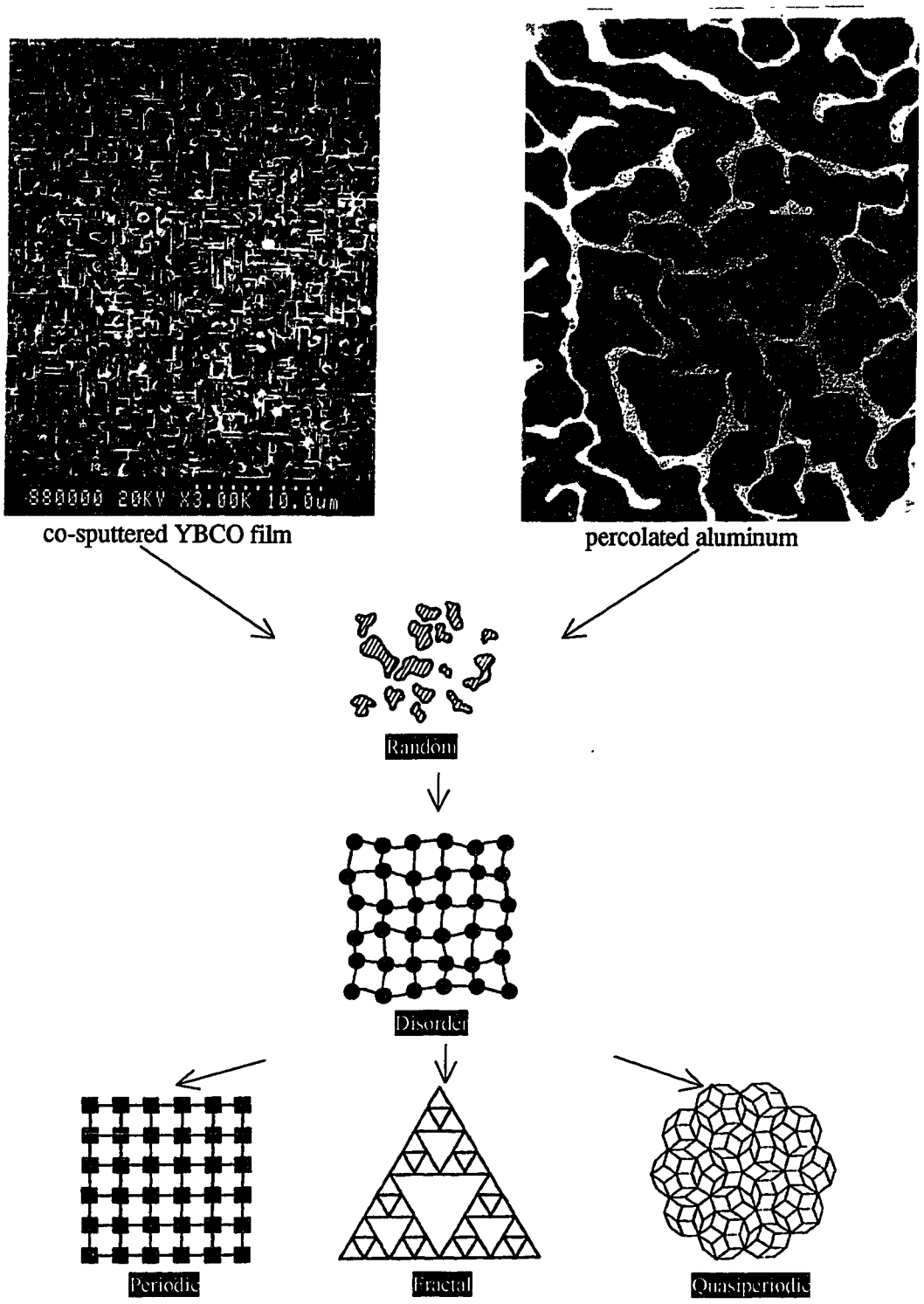

Figure 1.1 : Modeling of high T_C and granular thin film superconductors with superconductor wire networks and weakly-coupled arrays.

alternate metastable configurations. Until recently however, it has not been possible to observe vortices in arrays and networks because the magnetic fields associated with them are weak. Instead, experiments have measured the electronic transport properties that are related to the averaged vortex dynamics of the arrays near the transition temperature.[5-9] Comparison of experiments to theory therefore is difficult. Direct detection of vortex configurations and motion has been a long-standing experimental goal to bridge the gap between theories and experiments of superconductor arrays and networks.

This thesis concentrates on magnetic imaging of vortices in superconducting square wire networks (with a unit cell of 20μm x 20μm) by Scanning SQUID Microscopy (SSM). This novel instrument[10] which we developed utilizes a micro-dc SQUID (Superconducting QUantum Interference Device) that is scanned across the sample surface to detect magnetic field modulations due to trapped vortices. The instrument achieves spatial resolution better than 10μm and has scanning range up to 1cm x 1cm.

There are many existing instruments used to study small magnetic structures but none have the field sensitivity and scanning range to image vortices in our array samples. Nevertheless, it is useful to compare the SSM with other magnetic imaging instruments by their field sensitivity and their spatial resolution and range. In Figure 1.2, we show the regimes covered by several imaging methods that have been used to study magnetic structures in superconductors. In this plot, the product of the field and spatial resolution gives a measure of the flux sensitivity in units of Φ_0. Two of the techniques indicated, scanning tunneling microscope spectroscopy (STM)[11] and scanning electron microscope imaging (SEM)[12], do not directly utilize magnetic field probes: for these we have estimated an effective field sensitivity based on features observed using these techniques. Each approach has advantages and disadvantages for exploration of magnetic phenomena. For example, Bitter decoration by magnetic particles[13] and magneto-optic imaging techniques[14] allow viewing of vortex configurations over large areas, but are limited to

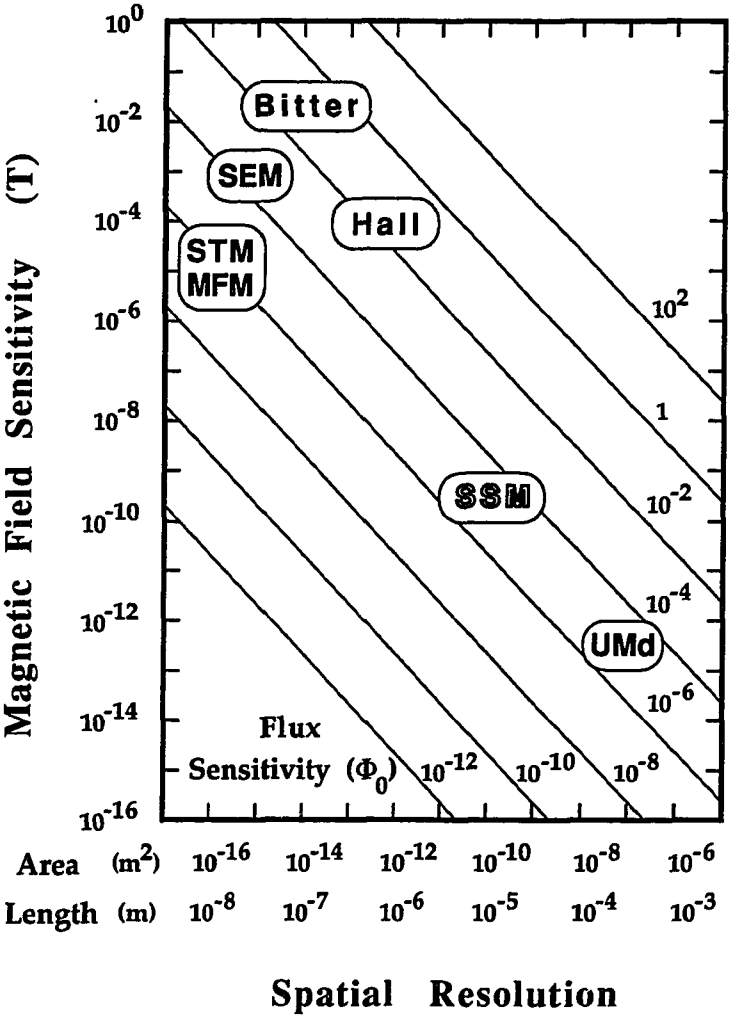

Figure 1.2 : Field sensitivity and spatial resolution attainable by several common magnetic structure imaging techniques and the Scanning SQUID Microscope system described here.

static images and large field modulations. With STM, the structure inside the core of a single vortex can be explored, but the range is limited by piezoelectric extension at low temperature. Newly developed GaAs Hall probes[15] based on 2D electron gas transport can operate over a wide temperature range and can be fabricated with submicron dimensions. The field sensitivity of a GaAs Hall probe is limited to about 0.1Gauss and has been used to image vortices in niobium networks with very small unit cells (~ 0.3μm x 0.3μm) in a narrow scanning range (~ 10μm x 10μm). Magnetic force microscopy (MFM) is capable of atomic resolution, but due to low field sensitivity has mostly been used to study high field magnetic domain structure.[16] Recently, a group at Hitachi[17] has used the technique of Lorentz microscopy to study of vortex motion in real time in niobium films. This impressive technique is capable of imaging Abrikosov vortices of size ~0.1μm in diameter over 50μm x 50μm areas at 30 frames/second. SQUIDs on the other hand have unparalleled magnetic field sensitivity. This capability has been demonstrated by SQUID imaging techniques in biomagnetism[18] and non-destructive testing[19], but these techniques have not needed nor achieved the spatial resolution required to image vortices in superconductors. A one-dimensional SQUID scanner developed recently at Maryland[20] has achieved spatial resolution of about 200μm with flux sensitivity of $10^{-5}\Phi_0/Hz^{1/2}$, corresponding to an impressive magnetic field sensitivity of $10^{-13}T/Hz^{1/2}$. Our SSM has a similar flux sensitivity but has spatial resolution and range that are capable of detecting magnetic vortices of size 20μm x 20μm in a large wire network of 500 cells x 500 cells.

We begin with Chapter 2 discussing the theory, fabrication, and operation of the dc SQUID used as the magnetic field detector. The theory of a single Josephson junction and dc SQUID are based on the resistively shunted junction (RSJ) model and can be understood as a particle in a 1-D and 2-D washboard potential, respectively. We will also discuss our techniques for fabricating dc SQUIDs and superconductor networks. Our dc SQUIDs are made of high quality robust Nb/Al-Al_2O_3/Nb junctions. They are operated in flux-lock

mode with a flux noise sensitivity of $6x10^{-6}\Phi_0/Hz^{1/2}$.

In Chapter 3, we will discuss the physics of large weakly-coupled superconductor arrays and superconductor networks. The weakly-coupled array system is isomorphic to the frustrated XY model with the addition of the phase coherent condition around every closed loop. Superconducting networks near T_c, on the other hand, are described by the Ginzburg-Landau equation. Very near T_c, the linearized mean-field equations describing networks are the same as the weakly-coupled arrays, and the two systems have the same magnetic phase diagrams. Well below T_c, the similarity between networks and weakly-coupled arrays diverges. The network becomes a bulk superconductor grid, with generated screening supercurrents large enough to trap or expel magnetic fields and give rise to actual flux quantization in the cells. In contrast, screening currents in the weakly-coupled array are weak and a trapped vortex is dominated by the phase drops across the junctions so that the actual field associated with a vortex is only about $10^{-3}\Phi_0$. For smaller arrays and networks, which we call clusters, the ground state vortex configurations and energies can be calculated exactly without relying on a mean field approximation. We will show our simulation results for 1x1 and 2x2 clusters. These results will be used later to explain the statistics of the cluster experiment described in chapter 5.

The scanning scheme and the design of the Scanning SQUID Microscope (SSM) are described in Chapter 4. The heart of our scanning scheme is a home-made mylar hinge which allows the SQUID to be within 10μm of the array sample. This idea is similar to the phonographic needle of a record player. The SSM utilizes a simple inverted cryogenic dewar. We will discuss the operation and performance of our prototype, SSM1. A few minor problems in our designs of the SSM1 will be pointed out which are corrected in the second version, the SSM2.

In Chapter 5, we will discuss some vortex imaging results obtained with the SSM1. In our magnetic images, we not only see the trapped vortices but also the underlying

superconductor lattice. We will explain this effect and other interesting features in the image that are inherent in the instrument. We will then show the results of vortex images in a large superconductor square network for different frustration factor f. Results for low rational f = 1/5, 1/4, 1/3, 1/2, 2/5, and 2/3 are shown. The results fit with theory very well except for lower values such as 1/5 and 1/4 which show more disorder. At this field, the energy of the ground state vortex pattern is only slightly lower than alternate metastable configurations so that sample defects and thermal fluctuations cause significant disorder. For values of irrational f, the vortex pattern is random and not commensurate with the lattice. At f=0, we observed vortices and antivortices. Next, we will present results for ensembles of 1x1, 2x2, and 3x3 clusters under different applied f. Using computer simulations of the vortex dynamics in the clusters, we can calculate the free energy curves for each vortex configuration and then calculate the statistics for an ensemble of clusters. Comparison of this modeling with the experiments gives information on the extent of coupling disorder in the clusters and the thermodynamics of the flux trapping process. Finally, we will present data on vortex dynamics in superconductor square networks by current injection. Here we have imaged a vortex pattern (at ~7K) for each different values of current applied to the array. The currents we applied (0μA to 40μA/wire) are well below the critical current of the niobium (~10mA/wire). As expected, most vortices are locked to the grid but a few vortices hopped perpendicular to the direction of applied current (driven by the Lorentz force) into the next cell. We also found vortices which hop along the direction of applied current with no preferential direction. Vortex-antivortex pair creation and annihilation were also observed.

Finally, Chapter 6 suggests some future experiments of vortex imaging which can be done by Scanning SQUID Microscopy. A potential application of the SSM in other non-superconducting systems such as ferromagnetic and diamagnetic will also be discussed.

References

1. For a review of this field, see *Proceedings of the NATO Workshop on Phase Coherencce in Superconductor Networks*, edited by J. E. Mooj and Schön, *Physica B* **152** (1988).

2. S. Teitel and C. Jayaprakash, "Josephson-Junction Arrays in Transverse Magnetic Fields". *Phys. Rev. Lett.*, **51**, 1999-2002 (1983).

3. Wan Y. Shih and D. Stroud, "Molecular-Field Approximation for Josephson-Coupled Superconducting Arrays in a Magnetic Field". *Phys. Rev. B*, **28**, 6575-6577 (1983).

4. Thomas C. Halsey, "Josephson-Junction Arrays in Transverse Magnetic Fields: Ground States and Critical Currents". *Phys. Rev. B*, **31**, 5728-5745 (1985).

5. D. W. Abraham, C. J. Lobb, M. Tinkham, and T. M. Klapwijk, "Resistive Transition in Two-Dimensional Arrays of Superconducting Weak Links". *Phys. Rev. B*, **26**, 5268-5271 (1982).

6. Richard A. Webb, Richard F. Voss, G. Grinstein, and P. M. Horn, "Magnetic Field Behavior of a Josephson-Junction Array: Two-Dimensional Flux Transport of a Periodic Substrate". *Phys. Rev. Lett.*, **51**, 690-693 (1983).

7. B. Pannetier, J. Chaussy, and R. Rammal, "Experimental Fine Tuning of Frustration: Two-Dimensional Superconducting Network in a Magnetic Field". *Phys. Rev. Lett.*, **53**, 1845-1848 (1984).

8. R. K. Brown and J. C. Garland, "Effect of Magnetic-Field-Induced Frustration on the Superconducting Transition of Proximity-Coupled Arrays". *Phys. Rev. B*, **33**, 7827-7829 (1986).

9. D. J. Van Harlingen, K. N. Springer, G. C. Hilton, and J. Tien, "Phase Coherence and Dynamics in Weakly-Coupled Periodic and Quasiperiodic Superconductor Array". *Physica B*, **152**, 134-145 (1988).

10. L. N. Vu and D. J. Van Harlingen, "Design and Implementation of a Scanning SQUID Microscope". *IEEE Trans. Mag.*, Applied Superconductivity Conference ASC 1992 (in print).

11. H. F. Hess, R. B. Robinson, R. C. Dynes, J. M. Valles, Jr., and J. V. Waszczak, "Scanning-Tunneling-Microscope Observation of the Abrikosov Flux Lattice and the Density of States Near and Inside a Fluxoid". *Phys. Rev. Lett.* **62**, 214-216 (1989).

12. H. Boersch, B. Lischke, and H. Sollig, *Phys. Status Solidi B* **61**, 215 (1974).

13. F. Bitter, "On Inhomogeneities in the Magnetization of Ferromagnetic Materials". *Phys. Rev.* **38**, 1903-1905 (1931).

14. H. J. Williams, F. G. Foster, and E. A. Wood, "Observation of Magnetic Domains by the Kerr Effect". *Phys. Rev.* **82**, 119-120 (1951).

15. A. M. Chang, H. Allen, L. Harriott, H. Hess, H. Kao, J. Kwo, R. Miller, R. Wolfe, J. van der Ziel, and T. Chang, "Scanning Hall Probe Microscopy". *Appl. Phys. Lett.* **61**, 1974-1976 (1992).

16. Y. Martin and H. K. Wickramasinghe, "Magnetic Imaging by 'Force Microscopy' with 1000Å Resolution". *Appl. Phys. Lett.* **50**, 1455-1457 (1987).

17. K. Harada, T. Matsuda, J. Bonevich, M. Igarashi, S. Kondo, G. Ponzzi, U. Kawabe, and A. Tonomura, "Real-Time Observation of Vortex Lattices in a Superconductor by Electron Microscopy". *Nature* **360**, 51-53 (1992).

18. H. Weinstock, "A Review of SQUID Magnetometry Applied to Nondestructive Evaluation". *IEEE Trans. Mag.* **27**, 3231-3236 (1991).

19. D. J. Staton, Y. P. Ma, N. G. Sepulveda, and J. P. Wikswo, "High-Resolution Magnetic Mapping Using a SQUID Magnetometer Array". *IEEE Trans. Mag.* **27**, 3237-3240 (1991).

20. A. Mathai, D. Song, Y. Gim, and F. C. Wellstood, "One-Dimensional Magnetic Flux Microscope Based on the DC Superconducting Quantum Interference Device". *Appl. Phys. Lett.* **61**, 598-600 (1992).

Chapter 2

DC SQUIDs

A single vortex trapped in a superconductor loop of 20 μm x 20 μm has a peak magnetic field of about .05 Gauss (Earth field ~ 0.5 Gauss). To be able to detect a field of this size, a very sensitive probe must be used. Microfabricated GaAs Hall probes[1] and magnetic tips[2] in magnetic force microscope (MFM) do not have such sensitivity. The dc SQUID however is capable of detecting a variation in the magnetic field as low as 10^{-7} Gauss. Detecting a single vortex in a superconductor network is therefore easily achievable with a dc SQUID. For weakly-coupled superconductor arrays the magnetic field associated with a single vortex in a cell of the same size is about three orders of magnitude less, ~ 10^{-5} Gauss. This signal is still within the detecting range of the dc SQUID.

The dc SQUIDs we fabricated for our experiment are state-of-the-art niobium planar trilayer SQUIDs.[3] Nb/Al-Al_2O_3/Nb junctions are very robust and can withstand many thermal cyclings without degrading.[4,5] They also have better low noise characteristic and small subgap leakage current because of which niobium SQUIDs are superior to Pb/In SQUIDs.[6] The only disadvantage of niobium dc SQUIDs is that they are very difficult to fabricate. The difficulties in fabricating niobium dc SQUIDs are due to film stress, trilayer deposition, etching, and step coverage. These problems will be addressed in the fabrication section.

2.1 Theory

A thorough understanding of a Josephson junction and phase coherence is needed in understanding the operation of the dc SQUID and the physics of superconducting arrays. The Josephson junction, the dc SQUID, and the array can all be explained by a model of a particle moving in a washboard potential. The potential is a multidimensional function of

the gauge-invariant phase of each junction, ϕ_i . For a system consisting of N junctions such as the weakly-coupled array the washboard potential is just $U(\phi_1,\phi_2,\ldots,\phi_N)$, where ϕ_i is the phase of i^{th} junction.

2.1.1 Single Josephson Junction (JJ)

A Josephson junction is a weak link in a superconductor that obeys the Josephson supercurrent relation (eqn. 2.1). The weak link can either be a thin layer of insulator sandwiched between the two superconductors (SIS junction), a thin normal metal layer (SNS junction) separating the two superconductors, or a microbridge in a thin line of superconductor (see Figure 2.1). In the zero resistance state, a dc supercurrent flows through the junction according to the Josephson relation

$$I_S = I_C \sin \phi \qquad (2.1)$$

where I_C is the critical current of the junction and ϕ is the static gauge-invariant phase difference across the junction. The coupling energy of the junction is given by

$$E_C = - E_J \cos \phi \qquad (2.2)$$

where $E_J = I_C\Phi_O/2\pi$ is defined as the Josephson energy and $\Phi_O = h/2e$ is the magnetic flux quantum. The Josephson coupling energy of each junction can be controlled by adjusting the I_C to a desirable value during the fabrication process. I_C is also a function of temperature, magnetic field, and barrier thickness (in SIS or SNS junctions). If the junction is biased at a voltage V, the phase will evolve in time as follows,

$$\frac{d\phi}{dt} = \frac{2e}{\hbar} V \quad . \qquad (2.3)$$

For a real Josephson junction, there is also an inherent resistance and capacitance associated with the device. This non-ideal JJ can be modeled by a resistively shunted junction (RSJ), shown in Figure 2.2. The model consists of an ideal weak link that obeys the Josephson current relation (eqn. 2.1) in parallel with a resistor and an intrinsic junction capacitance. When the device is biased with a current I, the total current through the RSJ is

$$C\frac{dV}{dt}+\frac{V}{R}+I_c\sin\phi = I \quad . \tag{2.4}$$

Combining eqns. (2.4) and (2.3) we get

$$C\frac{d^2\phi}{dt^2}+\frac{1}{R}\frac{d\phi}{dt}-\frac{2\pi}{\Phi_o}\left(I-I_c\sin\phi\right)=0 \quad . \tag{2.5}$$

Equation 2.5 can be analyzed as a particle of mass C moving in a washboard potential

$$U(\phi) = -E_J\left(\frac{I}{I_c}\phi-\cos\phi\right) \quad . \tag{2.6}$$

At bias current below I_c, the particle is trapped in the well and the voltage across the junction is zero. As current is increased, the washboard potential is tipped. At some point further tipping will cause the particle to roll out of the potential and be in a running state (Figure 2.3). In the running state, the phase is evolving with time which means a finite voltage is developed across the junction. A typical current-voltage (I-V curve) of a SIS Josephson junction is shown in Figure 2.4. Most SIS Josephson junctions have a hysteretic I-V curve due to their high intrinsic R. By shunting the junction with a lower resistor so that the McCumber parameter, $\beta_C \equiv 2\pi I_c R^2 C/\Phi_o < 1$ the junction can be made nonhysteretic.

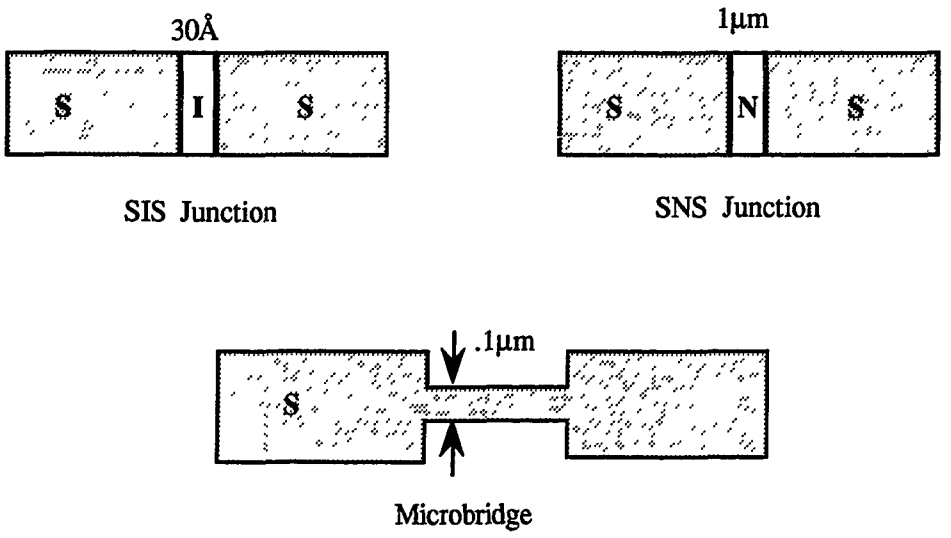

Figure 2.1 : 3 different types of Josephson junctions.

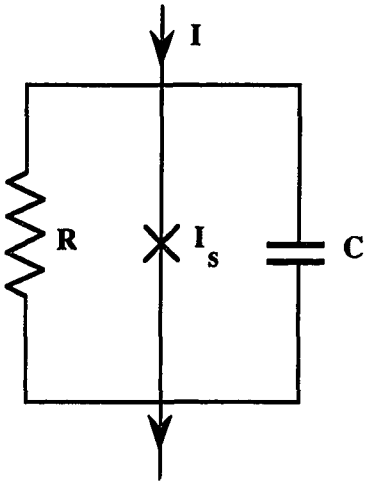

Figure 2.2 : RSJ model of a nonideal Josephson junction.

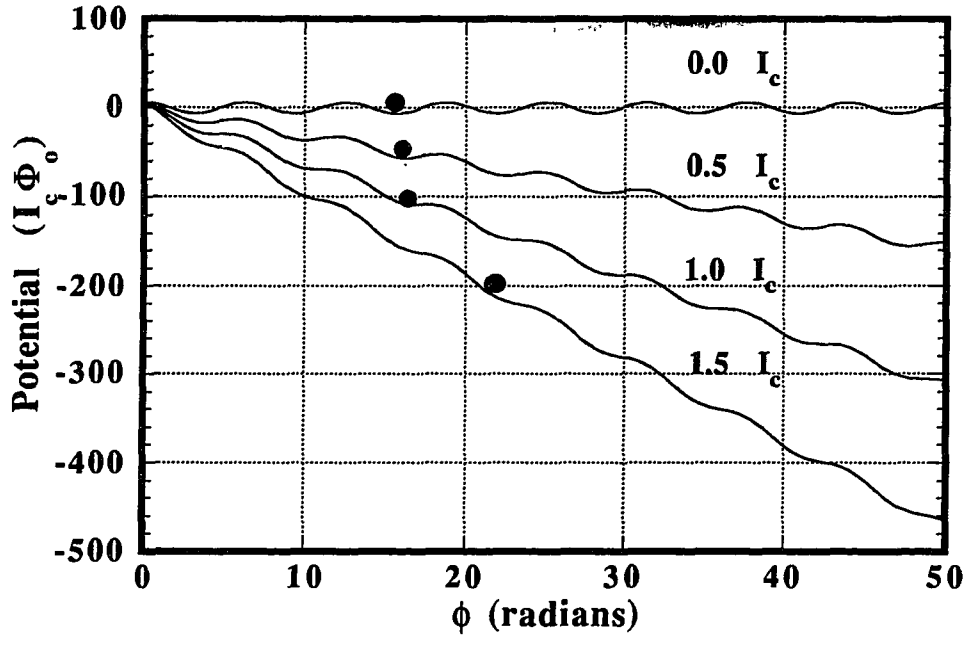

Figure 2.3 : 1-D washboard potential at different bias current.

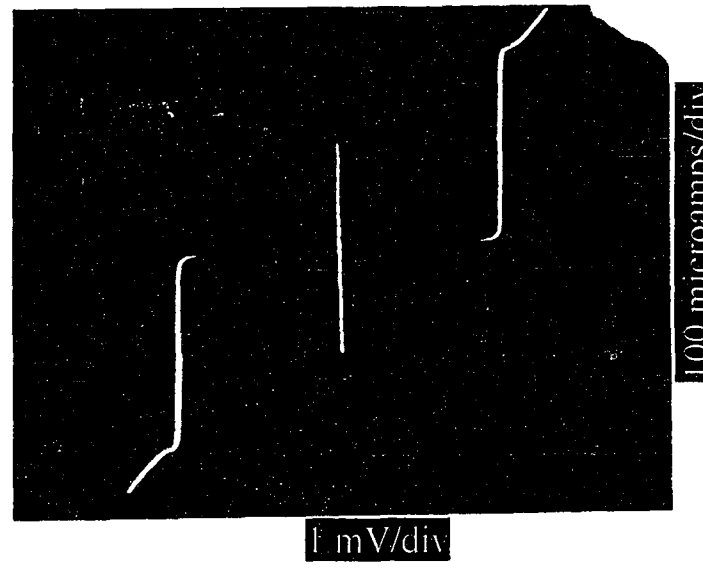

Figure 2.4 : I-V of an unshunted junction of Nb/Al-Al_2O_3/Nb (junction area ~ 25μm^2).

2.1.2 DC SQUID

The dc SQUID consists of two Josephson junctions connected with a superconducting loop. The RSJ model is shown in Figure 2.5. Unlike the junction, the SQUID must obey the phase coherent condition given by

$$2\pi n = \phi_1 - \phi_2 - \frac{2\pi}{\Phi_o}(\Phi_a + LJ) \quad . \qquad (2.7)$$

Φ_a is the applied flux to the SQUID loop, n is any integer, L is the self-inductance of the SQUID, and J is the circulating current in the SQUID. We can again write the equation of motion of the phases of the SQUID like the JJ in eqn. 2.5. Combining this with eqn. 2.7 we find that the phase acts like a particle of mass C moving in a 2-D washboard potential (see Figure 2.6) given by

$$U(\phi_1,\phi_2) = -\frac{I_c\Phi_o}{2\pi}\left[\frac{I}{2I_c}(\phi_1+\phi_2)+\cos\phi_1+\cos\phi_2\right]+\frac{1}{2}LJ^2 \quad . \qquad (2.8)$$

At zero field and bias current below $2I_c$, the particle is trapped in a well of a 2-D washboard potential, and the voltage across the SQUID is zero. However, by applying a current to the SQUID, the washboard potential can be tipped. Increasing the current above $2I_c$ will cause the particle to be in the running state. Applying a magnetic field (changing the $(1/2)LJ^2$ term) would not tip the washboard potential but would change the height of the minima and maxima in the 2-D potential. Increasing the applied field can make some local minima in the potential disappear and cause a particle to fall into the nearest minima.

A typical I-V curve for a shunted SQUID fabricated in our lab is shown in Figure 2.7 along with its V vs. Φ_a curve. The derivative of this curve, $dV/d\Phi$, is the transfer function and its maximum is of order R/L .[7] To operate the magnetic sensor at maximum sensitivity, the SQUID must be biased at its maximum transfer function. The

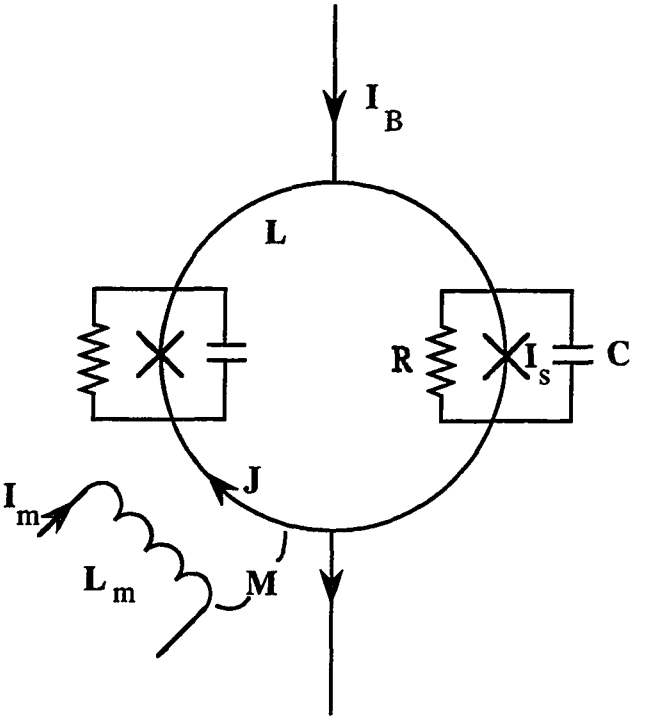

Figure 2.5 : RSJ model of the dc SQUID with modulation coil.

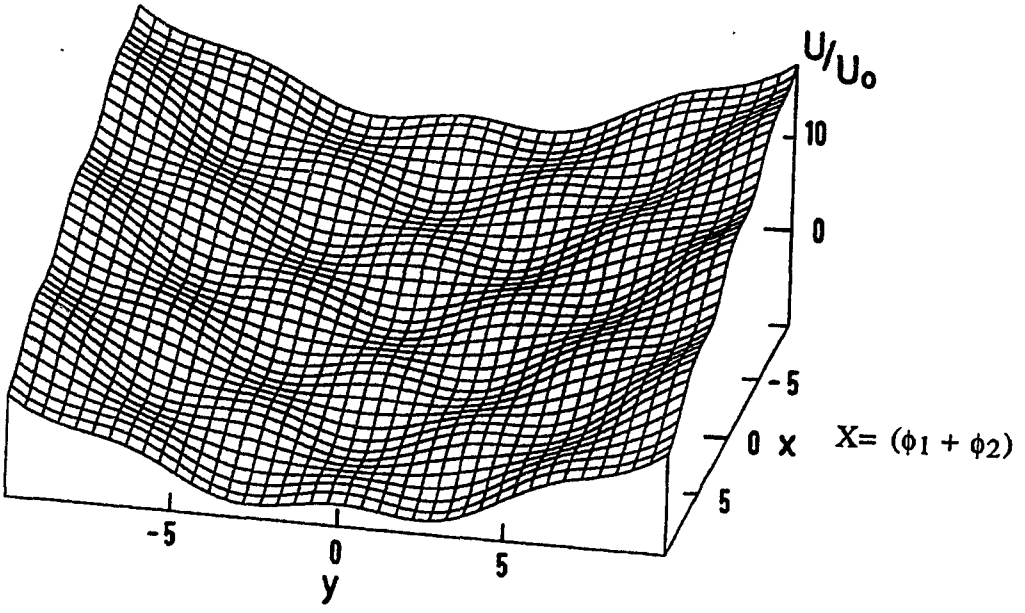

$I = 0.85\ (2I_c)$; $U_o = 2I_c\Phi_o/2\pi$; $\Phi_a = 0$; $\beta_L = 10\pi$

Figure 2.6 : 2-D washboard potential for the dc SQUID.

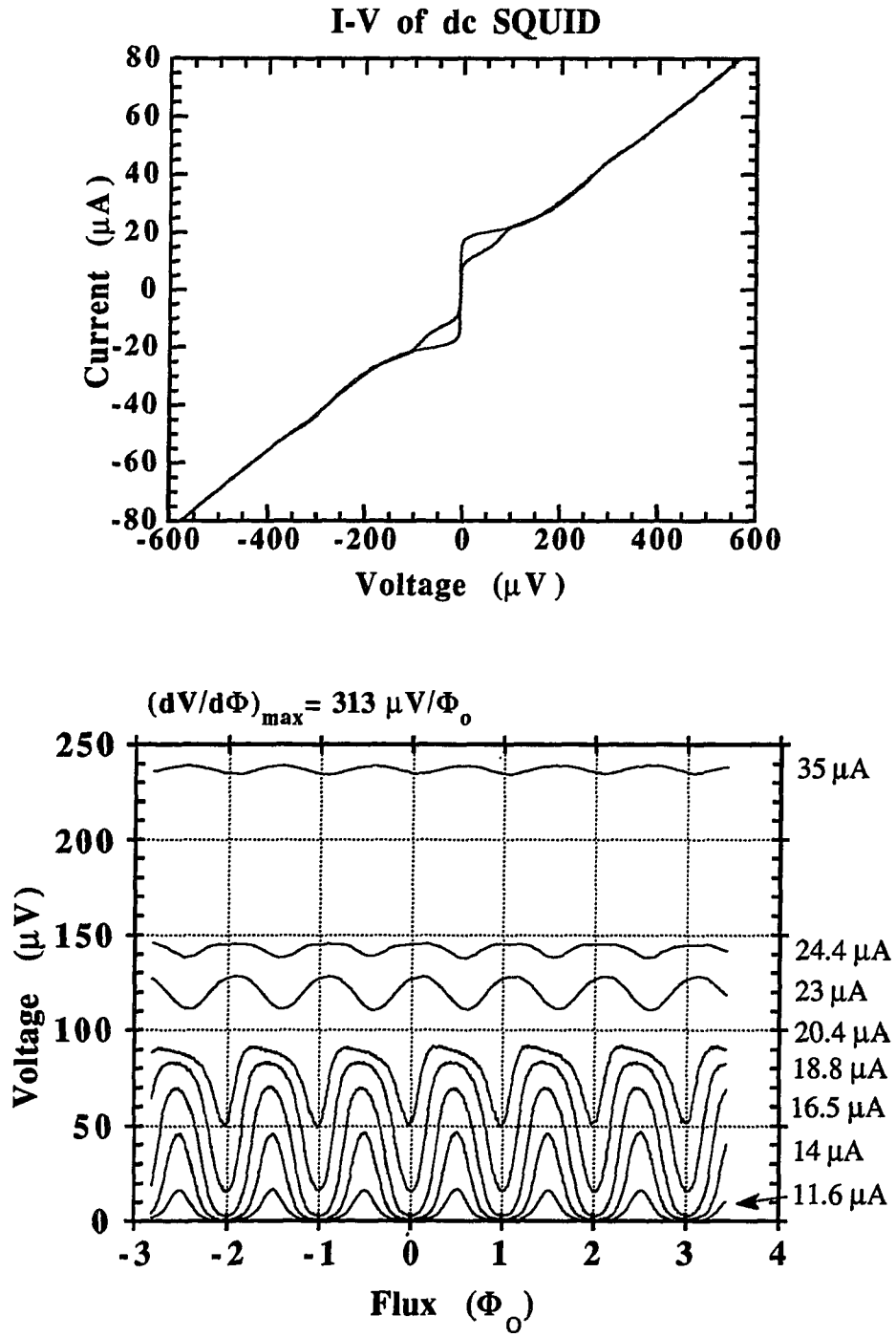

Figure 2.7 : A typical I-V and V vs $\Phi_{applied}$ for a niobium dc SQUID fabricated in our lab. Different curve on the transfer function corresponds to different bias current.

magnetic resolution of the SQUID at the bias point is just the rms flux noise, $\langle \Phi_N^2 \rangle$, which is defined as follows,

$$\langle \Phi_N^2 \rangle = \int_{f_1}^{f_2} S_\Phi(f)df \qquad (2.9)$$

and

$$S_\Phi \equiv \frac{S_V}{\left(\frac{dV}{d\Phi}\right)^2} \qquad (2.10)$$

where f_1 to f_2 are the frequency range of interest and S_V is the voltage spectral density across the SQUID biased at maximum transfer function. To compare the sensitivity of SQUIDs of different inductances the flux noise energy is often used and is defined as

$$\varepsilon(f) = \frac{S_\Phi(f)}{2L} \quad . \qquad (2.11)$$

There are two parameters that characterize a dc SQUID. The first parameter is β_C and this is the damping factor of the junction, as discussed previously. The second one is the screening factor and is defined as $\beta \equiv 2LI_C/\Phi_O$. Tesche and Clarke[8] have calculated that the flux noise energy of a SQUID is optimized when $\beta=1$ and $\beta_C \leq 1$ and its value is

$$\varepsilon(f) \approx 16 k_B T\sqrt{LC} \quad . \qquad (2.12)$$

In this result they have assumed a symmetric SQUID and the only source of noise comes from the Nyquist noise of the two shunt resistors. For $\beta>1$, the noise scales as $\beta^{1/2}$ and for $\beta<1$ it scales as $\beta^{-2/3}$.

In the white noise regime, the quantum noise for the SQUID has been predicted[9] to be $\sim\hbar$. The best SQUID fabricated to date[10] has flux noise energy of about $1.6\hbar$ at 1.5K.

Lowering the temperature does not improve the noise. This can be explained by the hot electron effect of the shunt resistors.[11]

The 1/f noise in the SQUID is due to two effects. The first effect is thermal fluctuations in the critical current of the junctions. This process is well understood and can be eliminated by biasing the SQUID with an AC current in the feedback mode.[12] The second effect is the motion of trapped flux in the superconductor (Nb for our SQUIDs)[13]. The 1/f noise here is intrinsic to the material and cannot be eliminated, but it scales with the amount of trapped flux!

2.2 Design

The design of the SQUID used in our experiment is shown in figure 2.8 along with the SEM photograph. Since the spatial resolution requirement for our experiment is 10 μm, the design of the SQUID hole is 10μm x 10μm. The inductance of this SQUID loop is estimated by measuring the modulation depth to be about 40 pH. To achieve $\beta \sim 1$ and $\beta_c < 1$, we need each junction to have a critical current of 25 μA and a shunt resistance of 10Ω. We evaporate a mixture of Au/Pd (1:1 by weight) as the shunt resistor. A thickness of 1200Å gives a resistance of about 1Ω /square. Any nonsuperconducting materials can be evaporated as shunt resistors, but it is important that the material does not oxidize in air. This ensures that the resistance characteristics of the SQUID will remain unchanged through thermal recycling. Copper and aluminum are prohibited.

A typical layout of the SQUID without the input coil consists of 6 layers. It is a good rule of thumb to minimize the number of layers in designing any device. The more layers there are to fabricate, the more difficult it is to make a working device. Stacking many layers on top of each other creates steep trenches and hills which cause metallic interlayers between insulator layers to short out. Packing many layers can be achieved by using the method of planarization[14].

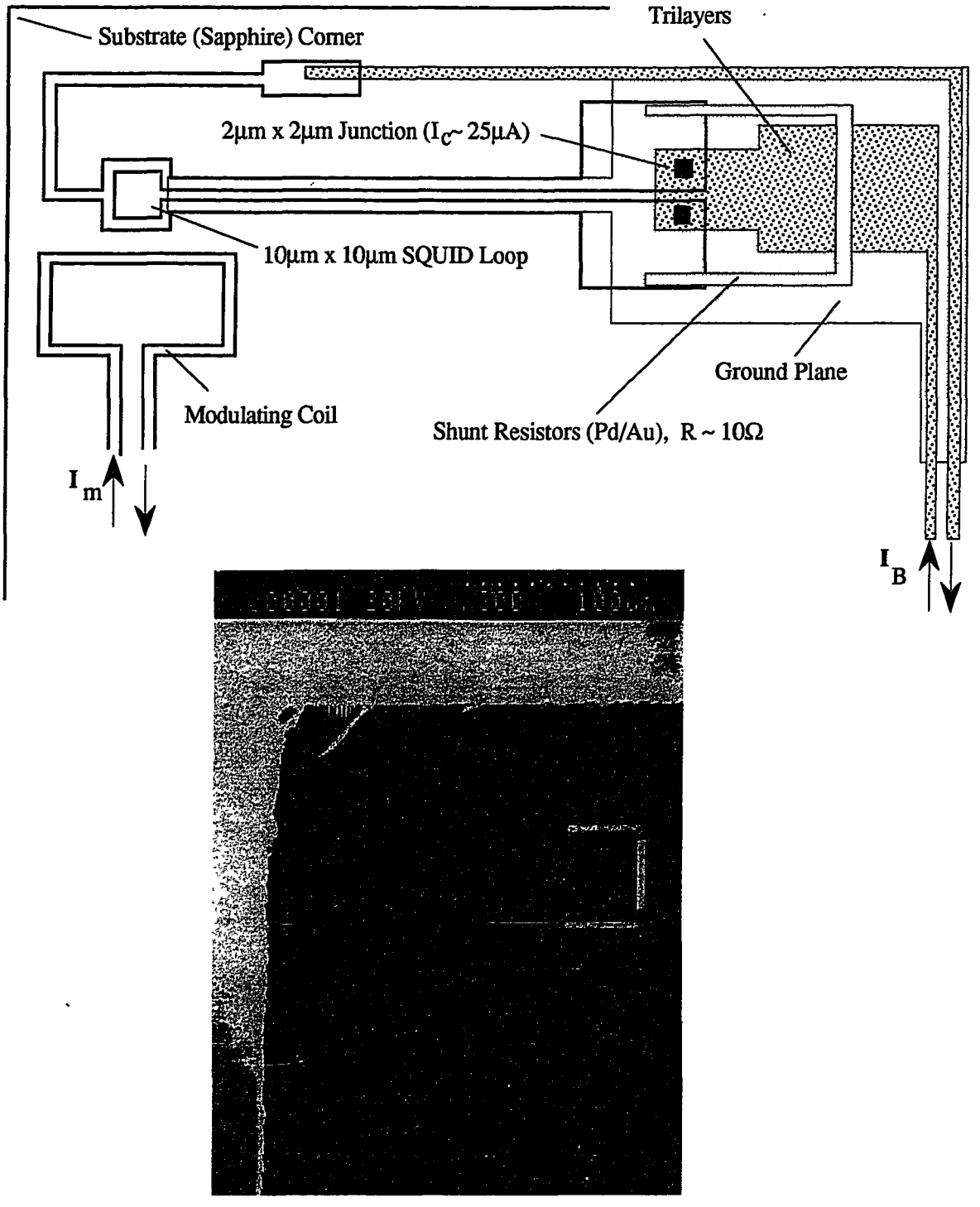

Figure 2.8 : Design layout of a dc SQUID along with SEM picture.

The layout of our SQUID design is as follows. The first layer is the 1200Å niobium ground plane (London penetration depth of Nb $\lambda_L \sim 800$Å). This layer shields out any magnetic field signal that is not picked up by the 10μm x 10μm SQUID loop and prevents fields from penetrating the shunt resistor loops. The second step is to put down two layers of SiO to insulate the ground plane. The third layer is the Nb/Al-Al_2O_3 trilayer deposition. This layer also defines the modulation coil and the big wiring pads. The next layer defines the junctions. The contact to the counterelectrode, which is the SQUID loop, is deposited after the junctions are defined. The sixth layer is the shunt resistor layer. If the device is good after testing then a final protective SiO layer (~5000Å) is deposited.

The mutual inductance of the modulation coil to the SQUID loop is measured to be about ~ 1.3pH (0.63 Φ_0/ mA) and a good SQUID has a transfer function of about 300μV/Φ_0. To increase this mutual inductance of the modulating coil to the SQUID, the modulation coil can be fabricated on top of the SQUID loop. This design however requires an additional insulator step. For very sensitive measurements down to 10^{-4} Φ_0 it is important to have a tight coupling constant between SQUID and modulation coil. The reason is that now only a small amount of dc current in the modulating coil is needed to modulate the SQUID and this small modulating field would not perturb the vortex being detected.

A point to be noted here is that any loops that are created by the shunt resistors must be ground planed. If not ground planed, stray inductance from the resistors can cause LC resonances in the I-V curve which can degrade the performance of the SQUID in the flux-locked mode.[15]

2.3 Fabrication

Fabrication of superconducting devices, specifically dc SQUIDs, is probably the most difficult part of this experiment. It is a skill that is learned over many months of practice and many trials and errors. It took us 2 to 3 years of continuous fabrication before we could consistently make good SQUIDs. There is no black magic when it comes to making good devices. A thorough understanding of chemistry, deposition and etching systems, and substrate handling is vital to fabricating good devices. In truth, you have to have steady hands to make good SQUIDs.

In the following section, we will discuss the secret of fabricating SQUIDs. We will not go into the details of standard fabrication techniques such as photolithography, lift-off procedure, alignment, etc. These procedures can be found in standard texts of microfabrication processes and in D. J. Van Harlingen ex-group member's thesis. We will present you with some of the tricks we have learned and the parameters that are important in making good SQUIDs within the DVH lab.

We will start out with a brief discussion of each technique and summarize with a cook-book procedure of fabricating the SQUIDs that we used in this experiment.

2.3.1 Ion Milling and DC Glow Discharge Cleaning

We always clean our sample, either by ion milling or glow discharge, before any thin film deposition process. This is a crucial step for good film adhesion. Without milling, the film will pop off at 4K due to different contraction coefficients of the substrate and the film.

Ion mill cleaning is a process in which high energy argon atoms are used to mill away the oxide or dirty layers on the substrate surface. Milling for a long time and at high voltage can damage the surface of the substrate or the surface of a thin film. DC glow discharge cleaning on the other hand is not so destructive as argon ion milling. The argon

ions here are created by a high discharge voltage between an electrode and a ground plane in a low pressure of argon, about 10 millitorr. These argon ions are non-directional and not as energetic as argon ions in milling. It takes longer to clean the substrate with glow discharge than with ion milling (3 minutes compared to 30 seconds). We favor ion milling because the technique is more reliable for good film adhesion at low temperature. To clean a bare substrate or a niobium film, we mill it at 400V and 8 mA for 30 seconds. Longer times can damage the counter-electrode niobium film and short out the Al_2O_3 barrier underneath. For a shunt resistor evaporation, we also mill the sample in the evaporator at the same parameters as above but evaporate an addition of 40Å of chromium for further adhesion.

2.3.2 Sputtering

Sputtering is a technique for depositing a thin film by bombarding a material target with high energy argon ions. It is an excellent technique of thin film deposition if the melting temperature of the materials is too high, approximately greater than 1600°C, for resistive evaporation. Unlike evaporation, the sputtered atoms coming off the target are scattered by the Ar atoms in the chamber before reaching the sample. Thus the sputtered atoms hitting the sample are non-directional. This can be a disadvantage during the lift-off process, but is of great importance when it comes to covering the undercut of an etched part of the trilayers. We will discuss details about this process later.

We used dc magnetron sputtering to deposit niobium and aluminum thin films. To deposit an insulator thin film such as SiO_2, we had to rely on RF sputtering. RF sputtering of metallic targets is also possible, but it is not practiced in our lab.

It is crucial to sputter the Nb thin films with minimal stress. The reason is that stress between the lower niobium layer and the upper niobium film of the trilayers can cause the thin insulator Al_2O_3 to buckle and results in shorts. Many groups [16,17] have reported

good successes in fabricating all niobium Josephson junctions by depositing their niobium films free of stress. The stress of the film depends on the sputtering rate and argon gas pressure. For a constant deposition rate, the film is compressive at low sputtering gas pressure and tensile at high argon pressure[18,19]. At some crossover pressure the film is stress free. There are two techniques for measuring the stresses of thin films. One way is using laser interferometry to measure the amount of bending (concave or convex) on a 2" silicon wafer coated with 2000Å of sputtered niobium film. The other crude method that we used in the lab is to sputter a film on a substrate covered with photoresist. By performing a lift-off procedure, the stress can be observed directly. A film with no stress will lift-off without assistance. For a compressive film, the layer buckles in acetone; it would be pulled apart in a tensile state. In our system, we found that sputtering at 20 Å/sec under 10 millitorr of Argon gas pressure gives the best result. We also sputter aluminum films at the same pressure but at a much lower rate. It is not essential that the aluminum film has minimal stress because only about 50Å to 100Å of aluminum is deposited to make insulator barriers in SQUID devices.

The secret of depositing good trilayers is to heat sink the substrates. We heat sink the samples to the aluminum substrate holder with a silver paste purchased from US Gun Corp. If the paste is not used, the substrate temperature can reach above 200°C during deposition. At such temperatures diffusion between the aluminum and niobium at the interlayers is enhanced and can degrade the SIS junction[20]. Furthermore, the patterned photoresist will be destroyed at such high temperature. We can cool our samples to liquid nitrogen temperature during trilayers deposition to obtain higher current density junction and prevent interlayer diffusion. With this process, however, it is difficult to control the oxidation process of aluminum in growing the artificial barrier of SIS junctions.

2.3.3 Thermal Evaporation

Thermal evaporation is a method of thin film deposition by resistive heating a material until it reaches a high vapor pressure. Since the process occurs in a vacuum where scattering is minimal, atoms that boiled off travel in straight line from source to substrate. Lift-off process, therefore, is not a problem when the patterned photoresist is thick or when there is an undercut in the photoresist. For sputtering, lift-off is more difficult because the sputtered atoms are deposited along the sidewall of the photoresist as well. This is shown in Figure 2.9.

For evaporating the shunt resistor of the SQUID, we rotate our sample with a small electric motor. This ensures uniformity in the thickness of the film which is essential. We improve lift-off by using a thicker photoresist (5214PR, spun=4000RPM for 15 seconds). It is also important to rotate the sample during the SiO deposition step after defining the junction. This will ensure insulation all around the base electrode of the trilayers as seen in Figure 2.12.

2.3.4 Reactive Ion Etching (RIE)

Etching the niobium of the trilayers using reactive ion etching is the most difficult part of fabricating niobium Josephson devices. This step causes the most problems. If the device does not work then it is probably a problem with the etching step.

We etch niobium in a mixture of CF_4 and O_2 gases. During RIE, the rf field in the chamber causes the CF_4 molecules to be broken up into CF_3^+, F^-, and other radicals. The negative ions and radicals chemically react with the niobium and form gaseous molecules, which are then pumped out of the system. These radicals and ions also attack Si, SiO, and SiO_2. The etching rate for each one of these materials is different. Silicon etches faster than niobium, which etches faster than SiO and SiO_2. Aluminum and

Evaporation:

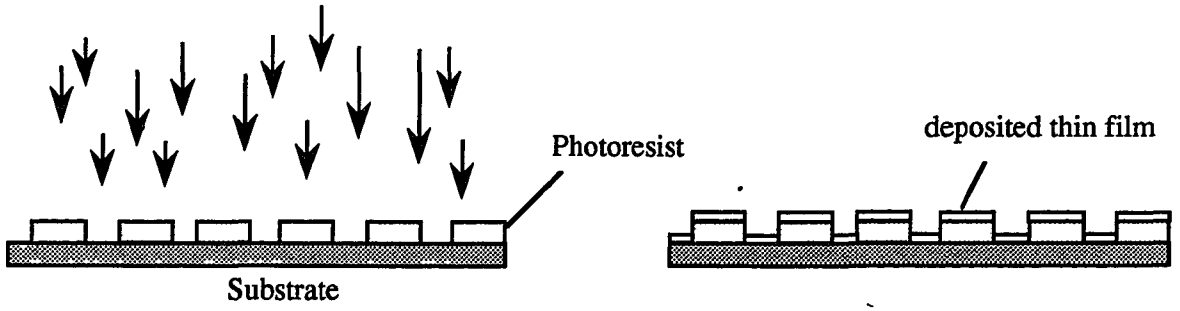

Sputtering:

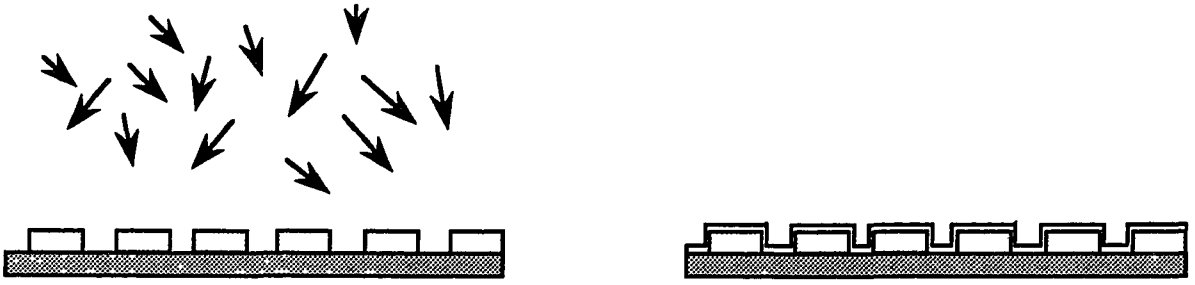

Figure 2.9 : Two different techniques of deposition- evaporation and sputtering. Liftoff is more difficult in sputtering because the film is also deposited along the walls of the photoresist.

Al_2O_3 are resistant to CF_4 etchant. Therefore the insulator of the SIS trilayers acts as an etch stopper. We noticed that Al or Al_2O_3 will eventually be etched away if we RIE the sample long enough. This process is not a chemical process but a milling process in which ions and radicals are bombarding the aluminum film. The rate of etching away Al or Al_2O_3 is hundreds of time slower than niobium in RIE.

A small mixture of O_2 during RIE is essential for making working devices. Without O_2, the SQUID will either be shorted or open. The function of O_2 is to etch the photoresist wall back as the niobium is being etched away. This is shown in figure 2.10. After all the niobium is etched away, the top niobium layer of the trilayers is tapered. An evaporation of SiO or a sputtered film of SiO_2 immediately following RIE would result in a short-free insulator. The ratio of the mixture of CF_4 and O_2 determines the tapered profile in the junction defining step. We found that it is ideal in our system to use a ratio of gas flow rate 7:1 (CF_4 to O_2) at a total pressure of 100 millitorr.

Another function of the O_2 in RIE is to get rid of polymers. RIE in pure CF_4 will result in polymer build-up along the side wall of the PR. Subsequent evaporation of SiO will create an overhang wall as seen in figure 2.11. It is impossible, therefore, to make wiring connection to the counterelectrode of the trilayers. The device thus becomes open.

If a huge overhang in the PR exists, it is then possible to RIE in pure CF_4. RIE is very directional for low pressures of CF_4 (~100mT), and since there is no vertical side wall for polymers to build on, making metallic contact to the counterelectrode of the junction is not a problem. By evaporating the etched trilayers at an angle and rotating it, a uniform insulator of SiO can be deposited without any shorts (see figure 2.12). A group from Virginia[21] has dwelled on this PR overhang technique and was able to fabricate a high quality 1μm x 1μm junctions.

The end point detection in our RIE is done by etching a reference niobium film on glass along with the trilayers to be etched. By visually observing the reference niobium

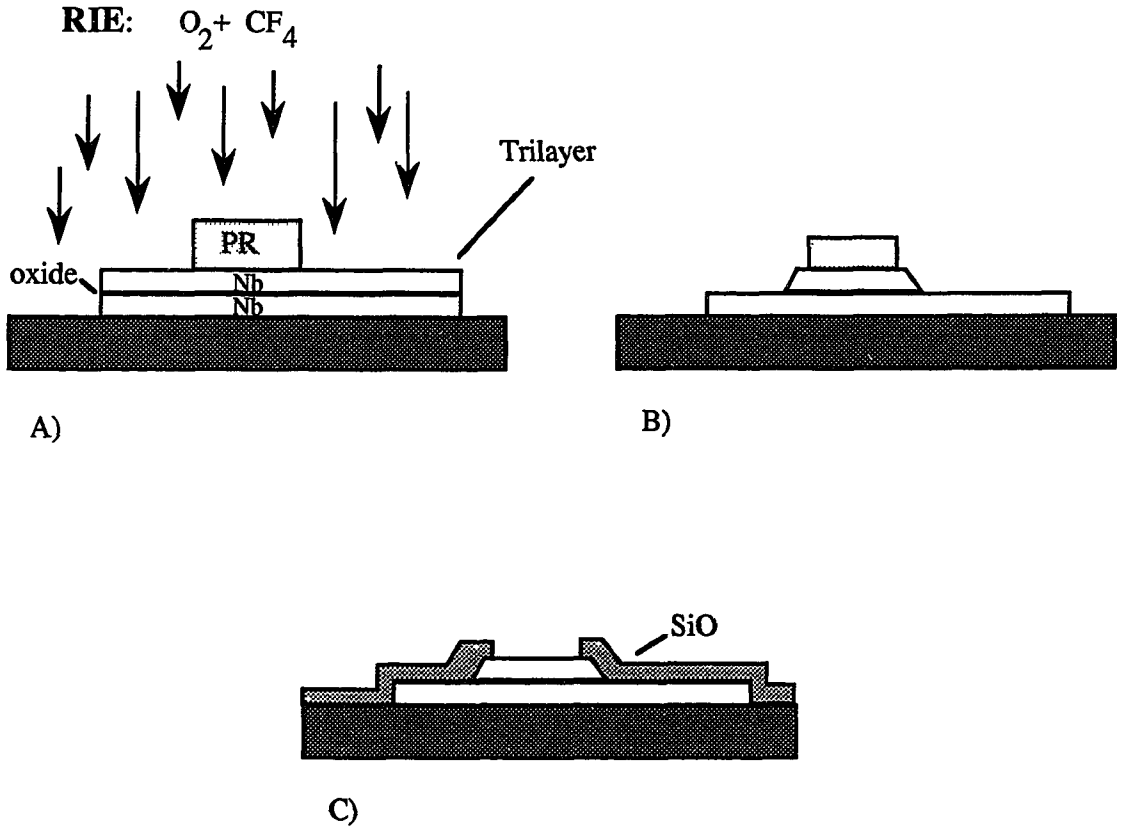

Figure 2.10 : RIE with a small mixture of oxygen etches the PR back while Nb is being etched down. Subsequent deposition of SiO ensures complete insulation of the base electrode of the trilayer.

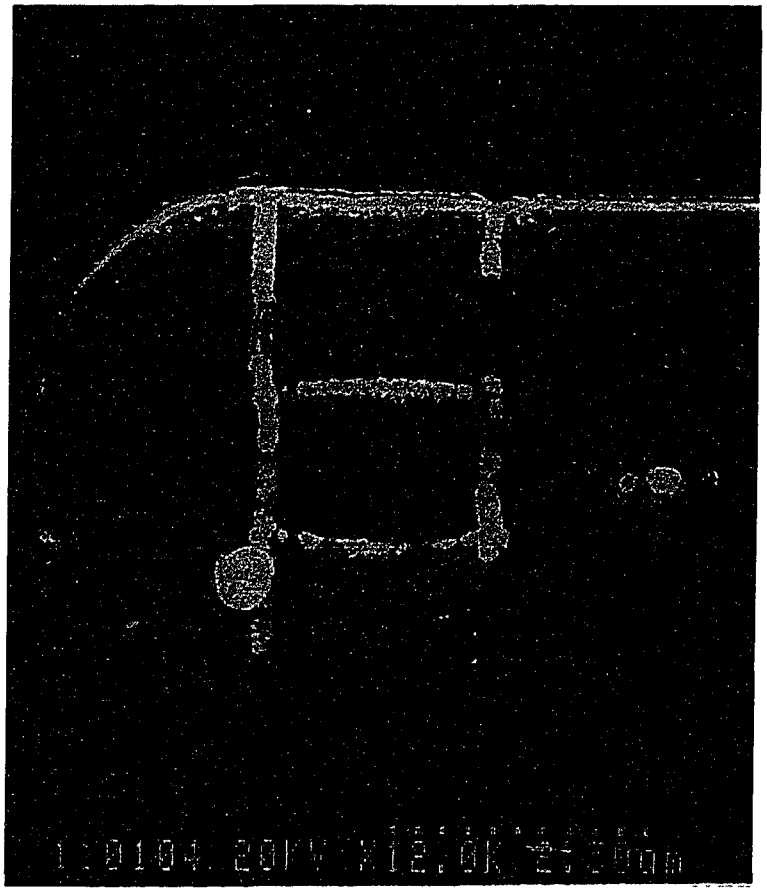

Figure 2.11 : Polymer build up along the wall of the photoresist during RIE. Subsequent deposition of counterelectrode will lead to open circuit. RIE in partial O_2 will solve the problem.

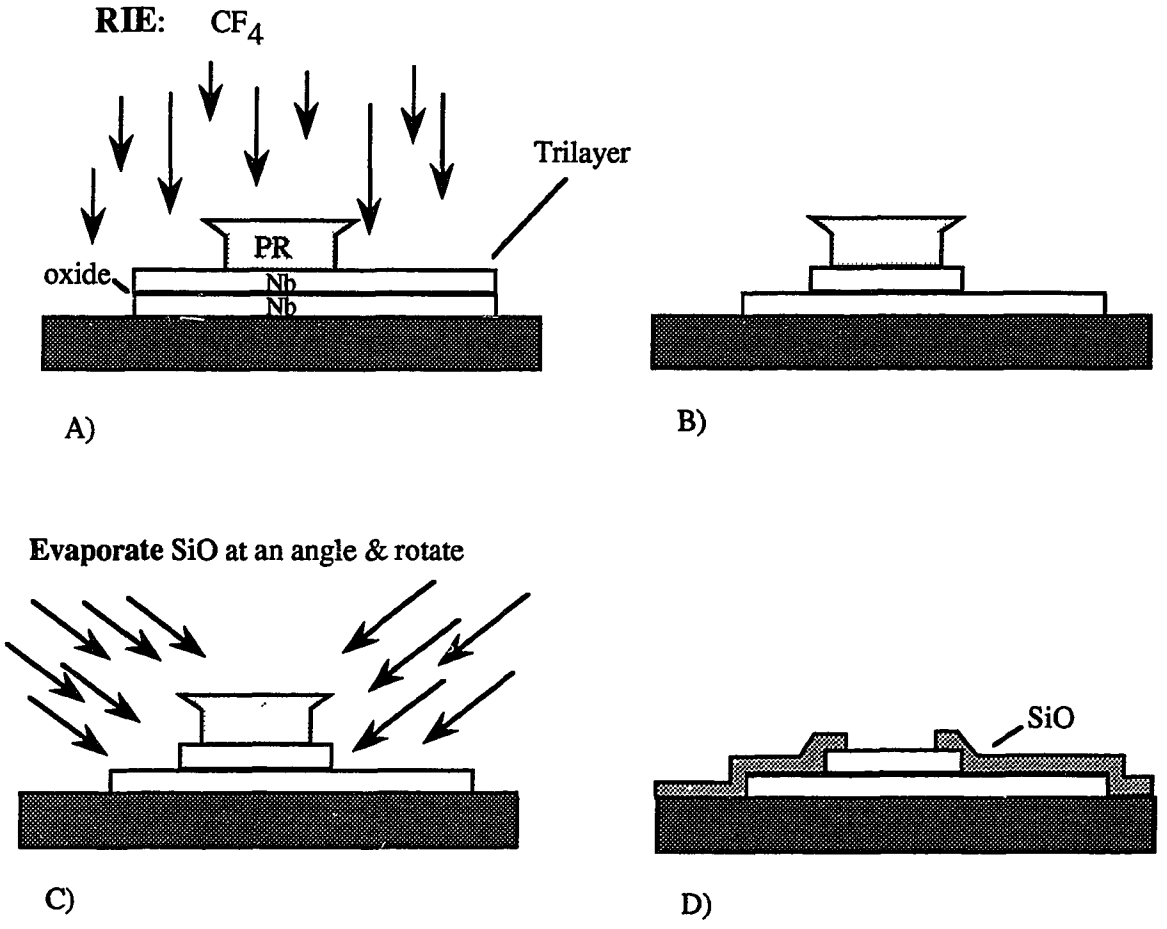

Figure 2.12 : RIE is directional. An overhang in the photoresist would prevent build up of polymers on PR walls during RIE. Evaporation of SiO at an angle while rotating would coat the base electrode uniformly and prevent shortage.

film, we can determine when the Nb counterelectrode has been completely etched. In our system, etching rate is faster out at the edge of the anode than toward the center. So, it is important to place the reference sample very close to the substrates.

2.3.5 Procedure for Fabricating SQUIDs

The following section outlines the procedure we use to fabricate SQUIDs for our experiments. For those that are not familiar with microfabrication, the following procedure should give you insight into the construction of the micro-SQUID.

I. Ground Plane
   A. Spin 5214PR (photoresist), 4000RPM, t=15 sec on a clean substrate
   B. Bake 130°C hot plate for 75 sec
   C. Expose 600 mJ UV; Develop 4:1 (water:developer) using 351 developer
   D. Mill 400V 10mA t=30sec ; Sputter 1200Å Nb @ 20Å/sec in 10 millitorr Ar
   E. Lift-off ; If the lift-off is difficult use the Q-tip assisted lift-off technique.

II. Insulator
   A. Mill 400V 10mA t=30sec; Evaporate 2000Å SiO @ 30Å/sec
   B. Clean by ultrasounding in acetone; Q-tip slightly to get rid of pinholes in the SiO, which will cause short across the metallic interlayer.
      cause short problem across metallic layers.
   C. Repeat II)A
   D. Repeat II) B

III. Trilayer
   A. Repeat I)A
   B. Repeat I)B
   C. Repeat I)C
   D. Mill 400V 10mA t=30sec
   E. Base electrode: Sputter 1000Å same parameter as I)D
   F. Barrier: Sputter 50-100Å Al (300V t=20sec on power supply of gun) at 10mT Ar
      Note: no need to wait from step E to F
   G. Oxidation: 400mT O_2 t=30min
   H. Counterelectrode: Sputter 600Å Nb @ 20 Å/sec, 10mT Ar
      Note: wait at least 1 hour from G to H for O_2 to pump out
   I. Lift-off

IV. Junction Definition, RIE, and SiO Evaporation

A. Repeat I)A
B. Bake sample in oven at 90°C t=20 minutes
   Note: higher baking temperature may degrade the trilayer
C. Expose 300 mJ UV, develop 4:1 on 351 developer until done
   Note: PR islands are small and sensitive to developing time, careful
D. RIE in CF_4:O_2 (flow rate 25:4) total pressure 100mT, 30W power, etch tills reference sample completely etched & etch additional 15sec (total ~ 7 minutes)
E. Evaporate 1000Å SiO @ 30Å/sec
   Note: Do D immediately after C. Do not ion mill before evaporating SiO. Use motor to rotate sample at an angle.
F. Lift-off. Do not Q-tip unless necessary
   Note: Do not Q-tip unless absolutely necessary after this step. Further Q-tips may smear the SiO layer into the junction area --> opens

V. Wiring

A. Repeat IV) A
B. Repeat I) C
C. Repeat I) D but sputter 2000Å instead
D. Lift-off

VI. Shunt resistors

A. Repeat IV) A
B. Repeat IV) C
C. Mill 400V 10mA t=30sec
D. Evaporate 40Å chrome @ 5Å/sec
E. Evaporate Pd/Au (1:1 by weight) 1500Å @ 10Å/sec
   Note: Sample is at an angle and rotated by motor during evaporation.
F. Lift-off

VII. Protection Layer

A. Clean sample
B. Without ion milling, evaporate 5000Å SiO @ 30Å/sec

VIII. Testing at liquid helium

IX. Dicing

A. Dice @ 10,000RPM for sapphire substrate and 30,000RPM for silicon
B. Dice SQUID close to corner of substrate as much as possible, ~ 100-200 μm

It takes about a week to do step I to step VIII. The success rate can range from

0% - 60% . The etching process is the primary reason for the low yield. We usually fabricate a batch of 8 substrates (8 SQUIDs) and start on the second batch after the first step of the first batch is finished. It is possible to fabricate for three weeks and have no working SQUIDs. Persistence nevertheless prevails.

2.4 Operation

The voltage of the SQUID is a periodic function of the magnetic flux penetrating the inductance loop, with period Φ_0 . For the device to be useful in detecting very low magnetic fields, the SQUID must be locked up at its maximum transfer function. Usually the SQUID is operated in the flux-locked loop. In this state the flux in the SQUID always remains constant. An external field picked up by the SQUID would generate a voltage which in turns feeds a current down the modulation coil to keep the total flux constant. By measuring the change of the current in the modulation coil, the external flux can be calculated.

Our schematic electronic block for the flux-lock operation is shown in figure 2.13. A 100KHz square wave of amplitude $\Phi_0/2$ biased at $n\Phi_0$ or $((n+1)/2)\Phi_0$ applied to the modulation coil results in a 200KHz sine wave across the capacitor. When this signal is mixed with the oscillator signal and integrated, the output voltage is zero. If now a small signal $\delta\Phi$ is detected by the SQUID, the 100KHz component across the SQUID is no longer zero and will give a nonzero output voltage after the mixing and integrating stages. This output voltage, which is proportional to the detected flux $\delta\Phi$, is then fed back through the SQUID modulation coil so that the SQUID is always biased at $n\Phi_0$ or $((n+1)/2)\Phi_0$. The flux the SQUID detected is just

$$\delta\Phi = \frac{V_{out}}{R_f} M \qquad (2.13)$$

We normally use $R_f \sim 5K\Omega$ to give a gain of $\sim 8V/\Phi_0$.

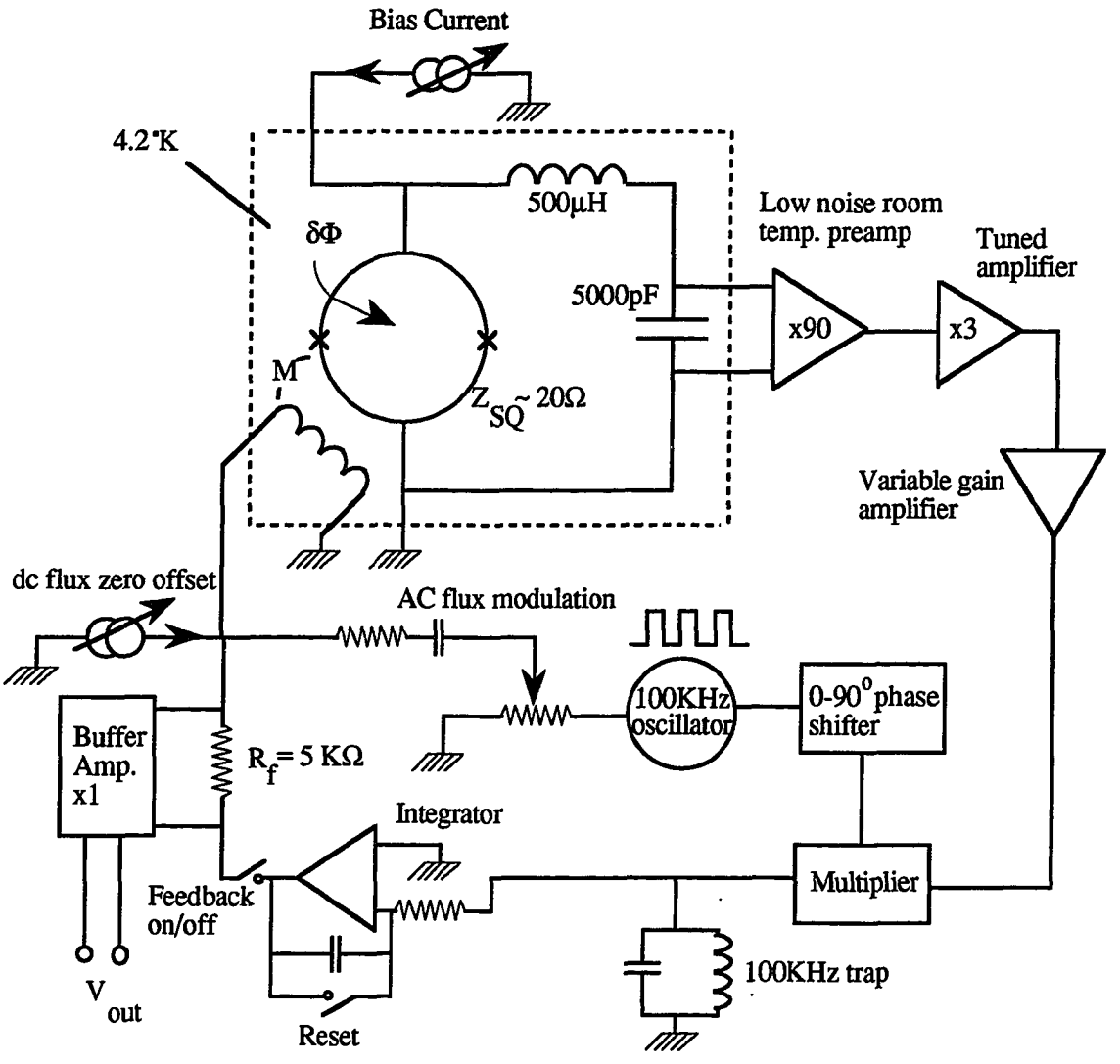

$$V_{out} = \frac{R_f}{M}\,\delta\Phi \qquad \text{In Flux-Locked Mode}$$

Figure 2.13 : Electronic diagram for operating a dc SQUID in flux-locked mode.

To optimize the performance of the SQUID, a noiseless tank circuit (operated at 4K) is necessary to boost up the impedance of the detector to the impedance of the room temperature preamp. A tank circuit of $Q \equiv \omega L/R$ would increase the signal gain of the SQUID by QV_{sig} and the impedance by Q^2Z_{SQUID}. For our configurations, $Z_{SQUID} \sim 20\Omega$ and tank circuit of Q ~16 where C=5000pF and L=500μH. Typical noise data for our SQUID is shown in Figure 2.14. The flux noise is about $6x10^{-6}\ \Phi_o/Hz^{1/2}$ above 6Hz. The system is noise dominated by the voltage noise of the homemade preamp (~ $4nV/Hz^{1/2}$ at 100KHz compared with SQUID noise out of tank circuit ~ $1.5nV/Hz^{1/2}$). Even when matched, the SQUID noise is probably still below preamp noise. By using a 5004 Brookdeal amplifier where its impedance is about 8KΩ (matching impedance of tank circuit ~ 5KΩ) and noise of $0.8nV/Hz^{1/2}$ at 100KHz, we can improve the noise to $3x10^{-6}$ $\Phi_o/Hz^{1/2}$. The gain of this preamp is fixed at 1000x and a front end attenuator must be used to prevent the preamp from going into saturation. The flux noise of our SQUID can be further reduced to ~ $1x10^{-6}\ \Phi_o/Hz^{1/2}$ if we were to use a tank circuit of matching impedance at 8KΩ. This value is about 3 times higher than the predicted flux noise (~ $3x10^{-7}\ \Phi_o/Hz^{1/2}$ according to equation 2.12). The reason for the increase in flux noise is due to the electronics. The modulating square wave coming off the electronics became a sinusoidal wave (due to LC filtering effect in the external wires) by the time it gets to the SQUID. The sinusoidal wave does not bias the SQUID at its maximum transfer function but at some average value, away from its maximum sensitivity. This effect has been calculated by Clarke[22] and has shown to increase in the flux noise by a factor of two to three from the expected value, which is consistent with our measurements.

The gain of the tank circuit drops off quite rapidly above the 3dB point above 100KHz. Our electronics therefore can operate up to a maximum frequency of about 2KHz. Operating the SQUID up to higher frequency is possible by using a higher driving frequency and a wide band transformer. Quantum Design Inc.'s dc SQUID and

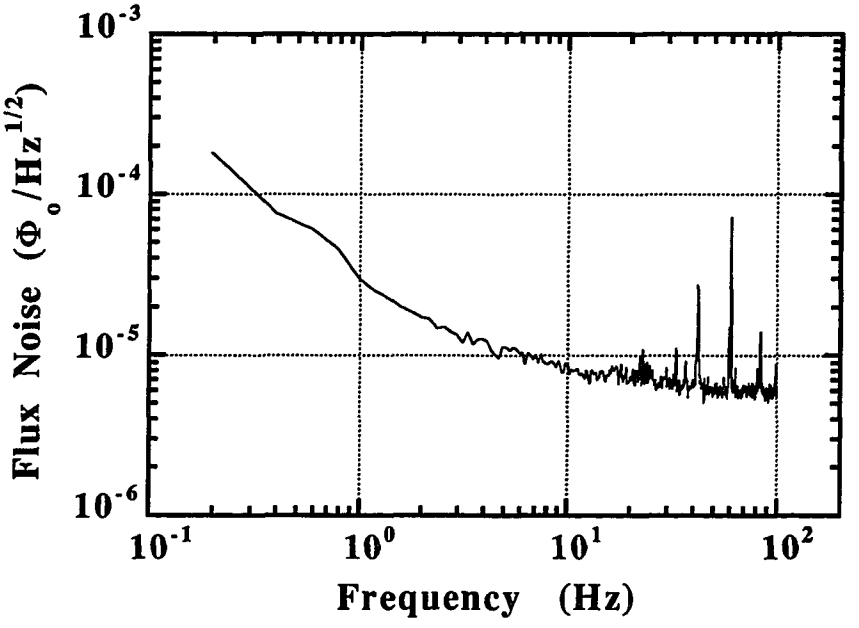

Figure 2.14: Flux noise for a typical SQUID fabricated in our lab in the flux-locked mode.

Wellstood[23] have achieved an operating SQUID up to 50KHz using a 500KHz oscillator and a wide band cold transformer. For driving frequency above 1MHz, cross-talk between the wires and external electromagnetic interference will be a problem .

References

1. A. M. Chang, H. Allen, L. Harriott, H. Hess, H. Kao, J. Kwo, R. Miller, R. Wolfe, J. van der Ziel, and T. Chang, " Scanning Hall Probe Microscopy". *Appl. Phys. Lett.* **61**, 1974-1976 (1992).

2. Y. Martin and H. K. Wickramasinghe. "Magnetic Imaging by Force Microscopy with 1000Å Resolution ". *Appl. Phys. Lett.* **50**, 1455-1457 (1987).

3. J. M. Jaycox, and M. B. Ketchen, "Planar Coupling Scheme for Ultra Low Noise dc SQUIDs". *IEEE Trans. Mag.* **17**(1), 400-403 (1981).

4. M. Gurvitch, M. A. Washington, and H. A. Huggins, "High Quality Refractory Josephson Tunnel Junction Utilizing Thin Aluminum Layers". *Appl. Phys. Lett.* **42**, 472-474 (1983).

5. H. A. Huggins and M. Gurvitch, "Preparation and Characteristics of Nb/Al-Oxide-Nb Tunnel Junctions". *J. Appl. Phys.* **57**, 2103-2109 (1985).

6. V. J. De Waal, T. M. Klapwijk, and P. Van de Hamer, "High Performance dc SQUIDs with submicrometer niobium Josephson Junctions". *Journal of Low Temperature Physics* **53**, 287-312 (1983).

7. M. B. Ketchen, "DC SQUIDS 1980: The State of the Art". *IEEE Trans. Mag.* **17**(1), 387-394 (1981).

8. C. D. Tesche, and J. Clarke, "DC SQUID: Noise and Optimization". *Journal of Low Temperature Physics* **29**, 301-331 (1977).

9. R. H. Koch, D. J. Van Harlingen, and J. Clarke, "Quantum Noise Theory for the DC SQUID". *Appl. Phys. Lett.* **38**, 380-382 (1981).

10. R. T. Wakai and D. J. Van Harlingen, "Signal and White Noise Properties of Edge Junction DC SQUID's ". *Appl. Phys. Lett.* **52**, 1182-1184 (1988).

11. F. C. Wellstood, C. Urbina, and J. Clarke, " Hot Electron Effect in the DC SQUID". *IEEE Trans. Magn.* **25**, 1001-1004 (1984).

12. V. Foggletti, W. J. Gallagher, M. B. Ketchen, A. W. Kleisasser, R. H. Koch, S. I. Raider, and R. L. Sandstrom. " Low-Frequency Noise in Low 1/f Noise DC SQUIDs". *Appl. Phys. Lett.* **49**, 1393-1395 (1986).

13. R. H. Koch, J. Clarke, W. M. Goubau, J. M. Martinis, C. M. Pegrum, and D. J. Van Harlingen. " Flicker (1/f) noise in tunnel junctions dc SQUIDs". *Journal of Low Temperature Physics* **51**, 207-224 (1983).

14. M. B. Ketchen, and et. al., "Sub-μm, Planarized, Nb-AlO_x-Nb Josephson Process for 125 mm Wafers Developed in Partnership with Si Technology". *Appl. Phys. Lett.* **59**, 2609-2611 (1991).

15. V. Foglietti, W. J. Gallagher, M. B. Ketchen, A. W. Kleinsasser, R. H. Koch, and R. L. Sandstrom, "Performance of DC SQUIDs with Resistively Shunted Inductance". *Appl. Phys. Lett.* **55**, 1451-1453 (1989).

16. T. Imamura and S. Hasuo, "A Submicrometer Nb/AlO_x/Nb Josephson Junction". *J. Appl. Phys.* **64**, 1586-1588 (1988).

17. K. Kuroda and M. Yuda, "Niobium-Stress Influence on Nb/Al-oxide/Nb Josephson Junctions". *J. Appl. Phys.* **63**, 2352-2357 (1988).

18. D. W. Hoffman and J. Thornton, "The Compressive Stress Transition in Al, V, Zr, Nb, and W Metal Films Sputtered at Low Working Pressures". *Thin Solid Films* **45**, 387-396 (1977).

19. C. T. Wu, "Intrinsic Stress of Magnetron-Sputtered Niobium Films". *Thin Solid Films* **64**, 103-110 (1979).

20. C. C. Chang, M. Gurvitch, D. M. Hwang, and C. W. Blonder, "Auger Electron Spectroscopy, Transmission Electron Microscopy, and Scanning Electron Microscopy Studies of Nb/Al/Nb Josephson Junction Structures". *J. Appl. Phys.* **61**, 5089-5097 (1987).

21. A. W. Litchenberger, D. M. Lea, C. Li, F. L. Loyd, M. J. Feldman, and R. J. Mattauch, "Fabrication of Micron Size Nb/Al-Al_2O_3/Nb Junctions with a Trilevel Resist Liftoff Process". *Proceedings of the 1990 Applied Superconductivity Conference. IEEE Trans. Mag.* **27**(1), 3168-3171 (1990).

22. J. Clarke, Superconducting Devices. *In* "SQUIDs: Principles, Noise, and Applications" (S. T. Ruggiero and D. A. Rudman, eds.), pp. 51-99, Academic Press, New York, 1990.

23 F. C. Wellstood, C. Heiden, and J. Clarke, "Integrated dc SQUID Magnetometer with High Slew Rate". *Rev. Sci. Inst.* **55**, 952-957 (1984).

Chapter 3

Weakly-Coupled Arrays, Wire Networks, and Clusters

3.1 Overview

Interest in this field was generated when workers[1-3] found that weakly-coupled square arrays exhibit a Kosterlitz-Thouless (KT) phase transition when they are cooled through the transition temperature in zero field, $f = 0$. According to the KT theory[4] vortices and antivortices are thermally created and bound in pairs in the array. Above a certain critical temperature, defined as T_{KT}, these pairs are screened by the other pairs and free vortices and eventually break apart. These thermally-activated vortices are free to move through the cells of the array in the presence of a current, and induce a finite voltage across the sample.

At finite field, vortices are induced in the array. Transport measurements do not show clear evidence for a K-T transition,[5,6] but the resistance of the sample oscillates as a function of applied field with a period of integer f. Minima in the resistance at values of rational f are also observed, with $f = 1/2$ being the most pronounced minimum (see figure 3.1). Theorists[7-9] have then explained these dips in terms of vortex commensurability. At rational f, vortices arrange in a periodic pattern that 'matches' with the underlying superconductor lattice and the system achieves a minimum in energy. Distortions in these commensurate patterns require a large energy. A small current injected into the sample for resistance measurement would cause only a few vortices to move, leading to dips in the resistance.

Since then much work, both experiment and theory, has been done to understand the effects of geometrical factors and disorder in arrays. These studies are important in understanding random arrays, which in many ways represent granular and high T_c superconductor films. Variation in geometry such as triangular[10], fractal[11], and

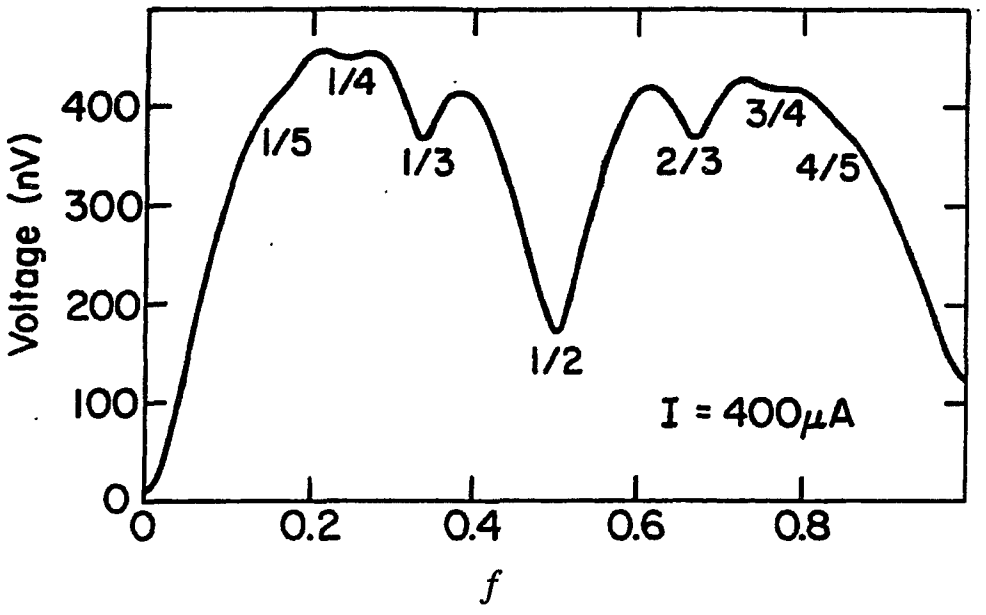

Figure 3.1 : Voltage (or resistance) vs. applied flux for Josephson junction square arrays. Sample consists of 500cells x 500 cells where each unit cell is 20μm x 20μm. (Data from Kendall Springer's Thesis)

quasiperiodic arrays[12] have been investigated. Disorder introduced by locally breaking bonds in arrays have also been systematically studied.[13] With the advent of e-beam lithography for writing nano-scale features, some workers[14-17] have turned to superconductor wire networks as an alternate system to Josephson junction arrays. These networks have a smaller cell size than weakly-coupled arrays and are made of superconducting wires of cross-sectional width (~0.2μm) smaller than the coherence length (~ 1μm for Al). In these systems, the superconducting order parameter varies only along the length of the wire and is described by the 1-D Ginzburg-Landau equation.[18,19] Near T_c, networks behave similarly to the weakly-coupled arrays. Transport measurements of networks show similar features to weakly-coupled arrays at values of rational f (figure 3.2).

Until recently, experimentalists could only measure the transport properties in weakly-coupled arrays and wire networks. Theorists, on the other hand, calculate static quantities such as the ground state vortex configurations and their energies. It has been a long standing goal for experimentalists to observe static vortex configurations in arrays. In this thesis, we have imaged magnetic vortices in arrays by Scanning SQUID Microscopy, a technique which we developed to measure weak magnetic field variations in 2D samples.

The samples in which we imaged trapped magnetic vortices were square niobium networks (figure 3.3). Our sample size ~ 1cm x 1cm consisted of 500 x 500 cells with each unit cell being 20μm x 20μm. The filament wire has a thickness t ~1200Å and a width of w ~ 2μm. For Nb, T_c is 9.2K, penetration depth λ is about 800Å , and the coherence length ξ is roughly 600Å . To understand the physics of vortices in our networks near T_c, it is essential to discuss the theory of weakly-coupled arrays and wire networks (where $\xi > w, t$). Although neither model accurately describes our samples, they are nevertheless useful in explaining the physics of vortices in our networks.

In section 3.2 we begin with the discussion of the physics of weakly-coupled superconductor arrays. This system is isomorphic to the frustrated-XY model. For an

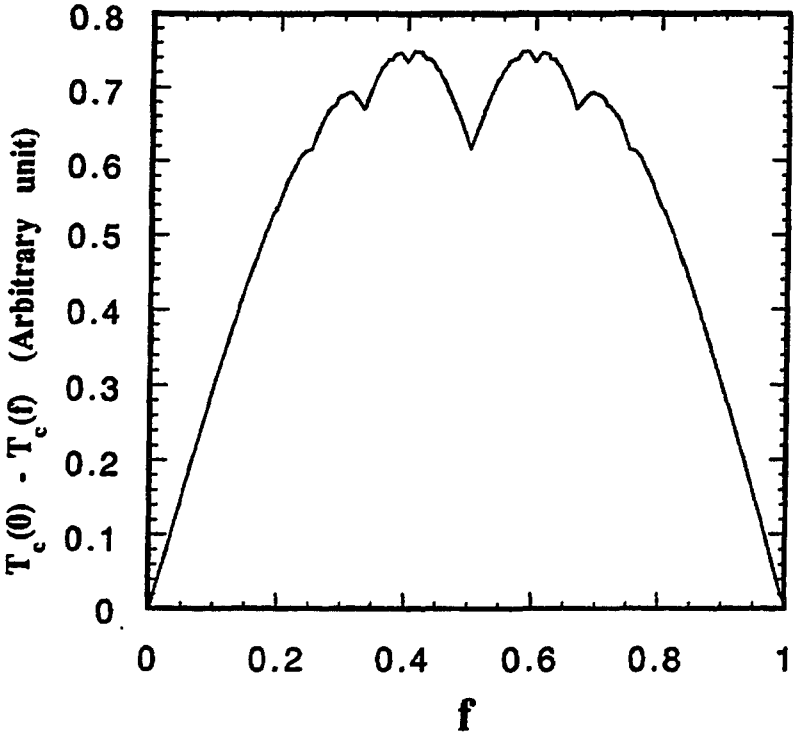

Figure 3.2 : $T_C(0)$-$T_C(f)$ (or resistance) vs. applied flux for superconducting square wire network . Sample consists of 800cells x 800 cells where each unit cell is 1.7μm x 1.7μm and wire width of 0.3μm. (Data from Fang Yu's Thesis)

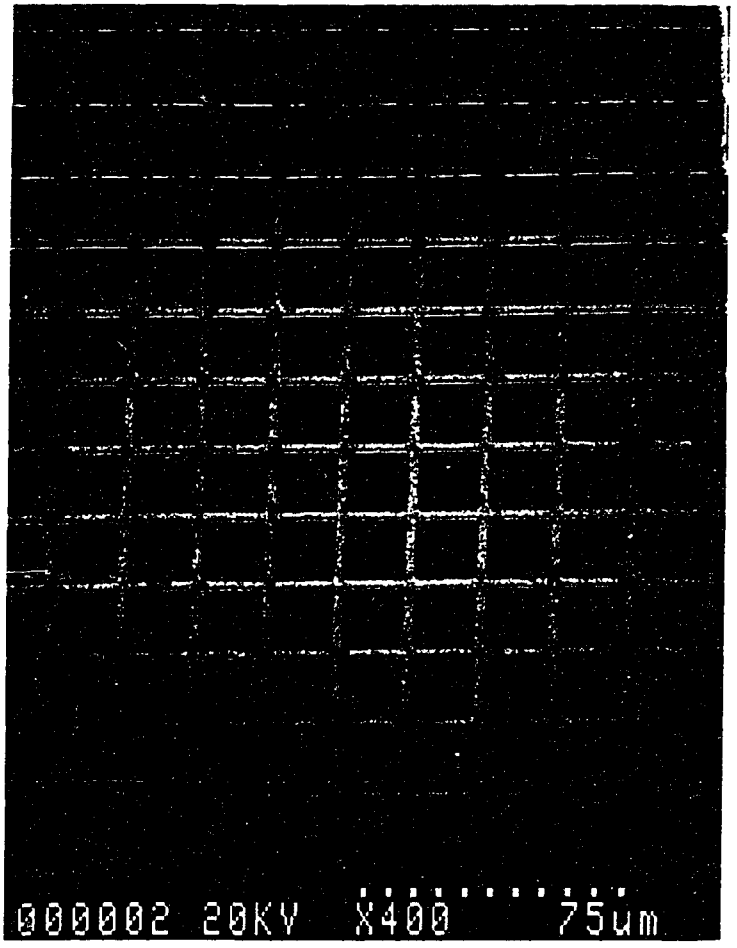

Figure 3.3 : SEM of a portion of a square niobium network consisting of 500cells x 500cells where each unit cell is 20μm x 20μm.

infinite array, Shih and Stroud[8] have used mean-field approximation to calculate the thermodynamic properties of the system. We will summarize their results. Their results agree with Teitel and Jayaprakash[7], who have approached the problem differently by using Monte Carlo simulations . Thermodynamic properties only predict the static ground state vortex patterns at rational values of f and give no information about the vortex dynamics in arrays. To understand the dynamics of vortices in arrays, we will discuss the 'single vortex model' developed by Lobb, Abraham, and Tinkham.[20] In this model, a vortex crossing a junction into the neighboring cell encounters a barrier height which is proportional to the Josephson junction coupling energy. A current applied to the junction arm exerts a perpendicular force (Lorentz force) on the vortex and causes it to move out of the cell.

The theory of superconductor networks is described in section 3.3. Very close to T_c, the linearized-mean field equations (derived from the Ginzburg-Landau theory) describing networks are the same as the weakly-coupled arrays and can be treated as an XY model. Far from T_c the similarity between the two systems diverges. The current-phase relation between adjacent nodes in networks is no longer sinusoidal but piecewise linear like in bulk superconductor. The 'single vortex model' still applies but the barrier height (a function of temperature) that a vortex sees when hopping into the next cell is much higher than in weakly-coupled arrays.

In section 3.4, we will show some of our simulation results on Josephson clusters. Results of 1x1, 2x2 ,and 3x3 clusters will be discussed. Vortex configurations in these systems are described by statistical processes and are crucial in understanding larger arrays.

3.2 Weakly-Coupled Superconductor Arrays

3.2.1 Theory

A weakly-coupled array consists of hundreds or thousands of superconducting islands that are weakly coupled through an underlayer of normal metal. These weak links are normally SNS Josephson junctions. The smallest unit of the array is the unit cell. The number of junctions around each unit cell depends on the array geometry.

For simplicity, consider an N x N junction symmetric square array in a uniform perpendicular applied field of flux Φ_a=BA piercing each unit cell of area A. Each cell consists of four junctions in a loop of inductance L, shown in figure 3.4. Phase coherence requires the fluxoid (defined as left hand side of equation 3.1) to be quantized.

$$2\pi n = \sum_{cell} \phi_{ij} + 2\pi\left(f + \frac{LJ}{\Phi_o}\right) \tag{3.1}$$

where ϕ_{ij} is the gauge invariant phase drop across the junction ($-\pi < \phi_i < \pi$), $f = \frac{\Phi_a}{\Phi_o}$ is the frustration factor, J is the circulating current around each cell, and the summation is taken over all the junctions of a unit cell. The factor n is an integer and is defined as the vorticity number. A vortex is defined when n=1. For every vortex in a cell there is an associated magnetic field that is due to two terms, the screening field from the circulating current and the applied field. The gauge invariant phase difference is related to the order parameter of the superconductor island as follows

$$\phi_{ij} \equiv \varphi_i - \varphi_j - A_{ij(\text{across junction})} \tag{3.2}$$

where

$$A_{ij} \equiv \frac{2\pi}{\Phi_o}\int_i^j \vec{A}\cdot d\vec{l} \tag{3.3}$$

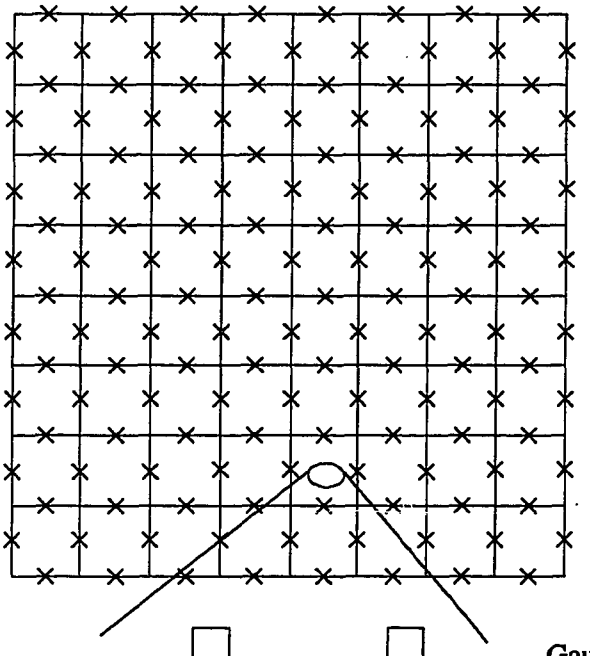

Gauge Invariant Phase

$$\phi_{ij} = \varphi_i - \varphi_j - \int_i^j \vec{A}\cdot d\vec{l}\Big|_{(\text{across link})}$$

Phase Coherent Condition

$$2\pi n = \sum_{\substack{\text{junctions}\\ \text{in unit cell}}} \phi_{ij} + \frac{2\pi}{\Phi_o}(\Phi_a + LJ)$$

Figure 3.4 : Phase coherent condition in a unit cell of an infinite weakly-coupled square arrays.

For a uniform field B applied perpendicular to the array, the magnetic vector potential is taken as $\vec{A} = Bx\hat{y}$. The Hamiltonian of the whole array is the sum of the Josephson coupling energy of all the junctions and circulating currents in the array,

$$H = -E_J \sum_{\langle ij \rangle} \cos\left(\varphi_i - \varphi_j - A_{ij}\right) + \sum_{\langle ij \rangle} \frac{1}{2}\left(\frac{L}{4}\right) J_{ij}^2 \qquad (3.4)$$

The summation is taken over all nearest neighbors, L/4 is the inductance of a single arm of the cell, and J_{ij} is the current flowing from island i to j. Equation 3.4 only includes nearest neighbor mutual inductance between cells. For a weakly-coupled array, $\left(\beta_L \equiv \frac{2\pi L I_c}{\Phi_o} << 1\right)$, the second term of eqn. 3.4 is much smaller than the first one and can be neglected.

In an applied field, circulating current is generated around each cell to satisfy the phase coherent condition (eqn. 3.1). This gives rise to a distribution of vortices in the array. At low temperature and for zero bias current, the vortices redistribute themselves to achieve a minimum in free energy given by equation 3.4.

If we write down the equation of motion of the array as we did in the junction and the dc SQUID (section 2.2), the picture would be analogous to a 'particle' of mass C moving in a multi-dimensional potential well, where each gauge invariant phase ϕ_{ij} across a junction represents a dimension in a phase space. Each minima in the multi-dimensional well corresponds to a static vortex configuration in the array. If a bias current is now applied to the array, the multidimensional potential well is distorted and the 'particle' of mass C will eventually be in the running state. At this point vortices flow in the array and a finite voltage drop occurs across the array. This is known as flux flow in the array and corresponds to the resistive region near T_c. By lowering the temperature or reducing the bias current one can trap the phase particle in some metastable state. The same effect holds

true for a superconducting network, but the only difference is that a vortex in a cell of the network is predominantly magnetic flux of Φ_0, whereas a vortex in the weakly-coupled array of β_L=0.1 is made up mostly of junction phases and the magnetic flux contribution (from our simulation result) is only ~$10^{-3}\Phi_0$.

3.2.2 Mean Field Calculations

Shih and Stroud[8] have calculated the free energy for an infinite square array using mean-field approximations. Their results have been very successful in explaining the transport measurement results[2,3,21,22] qualitatively. Their treatment assumes that all the phases φ_i of the superconductor islands are classical thermodynamic variables within the canonical ensemble and that the exact Hamiltonian (equation 3.4) can be approximated by an effective Hamiltonian, H_{eff}. The effective Hamiltonian for the i^{th} superconductor island is given as

$$H_{eff}^{(i)} = -\sum_{j\neq i} E_J\left[\cos\varphi_i\left\langle\cos\left(\varphi_i + A_{ij}\right)\right\rangle + \sin\varphi_i\left\langle\sin\left(\varphi_i + A_{ij}\right)\right\rangle\right] \tag{3.5}$$

The partition function Z_i and the "phase-order parameters" η_i for the i^{th} superconductor island are defined as follows

$$Z_i = \int_0^{2\pi} e^{-\beta H_{eff}^{(i)}} d\varphi_i \tag{3.6}$$

$$\eta_i \equiv \left\langle e^{i\varphi_i}\right\rangle \approx Z_i^{-1}\int_0^{2\pi} e^{-\beta H_{eff}^{(i)}} e^{i\varphi_i}\, d\varphi_i \tag{3.7}$$

where $\beta=(k_BT)^{-1}$. The expectation values of equation 3.5 are to be calculated self-consistently in the form of eqn. 3.7. Equation 3.5 to 3.7 constitute a set of N-coupled nonlinear complex equations in the N unknowns η_i and, in general, must be solved numerically. Near T_c all of η_i are small as well as $H_{eff}^{(i)}$. The term $e^{\beta H_{eff}^{(i)}}$ can then be

approximated as $1-\beta H_{eff}^{(i)}$. Substituting this term into eqn. 3.7 and carrying out the integral will result in the linearized mean-field equation given as

$$\eta_i - \frac{\beta}{2} E_J \sum_j e^{iA_{ij}} \eta_j = 0 \tag{3.8}$$

Equation 3.8 is precisely the Schrödinger equation in the tight-binding representation for an electron of charge 2e in a magnetic field, where η_i is the wavefunction of the i^{th} site, E_J is the nearest-neighbor hopping potential, and β^{-1} is the energy eigenvalue. $T_c(f)$, a quantity which experimentalists can measure, is the highest value of T at which eqn. 3.8 has a nontrivial solution. The ground state energy at T=0K, a quantity that experimentalists cannot measure, is calculated by solving for η_i of equation 3.7 at T=0K and substituting into the following equation

$$E_g(f) = -\sum_{\langle ij \rangle} E_J \mathrm{Re}(\eta_i^* \eta_j e^{iA_{ij}}) \ . \tag{3.9}$$

The results of $E_g(f)$ at T=0K by Shih and Stroud are shown in figure 3.5. This result agrees with the Mote Carlo calculations done by Teitel and Jayaprakash.[7] At certain fractional f there are dips in the energy curve. The ground-state vortex configurations at these rational f are periodic and commensurate with the underlying lattice.[7,9] Figure 3.6 shows vortex configurations for a few values of f. In theory it is possible to predict the ground-state vortex configurations for all rational f, but as the denominator fraction f gets larger, the probability of the achieving ground-state configuration becomes unlikely. At finite temperature, fluctuations become important and ground states are destroyed.

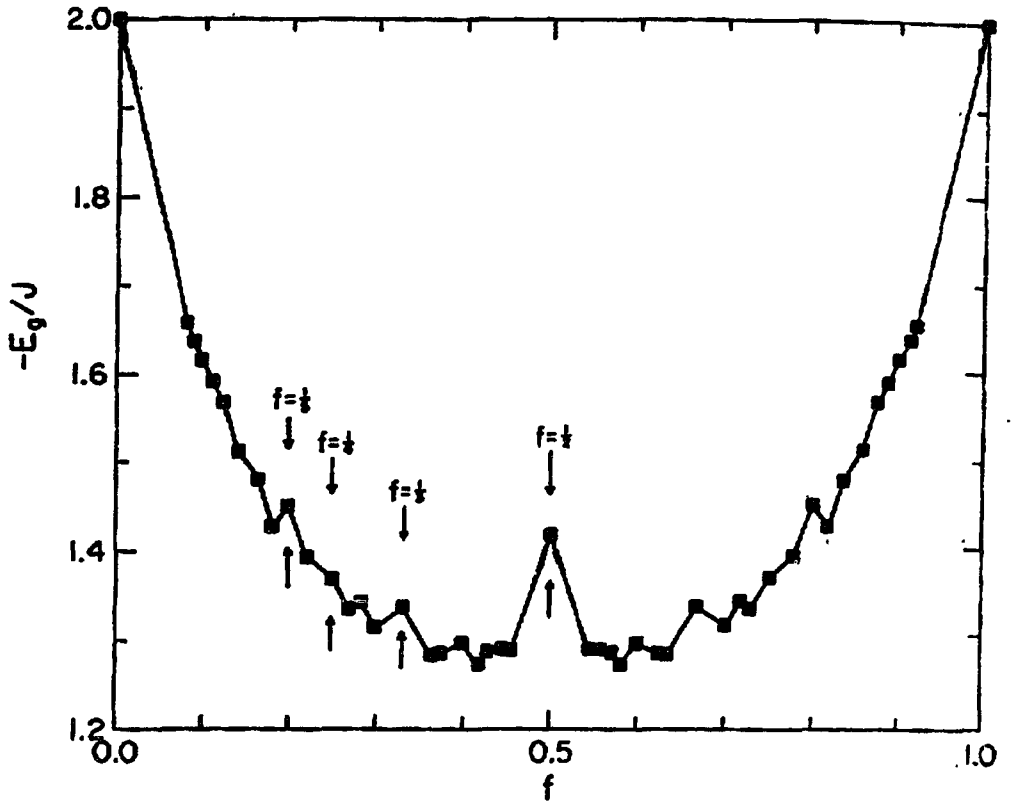

Figure 3.5 : Ground state energy calculations at T=0K vs *f* (frustration factor) by Shih and Stroud for an infinite square weakly-coupled array. J defined here is equivalent to E_J in equation 3.4.

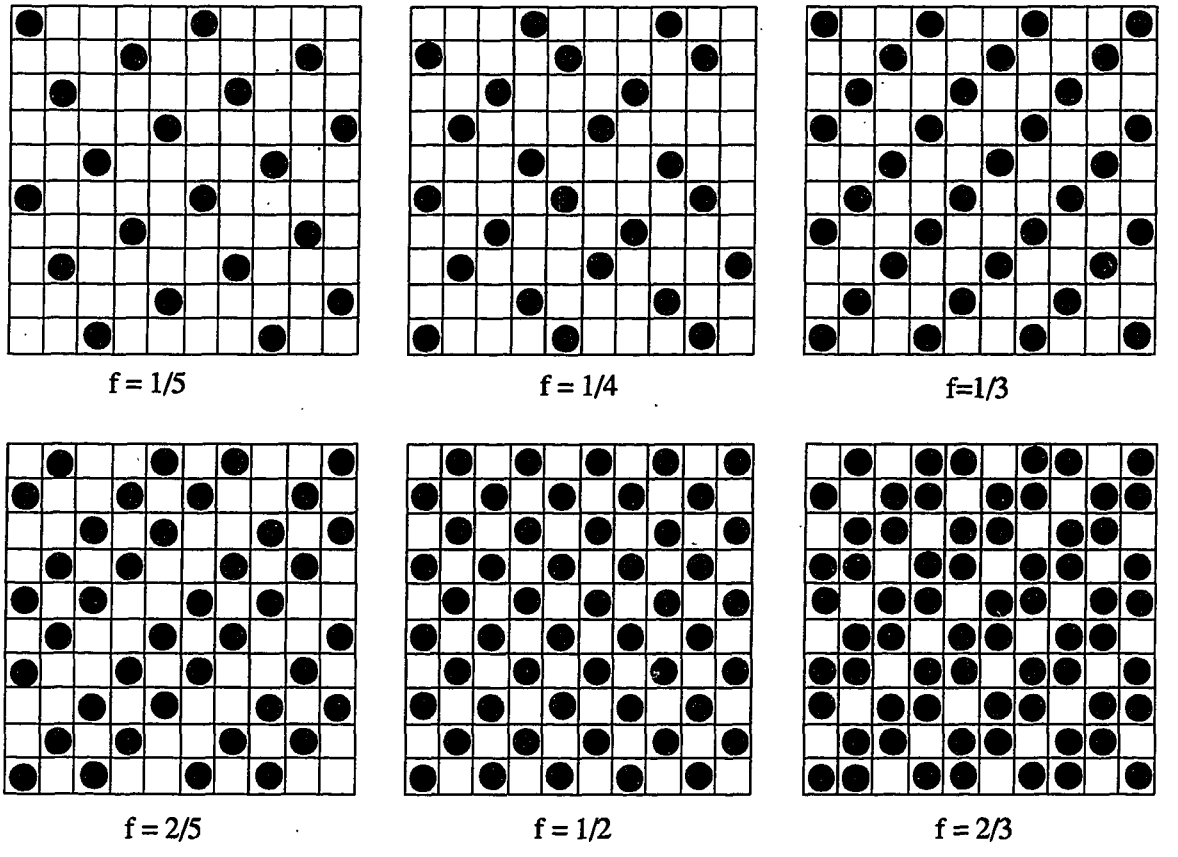

Figure 3.6 : Theoretical predictions of vortex configurations for several fractional values of f. Black dots are vortices. At fractional f vortices are commensurate with underlying lattice.

3.2.3 'Single Vortex Model'

To understand the dynamics of vortices in arrays it is necessary to introduce the 'Single Vortex Model'.[20] This model assumes the array has only one vortex so that vortex-vortex interactions are nonexistent. According to this model, a vortex has a minimum in energy when it is in the cell. The energy is a maximum when a vortex is on top of the Josephson junction defining the two cells. In a large square array, this energy difference, defined as the barrier energy U_b, is $0.2E_J(T)$ and is even lower, $0.034E_J(T)$ for triangular arrays. A vortex traveling from one cell to the next must overcome this barrier. A vortex traveling in the *y* direction of the array sees a periodic potential which can be approximated as

$$U(y) = -\gamma E_J(T)\cos\left(\frac{2\pi y}{l}\right) , \tag{3.10}$$

where $\gamma = \frac{1}{2}U_b/E_J(T)$ and *l* is defined as the length of a unit cell. The potential as a function of *xy* space is shown in figure 3.7. A current applied to the array would exert a perpendicular force (Lorentz force) on the vortex. Increasing the bias current will eventually drive the vortex into a running state. This is equivalent to saying that the potential is 'tipped' and one can write the potential as

$$U(y) = -\gamma E_J(T)\cos\left(\frac{2\pi y}{l}\right) - \frac{i\Phi_o y}{l} \tag{3.11}$$

where *i* is the current applied per junction. At finite *f* many vortices are induced in the arrays. Vortex-vortex interactions become important and the 'single vortex model' no longer applies. In this case each vortex causes 'local warping' in the potential around its position. The barrier height that a vortex sees depends on the vortex density in that region.

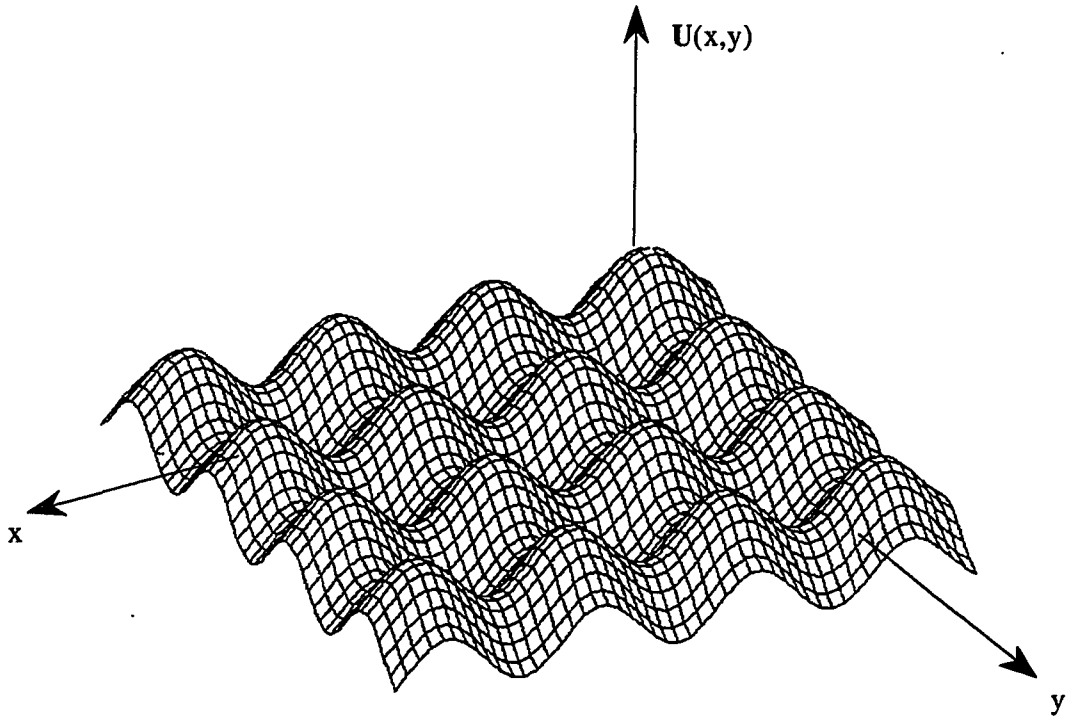

Figure 3.7 : 'Single vortex potential' as a function of *xy* positions in the arrays. The peaks in the potential are the locations of the superconducting islands.

3.3 Superconductor Networks

3.3.1 Theory

Unlike weakly-coupled arrays where the change in the superconducting phase occurs at only one point, the superconducting phase varies continuously along the wires of a network. For an exact treatment, the Ginzburg-Landau equation must be used. Alexander[18] and Toulouse[19] have worked out the solutions for a superconductor network where the coherence length ξ of the superconductor is smaller than the width *w*, and thickness *t* of the wires. For this case the order parameter (defined as $\psi = |\psi| e^{i\varphi}$) varies only along the direction of the wires and the Ginzburg-Landau equation reduces to one dimensional form. We will briefly summarize Alexander's results.

Near T_c the free energy density of the network is given by the Ginzburg-Landau free energy

$$F = A|\psi|^2 + \frac{1}{2}B|\psi|^4 + C\left|\hat{u}\cdot\left(i\nabla - \frac{2e}{\hbar c}\vec{A}\right)\psi\right|^2 \qquad (3.12)$$

where A,B,C are constants, and $\hat{u}$ is a unit vector tangent to a wire. ψ and $\vec{A}$ are defined previously. For $\xi > w$, ψ varies only along the wire so $\nabla \rightarrow \frac{\partial}{\partial s}$ and s is the curvilinear distance $\int \hat{u}\cdot d\vec{r}$. The total energy of the network is given by

$$F_{tot} = \sum_{jk}\left(\int_j^k F\, ds\right) \qquad (3.13)$$

The integral is over one link and the summation is over all wire links. Minimizing the free energy of equation 3.12 gives the following linearized Ginzburg-Landau equation on a strand of wire

$$\left[i\frac{\partial}{\partial s} + \frac{2\pi}{\Phi_o}A(s)\right]^2 \psi(s) = \frac{1}{\xi^2}\psi(s) \qquad (3.14)$$

and $\xi^2 = -\frac{C}{A} \propto \frac{T_c}{T_c - T}$ is the temperature-dependent coherence length.

The boundary condition at the node i is taken as

$$\sum_j \left[i\frac{\partial}{\partial s_{ij}} + \frac{2\pi}{\Phi_o} A(s) \right] \psi_{ij}(s)\big|_i = 0 \qquad (3.15)$$

where $A(s) = \int_i^s \bar{A} \cdot \hat{u} ds$ is the projection of the vector potential along the strand and the summation is taken over all strands connected at a given node. The real part and the imaginary part of equation 3.15 give two boundary conditions at a node. One is just the conservation of current at a node, Kirchoff's law, and the other is the phase constraint. Given the boundary conditions $\psi(s)|_i = \psi_i$ and $\psi(s)|_j = \psi_j$ the solution of equation 3.15 is

$$\psi(s) = \left(\psi_i \frac{\sin(l_{ij} - s)/\xi}{\sin\theta_{ij}} + \psi_j e^{i\gamma_{ij}} \frac{\sin(s/\xi)}{\sin\theta_{ij}} \right) e^{-i\gamma(s)} \qquad (3.16)$$

where $\theta_{ij} = \frac{l_{ij}}{\xi}$, l_{ij} is the length of the bond, $\gamma_{ij} = \int_i^j A(s)ds$, and $\gamma(s) = \int_i^s A(s)ds$.

Substituting the order parameter $\psi(s)$ (equation 3.16) into equation 3.15 we obtain a set of linear equation

$$-\psi_i \sum_j \frac{\cot\theta_{ij}}{\xi} + \sum_j \frac{\psi_j e^{i\gamma_{ij}}}{\xi \sin\theta_{ij}} = 0 \qquad (3.17)$$

For a square network all links have the same length and equation 3.17 reduces to

$$\psi_i - \frac{1}{4\cos\theta} \sum_j e^{i\gamma_{ij}} \psi_j = 0 \qquad (3.18)$$

Solving for this equation is equivalently to solving for the set of linearized-mean field equation in the weakly-coupled array.

Thus very near T_C, transport data vs f in the weakly-coupled arrays and the networks behave qualitatively the same. A superconducting wire can then be represented by a single Josephson junction where the current phase relation (equation 2.1) is sinusoidal. Well below T_C the network behaves like a bulk superconductor which screens out all applied magnetic field and trapped vortices are tightly pinned to the grids. The current-phase relation is no longer sinusoidal but piecewise linear.

3.3.2 'Single Vortex Model'

At very low fields, the 'single vortex model' still applies for wire networks. For wires with $l >> \xi(T)$ and $t,w << \xi(T)$, the barrier height for a single vortex hopping out of the potential is given by[24]

$$U_b = \left(0.94 \frac{l}{\xi(T)} + 0.2 \right) E_J \tag{3.19}$$

where

$$E_J = \frac{3\sqrt{3}\xi(T)}{2l} \frac{\hbar}{2e} i_c(T) \ . \tag{3.20}$$

$\xi(T)$ is the temperature dependent coherence length, i_c is the critical current of the superconducting filament, l is the unit cell distance, and t,w are the film thickness and filament width of wire, respectively. In networks, a vortex crossing a wire must overcome the condensation energy of the superconductor causing it to go normal. This extra energy shows up as the first term of equation 3.19. Since $l >> \xi(T)$, the second term can be neglected. The barrier a vortex sees in superconductor networks, therefore, is much larger than in weakly-coupled arrays.

3.4 Superconductor Clusters

Superconductor clusters are building blocks of arrays and networks. These systems are roughly defined for samples of less than 10cells x 10cells. Clusters are important in understanding the physics of infinite arrays and networks. Figure 3.8 shows a few weakly-coupled square clusters. Since the number of junctions is small, calculations of ground state vortex configurations and ground state energies (equation 3.4) are possible without resorting to the mean-field method.

3.4.1 Computer Simulations

We have calculated the ground state energy and metastable states vs. f for a few weakly-coupled clusters of less than 10x10 cells. From the simulations we can also extract the vortex configuration for a given value of energy. In our simulations we assumed that each branch of the loop consists of an ideal Josephson junction of critical current I_C, resistance R, capacitance C=0, and a branch inductance L/4. At every node, the current is conserved and in every loop the phase coherent condition must be satisfied. Supercurrent flowing through a junction must obey a Josephson junction relation.

The simulation begins with an initial condition f and N random phases for the N junctions in the cluster. From the N random phases the supercurrent can be calculated in each of the junctions. If the phase coherent condition is not satisfied, an additional flux from the circulating current of the loop is required to make up the difference. These normal currents cause the phases of the junctions to evolve according to equation 2.5. At some time later, Δt, a new set of N phases is calculated and the procedure begins all over until all the currents in all the branches satisfy current conservation and the phase coherent condition. At this point a value of energy and its vortex configuration of the system is calculated. At any one value of f we run the simulation many times (many initial conditions

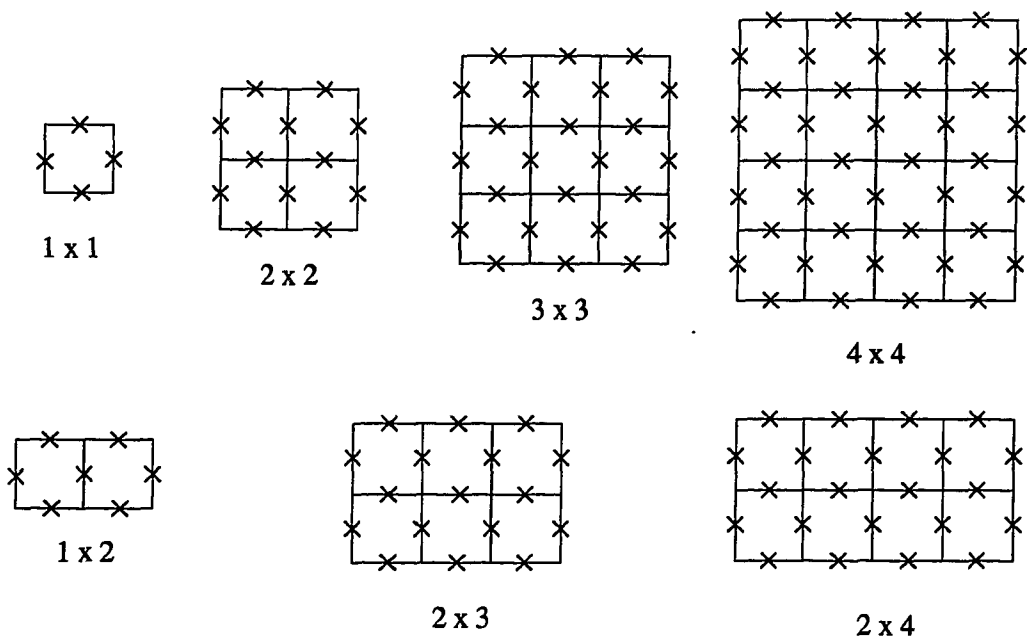

Figure 3.8 : A few examples of Josephson junction clusters.

of random phases) to get all the possible stable vortex configurations. The results of a few clusters are shown in figure 3.9. The only free parameter for these energy curves is $\beta_L=2\pi LI_C/\Phi_O$.

So far, experimentalists have not been able to measure these energy curves, but we will later describe (section 5.4) an experiment to deduce the energy curves by measuring the probabilities of capturing different vortex configurations in an ensemble of clusters. It is important to note here that our simulations are for clusters of Josephson junctions. The results nevertheless should apply at $T\sim T_C$ for clusters made of superconductor wire networks. Well below T_C the behavior of networks and weakly-coupled arrays diverge and the simulation results no longer apply.

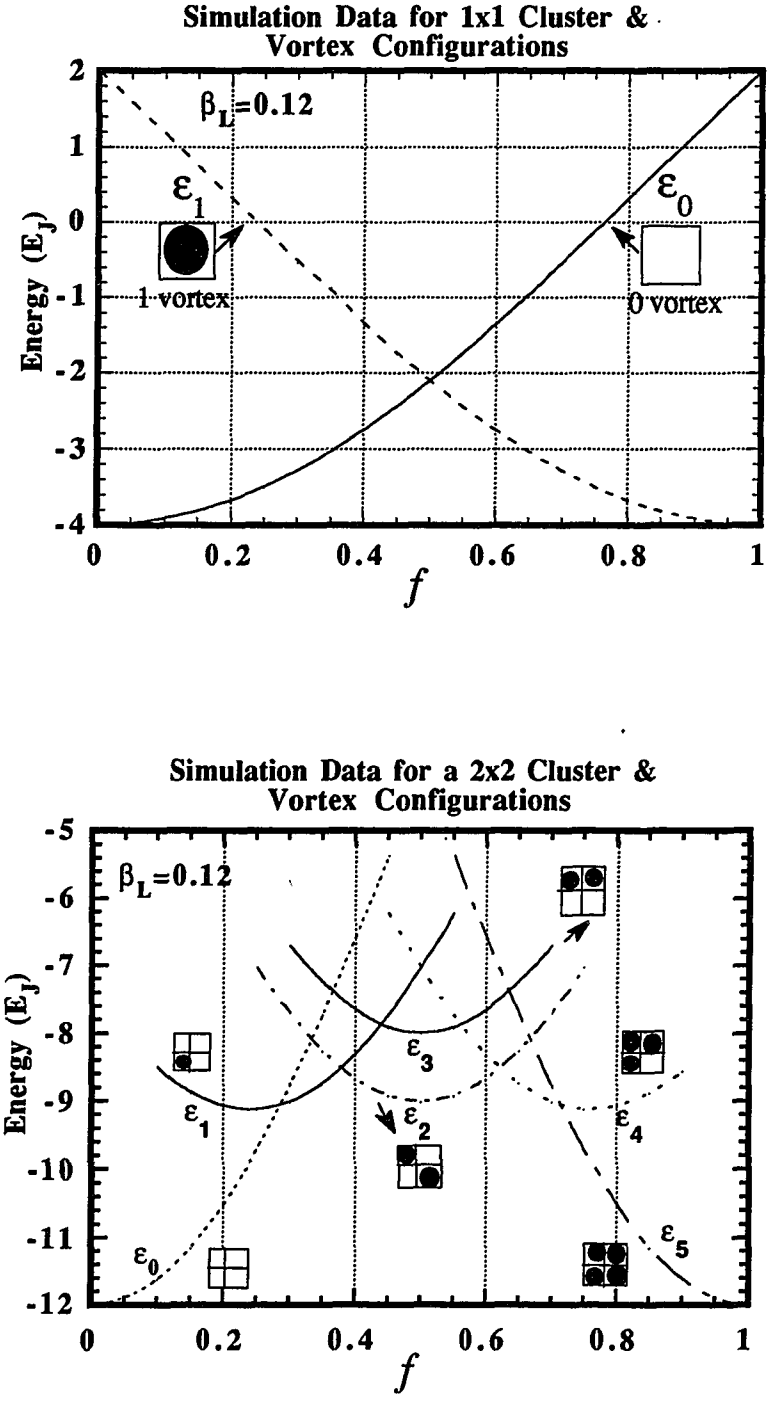

Figure 3.9 : Simulation results of a few Josephson junction clusters.

References

1. D. W. Abraham, C. J. Lobb, M. Tinkham, and T. M. Klawijk, "Resistive Transition in Two-Dimensional Arrays of Superconducting Weak Links". *Physical Review B* **26**, 5268-5271 (1982).

2. R. F. Voss and R. A. Webb, "Phase Coherence in a Weakly Coupled Array of 20,000 Nb Josephson Junctions". *Physical Review B* **25**, 3446-3449 (1982).

3. J. Resnick, J. C. Garland, J. T. Boyd, S. Shoemaker, and R. S. Newrock, "Kosterlitz-Thouless Transition in Proximity-Coupled Superconducting Arrays". *Phys. Rev. Lett.* **47**, 1542 (1981).

4. J. M. Kosterlitz and D. J. Thouless, "Ordering, Metastability and Phase Transitions in Two-Dimensional Systems". *J. Phys. C* **6**, 1181 (1973).

5. H. S. J. Van der Zant, c. J. Muller, H. A. Rijken, B. J. Van Wees and J. E. Mooij, "Experiments of Frustrated Josephson Arrays". *Physica B* **152**, 56 (1988).

6. D. Khimhi, F. Leyvraz, and D. Anriosa, "Resistive Transition in Two-Dimensional Arrays of Proximity Josephson Junctions: Magnetic Field Dependence". *Physical Review B* **29**, 1487 (1984).

7. S. Teitel and C. Jayaprakash, "Josephson Junction Arrays in Transverse Magnetic Fields". *Phys. Rev. Lett.* **51**, 1999 (1983).

8. Wan Y. Shih and Stroud, "Molecular-Field Approximation for Josephson-Coupled Superconducting Arrays in a Magnetic Field". *Physical Review B* **28**, 6575-6577 (1983).

9. T. C. Halsey, "Josephson-Junction Arrays in Transverse Magnetic Fields: Ground States and Critical Currents". *Physical Review B* **31**, 5728 (1983).

10. R. K. Brown and J. C. Garland, "Effect of Magnetic-Field-Induced Frustration on the Superconducting Transition of Proximity-Coupled Arrays". *Physical Review B* **33**, 7827 (1986).

11. Hu Jong Lee, M. G. Forrester, M. Tinkham, and C. J. Lobb, "Resistive Transition of Sierpinski Gasket Array of Weak Josephson Junctions". *Jap. J. Appl. Phys.* **26-3**, 1385 (1987).

12. D. J. Van Harlingen, K. N. Springer, G. C. Hilton, and J. Tien, "Phase Coherence and Dynamics in Weakly-Coupled Periodic and Quasiperiodic Superconductor Array". *Physica B* **152**, 134-145 (1988).

13. M. G. Forrester, Hu Jong Lee, M. Tinkham, and C. J. Lobb, "Positional Disorder in Real Josephson Junction Array". *Jap. J. Appl. Phys.* **26-3**, (1987).

14. B. Pannetier, J. Chaussy, and R. Rammal, "Experimental Fine Tuning of Frustration: Two-Dimensional Superconducting Network in a Magnetic Field". *Phys. Rev. Lett.* **53**, 1845-1848 (1984).

15. A. Behrooz, M. J. Burns, H. Deckman, D. Levine, B. Whitehead, and P. M. Chaikin, "Flux Quantization on Quasicrystalline Networks". *Phys. Rev. Lett.* **57**, 368 (1986).

16. P. Santhanam, C. C. Chi, and W. W. Molzen, "Flux Quantization in Periodic Networks Containing Tiles with Irrational Ratio of Areas". *Physical Review B* **37**, 2360 (1988).

17. J. M. Gordon, A. M. Goldman, and J. Maps, "Superconducting-Normal Phase Boundary of a Fractal Network in a Magnetic Field". *Phys. Rev. Lett.* **56**, 2280 (1986).

18. S. Alexander, "Superconductivity of Networks. A Percolation Approach to the Effects of Disorder". *Physical Review B* **27**, 1541-1557 (1983).

19. R. Rammal, T. C. Lubensky, and G. Toulouse, "Superconducting Networks in a Magnetic Field". *Physical Review B* **27**, 2820-2829 (1983).

20. C. J. Lobb, D. W. Abraham, and M. Tinkham, "Theoretical Interpretation of Resistive Transition Data From Arrays of Superconducting Weak Links". *Physical Review B* **27**, 150 (1983).

21. M. Tinkham, D. W. Abraham, and C. J. Lobb, "Periodic Flux Dependence of the Resistive Transition in To-Dimensional Superconducting Arrays". *Physical Review B* **28**, 6578 (1983).

22. Richard A. Webb, Richard F. Voss, G. Grinstein, and P. M. Horn, "Magnetic Field Behavior of a Josephson-Junction Array: Two-Dimensional Flux Transport of a Periodic Substrate". *Phys. Rev. Lett.* **51**, 690-693 (1983).

23. H. S. J. Van der Zant, M. N. Webster, J. Romijn, and J. E. Mooij, "Phase Fluctuations in Two-Dimensional Superconducting Weakly Coupled Wire Networks". *Physical Review B* **42**, 2647 (1990). H. S. J. Van der Zant, Ph.D. Thesis, (Delft University of Technology, 1991, unpublished).

24. K. N. Springer, Ph.D. Thesis, (University of Illinois, 1988, unpublished).

25. F. Yu, Ph.D. Thesis, (University of Minnesota, 1992, unpublished).

Chapter 4

Scanning SQUID Microscope (SSM)

To build an instrument for imaging magnetic vortices in superconductor arrays, many factors must be considered. First the microscope that houses the SQUID and the sample must be operated at liquid helium temperature. The instrument must be designed to hold liquid helium for at least 8 hours of operation with minimal heat loss. Next, a scanning mechanism must be designed to scan a SQUID across the array sample. This mechanism must be able to scan over at least 50 cells x 50 cells (each cell is 20μm x 20μm) of the array and a minimum of 5 data pixels per unit cell. Third, the spatial resolution of the instrument must be smaller than the size of a vortex sitting in a unit cell. This requires the SQUID detector to be within 20μm or less from the array sample.

Section 4.1 will discuss the scanning scheme of placing the SQUID within 10μm of the array sample. We will then discuss the design of the microscope in section 4.2. We call the prototype of the microscope the Scanning SQUID Microscope version 1, the SSM1. This system has achieved the spatial resolution to detect vortices but is limited to a small scanning range(~1mm x 1mm) and a restricted operating temperature range (can not go below 5.4K). A new and improved version of the SSM1, the SSM2, is shown in section 4.3. This instrument has been constructed but is yet to be operated.

4.1 Scanning Scheme

To be able to image vortices, where the size of one vortex is approximately set by the cell size 20μm x 20μm, in a superconducting grid, the SQUID must be as close as 10μm or less to the surface of the sample. The SQUID device itself is very fragile and should not touch the sample during scanning. Another consideration which must be taken into account

is that only one point of the SQUID substrate should make contact to the sample during scanning. This is to ensure that the two non-parallel flat substrates (SQUID and sample) do not jam into one another during scanning.

Our scheme of scanning is shown in figure 4.1. Here the SQUID is fabricated about 100μm from the corner of the sapphire substrate. By placing the SQUID substrate at an angle of 1° to 5° we can get the SQUID within 5μm to 10μm of the surface of the sample. We have developed a hinge mechanism which is similar to a phonographic needle of a record player to carry out this technique of scanning (see figure 4.2). A hinge is made of two pieces of aluminum connected together with a clamped thin sheet (~ 100μm thick) of mylar. This hinge does not flex along the scanning plane and has minimal backlash. At low temperature the mylar is still flexible and will bend according to the weight of the aluminum piece at one end. By adjusting the weight of this aluminum piece, the pressure of the tip of the SQUID substrate can be carefully adjusted so that the sample will not be scratched during scanning.

4.2 SSM1

With the specification of a large scanning range (at least 1mm x 1mm and up to 1cm x 1cm), scanning by piezoelectric crystals is out of the question. It is impossible to get more than 10μm range for a piezo tube 5 inches long operating at 4K. Inch worms made of two concentric piezo tubes, sold by Burleigh Corp., are ideal. At room temperature, its scan range is several inches with stepping resolution of a fraction of a micron. Its geometry, however, excludes its operation below 230K.

It would seem to be better to have a scanning mechanism self-contained and operating from the inside of the dewar. The reason is that a scanning mechanism operating inside a dewar is very resistant to external vibrations, and mechanical bending due to differences in

Scanning Scheme

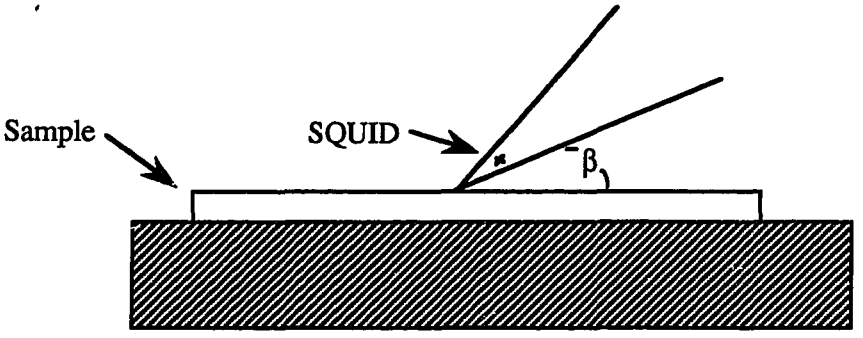

Figure 4.1 : Scanning scheme. Only one point of SQUID touches sample during scanning. Distance of SQUID to sample is $d = d' \sin\beta$, where β is the angle between SQUID and sample and d' is distance of SQUID to the corner of the substrate.

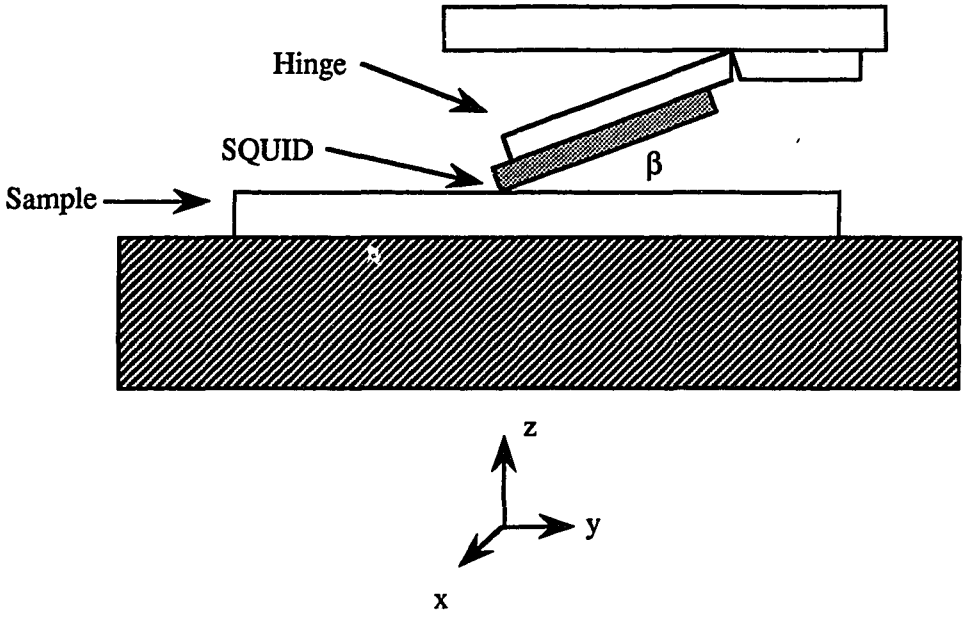

Figure 4.2 : The hinge technique. Sample moves in x-y-z direction while the SQUID remains stationary. The hinge can be made with little weight so that it doesn't scratch the sample. Note: distance of sensor to sample is known at all time, given the angle β is fixed.

thermal contraction are nonexistent. Professor Mochel suggested that we look into bimorphs as a motion transducer at low temperatures. A bimorph is made a thin piece of metal (brass) sandwiched between 2 long thin piezo slabs of the same dimension. With one end fastened, the other end of the bimorph would bend when a voltage is applied across the two piezo slabs. The amount of bending is proportional to the applied voltage. Utilizing this bending motion and amplifying the movement with some differential arm mechanism, movement up to several millimeters is possible. Unfortunately, bimorphs do not work at low temperature. At liquid helium, relative contraction between the metal and the piezo slabs is sufficient to break the glue-bond that holds them together. Even if a stronger glue is used, the brass shim would be so stiff at 4K that the bimorph would not bend much for a maximum applied voltage.

Using a mini-precision XY stage at liquid helium temperature, with a driving gear mechanism at room temperature, as a mechanism to scan the SQUID seemed an obvious choice. Our idea failed because the stage froze out at liquid nitrogen temperature. Utilizing mechanical gears at low temperature was not high in our list because we were afraid the gears would ice up and the motion would be rough. Finally, we came up with an idea of using a XYZ vacuum stage (manipulator) at room temperature as our scanning mechanism. One end of a short rigid shaft with low thermal conductivity is attached to the XYZ manipulator and the other end is attached to the sample or the SQUID at 4K. To shorten the driving shaft as much as possible so that vibration and bending are minimized, we implemented an inverted dewar.

4.2.1 Design

The SSM1 is the prototype of our Scanning SQUID Microscope. The schematic is shown in figure 4.3 and figure 4.4. The array sample and the SQUID are housed inside the indium O-ring sealed sample chamber. Both the sample and the detector are cooled by the

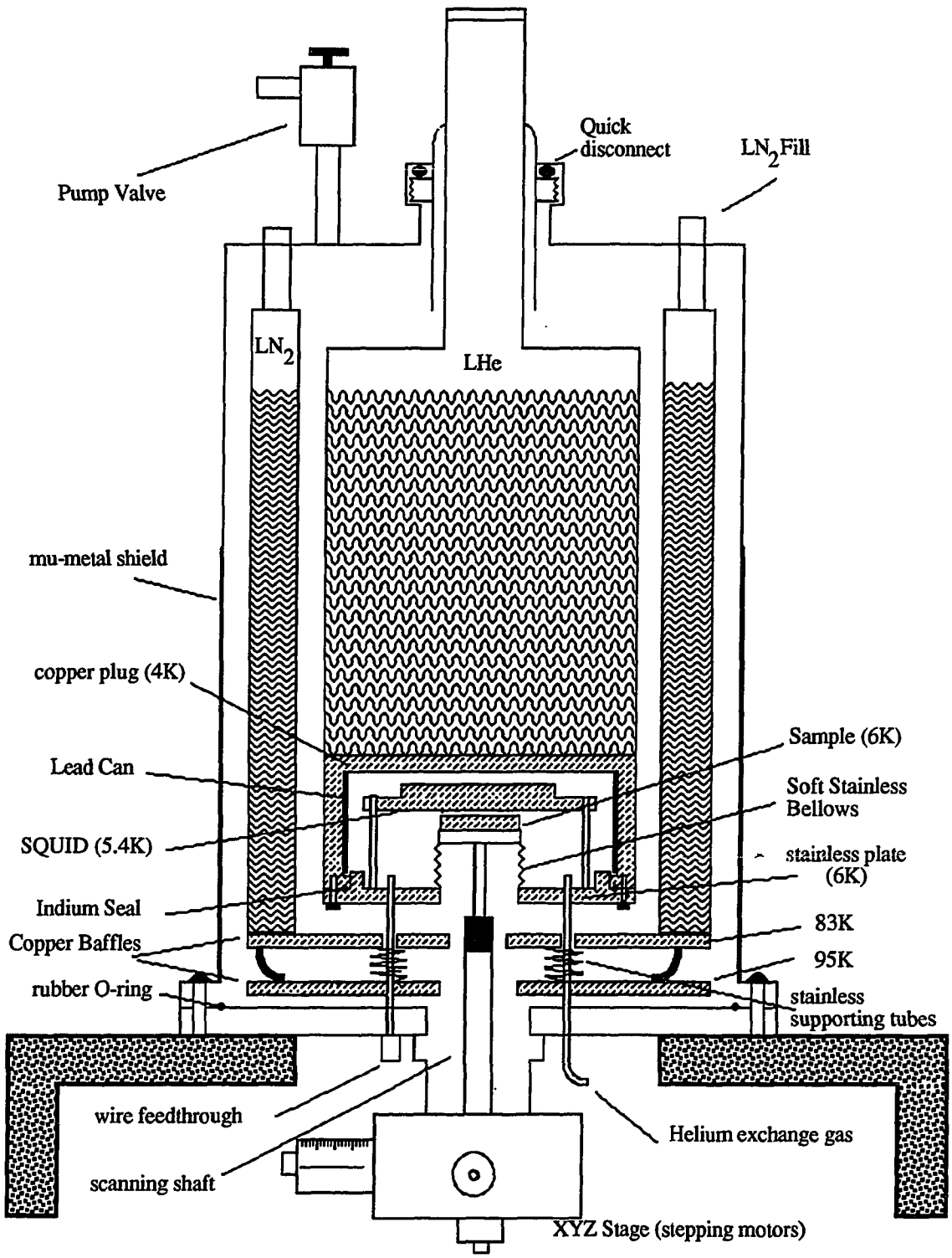

Figure 4.3 : Blueprint of SSM1. Picture is not drawn to scale.

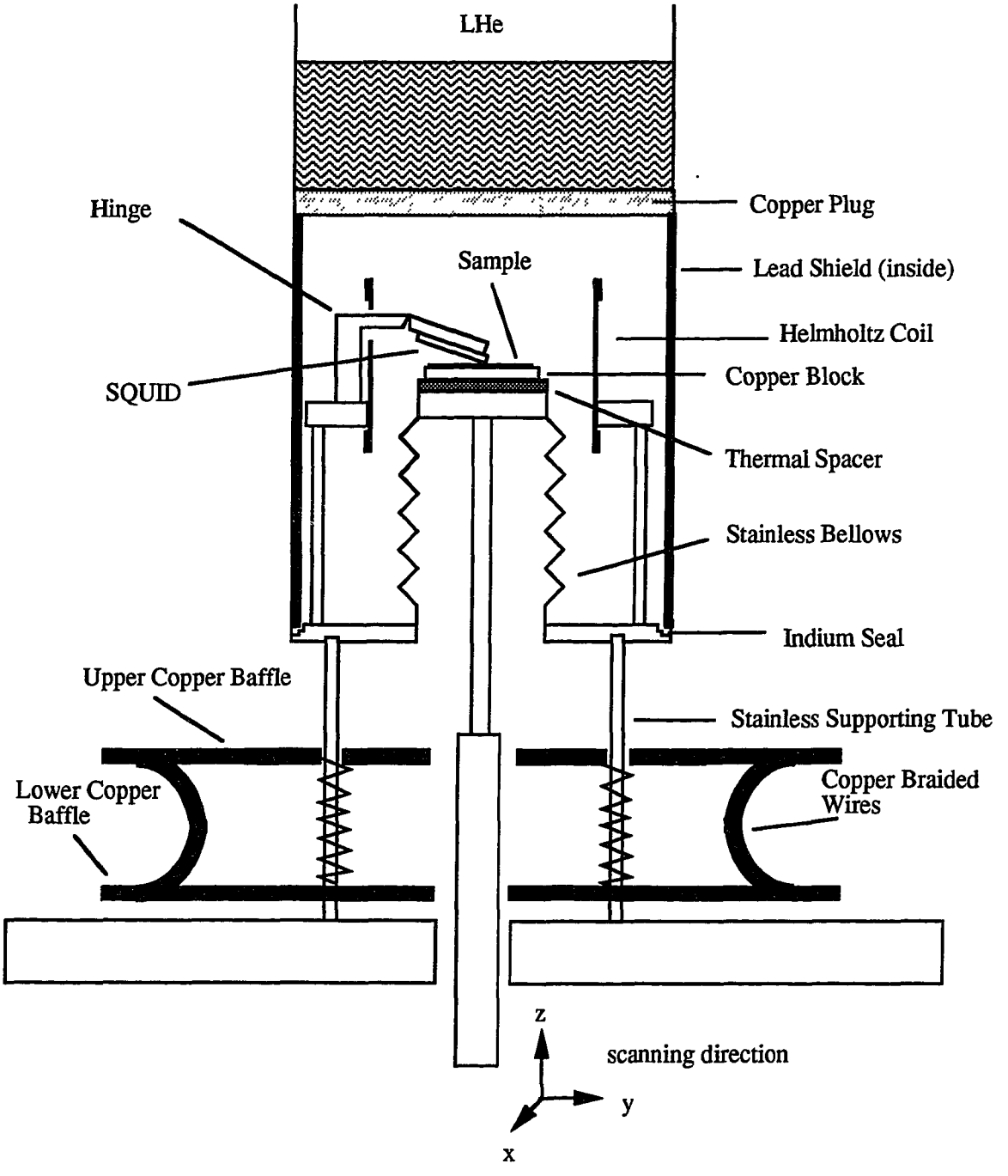

Figure 4.4 : A close up view of the sample chamber.

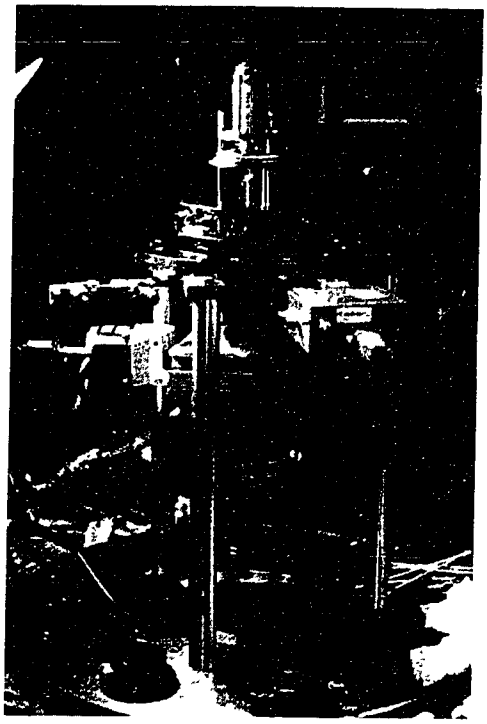

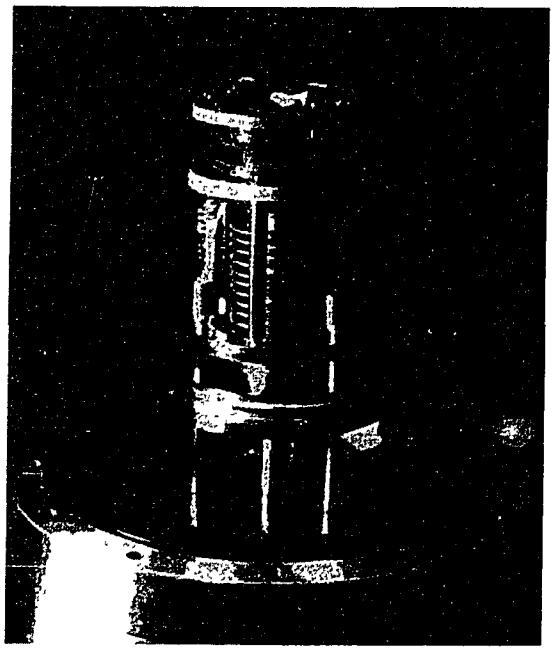

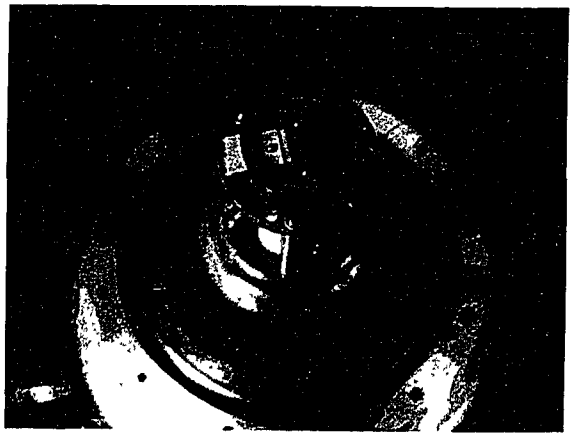

Figure 4.5 : Photographs of the SSM1.

helium exchange gas in thermal contact with the liquid helium reservoir above. The liquid helium reservoir and the sample chamber are thermally isolated from the outside world by the vacuum space inside a larger cylindrical housing that contains the liquid nitrogen reservoir and cooled copper baffles.

In our case, the SQUID is held fixed while the sample is being scanned using a stepping motor driven UHV XYZ- manipulator. The room temperature XYZ-manipulator is connected to the sample through a 47 cm rigid, low thermal conductance stainless steel shaft. The shaft is isolated from room temperature through the manipulator bellows and a soft stainless bellows in the sample chamber space. It is crucial for this bellows, which maintains a vacuum inside the sample chamber, to be very soft. Large stiffness in the bellows at low temperature can cause bending in the shaft during scanning. Also, to minimize the heat flows into the sample chamber, we heat sink the lower part of the scanning shaft to the lower cooled baffle.

The sample is mounted on a copper block on one end of the scanning shaft. A resistive heater (~100Ω) and a Si diode thermometer are imbedded inside the copper block so that the temperature of the sample can be precisely regulated. A Helmholtz coil inside the sample chamber is used to apply a uniform field to the array. Both the SQUID and the sample are shielded from external magnetic fields with a superconducting lead can inside the sample chamber and a single layer μ-metal shield on the outside of the SSM1.

With this design, to get into the sample chamber the 2" diameter quick-connect on the top must be loosened. The outer can, along with the liquid nitrogen can welded into it, can be taken off completely. By loosening the screws that tighten the indium-seal, the liquid helium can may be taken off. The assembly that holds the soft bellows, the SQUID, and the sample is supported by 3 thin wall stainless tubes which are brazed to the base plate. These 3 tubes are .010" wall and .2" in diameter.

To prevent thermal radiation from getting into the sample chamber from the bottom of

the SSM1, cooled copper baffles are used. The upper copper baffle is in direct thermal contact with the liquid nitrogen can. We used DOW vacuum grease mixed with fine copper powder to improve the thermal contact of the upper baffle to the liquid nitrogen reservoir above. The lower baffle is thermally connected to the upper baffle through clamped copper braided wires. Since the 3 supporting tubes are brazed to the lower copper baffle, the temperature of this lower copper baffle determines the amount of heat flow into the sample chamber during operation.

All the wiring in the SSM1 comes in from the bottom of the microscope through 2 of the 3 supporting stainless tubes. Manganin wires of .002" diameter are used to reduce the heat flow into the sample chamber. Each twisted pair of manganin wires has a resistance of about 100Ω. We eliminate cross talk between the wires by putting all SQUID leads through one supporting tube and the wires for the sample through the other.

The overall dimension of the SSM1 is 2 feet tall and 6" in diameter. The liquid helium reservoir is 3" in diameter and can hold up to a maximum of 1.5 liters of liquid helium. Distance of the supporting tubes measured from the base plate to the sample can is about 4 inches.

4.2.2 Operation and Results

Temperature: The temperature specification of the SSM1 in operation is shown Figure 4.3. As expected, most of the heat flows into the sample chamber through the scanning shaft and the 3 supporting stainless tubes. With liquid helium transferred into the SSM1, the helium exchange gas temperature inside the sample chamber is about 5.4K, while the temperature of the stainless block where the sample is supposed to be mounted is about 7.3K. The temperature of the stainless plate to which the 3 thin tubes are brazed is about 6.7K.

In all of our experiments the temperature of the sample is regulated by injecting current into the 100Ω resistor inside the copper block where the sample is mounted. Without heating, the temperature of the sample is about 6K. The SQUID is fabricated on sapphire substrates, a very good thermal conductor, and operates at about the same temperature as the helium exchange gas. It is important to note here that these temperatures are the absolute minimum achieved temperatures for any helium gas pressure. Increasing the pressure of helium gas beyond 1Torr of pressure will not decrease the temperature. During operation, a heater tape is used to keep the rubber O-ring of the 2" diameter quick-connect of the SSM1 warm at all time to prevent leaking because this part of the SSM1 can get quite cold.

Liquid helium is being constantly transferred into the SSM1 during the data taking process. Because of this process, pumping on liquid helium to achieve a lower temperature is prohibited. A 30 liters of liquid helium can last for up to 10 hours of data acquisition. An image of 128 pixels x 128 pixels takes about 27 minutes to scan with 5 μm/data point (1000 averages) and with stepping motors acceleration of 100 rev/sec^2 and a speed of 60 rev/sec. To eliminate any backlash and mechanical hysteresis, we do data rastering in only one scan direction.

Vibration & Noise Interference: The SSM1 is operated inside the screen room to minimize external electromagnetic interference. Without people walking in the screen room, the SQUID is very stable and can operate for many hours of data acquisition without unlocking. The electromagnetic fields generated by the stepping motors have little effect on the SQUID, but the SQUID can unlock if its transfer function is poor. The fields generated by the stepping motors are strongest when it is in first turn on. So if the SQUID can survive the initial turn on states of the stepping motors then there are no problems during the rastering process.

Shielding: With a mu-metal can, if used effectively, the Earth's field inside the can may be reduced from 500 milliGauss to less than a milliGauss. In our system, the array sample is very close to the bottom of the dewar, where the shield is not so effective. The Earth's field therefore is not shielded out completely. With a milliGauss probe and from SQUID experiments, we determined the residual field to be about 20 milliGauss. By applying an opposing uniform field with a Helmholtz coil inside the sample chamber, we can reduce the residual field close to 0 milliGauss.

The lead can is inside the sample chamber and it does not go superconducting until 7K. During cool down, we turn off all of external electronics until the sample chamber reach 5.4K. At this point the lead can is very effective in shielding out all external magnetic fields.

Scanning Shaft: We encountered some difficulties in the scanning shaft of the SSM1. For the sample bellows, we used a 13 convolution (0.5 cm/convolution) stainless steel formed bellows. This bellows is quite stiff at low temperature. The shear resistance force of this bellows is sufficient enough to cause bending in the scanning shaft when we scan over a range larger than 2 millimeters. This bending causes serious distortion in the image. For a scan range of about 900 μm x 900 μm (read from stepping motors), there are no obvious distortions. However, because there is always a slight bending in the shaft due to the bellows, the region scanned by a manipulator of 900 μm x 900 μm image is only 500 μm x 500 μm. We get this 65 % tooling factor consistently throughout many runs. Sometime in the images, there are some small distortions and glitches. These are due to the mechanical limitation of the XY micrometers screws of the manipulator. The hysteresis in our home-made mechanical hinge is minimal.

Problems & Future Improvements: From our prototype of the SSM1 we encountered a few major problems. These problems are listed as follows:

1) The scanning shaft bends due to the stiffness of the stainless formed bellows.
2) Sample chamber can not reach below 5.4K.
3) Liquid helium reservoir is too small (only 1.5 liters).
4) O-ring of quick connect in the outer can becomes cold during operation.

We have designed a second version of the SSM1 (the SSM2) in which have solved all of the problems above but it is not operational yet. We solved the bellows problem by using a welded bellows of many convolutions (about 50). This type of bellows behaves exactly like a slinky and is very soft in the shearing mode. Thus large scan range up to 1cm x 1cm without any distortions is easily achievable. The reason for problem 2) is the three stainless supporting tubes and the scanning shaft. The three supporting tubes are short (~10cm with one end at 90K) and conduct about 60mW of heat into the sample chamber. The scanning shaft on the other hand conducts ~ 200mW of heat. In the SSM2 we have eliminated the three supporting tubes entirely and reduced the thermal conductivity of the scanning shaft by replacing the stainless with a ceramic rod. The thermal conductivity of ceramic is about 10 to 100 times lower than stainless steel. Problem 3) is solved by increasing the holding capacity of liquid helium from 1.5 liters to 6 liters. The design of the SSM2 does not involve a quick-connect so problem 4) does not exist.

4.3 SSM2

4.3.1 Design

As suggested above, we made a few improvements in the SSM2 over our SSM1 prototype. The schematic is shown in figure 4.6 and figure 4.7. In this design we eliminated the 3 stainless supporting tubes totally. The only direct source of heat coming

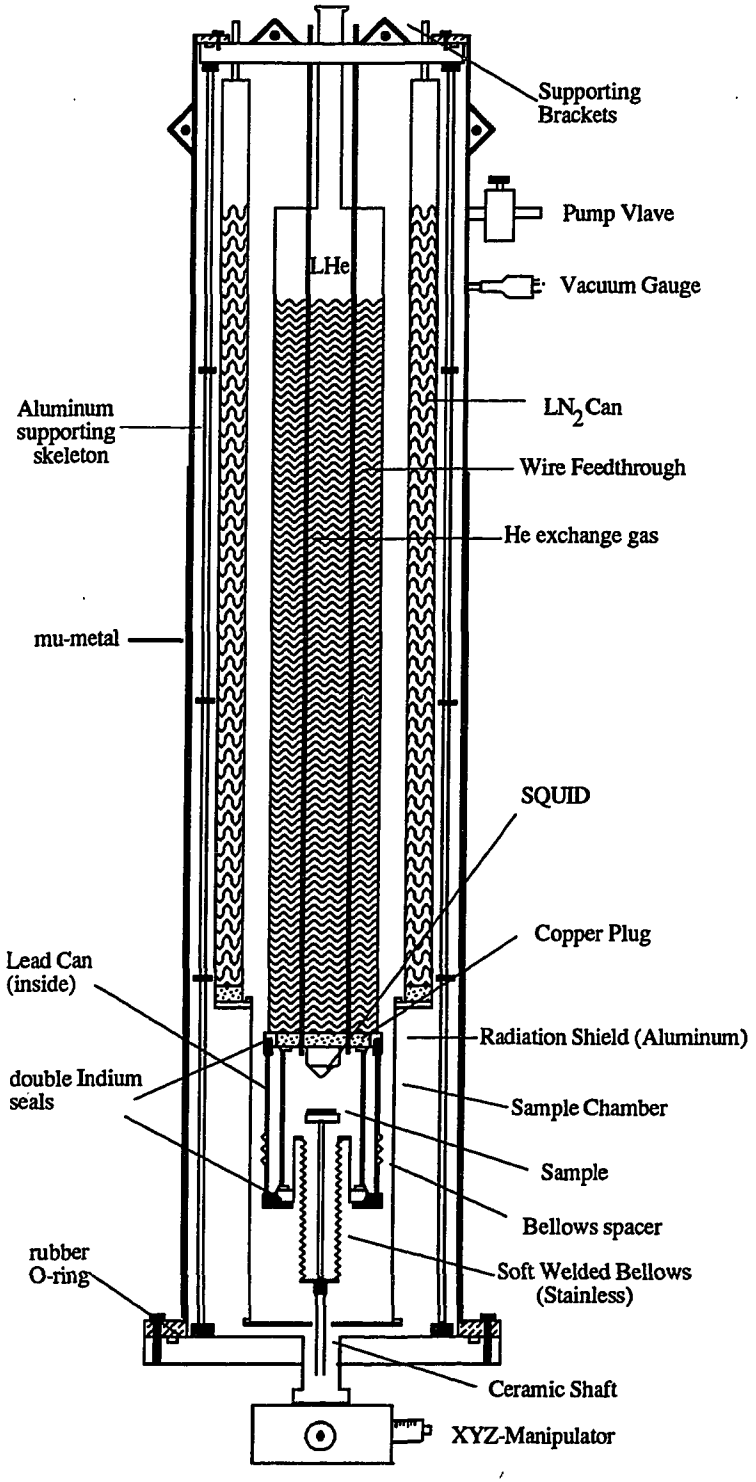

Figure 4.6 : Blueprint of the SSM2.

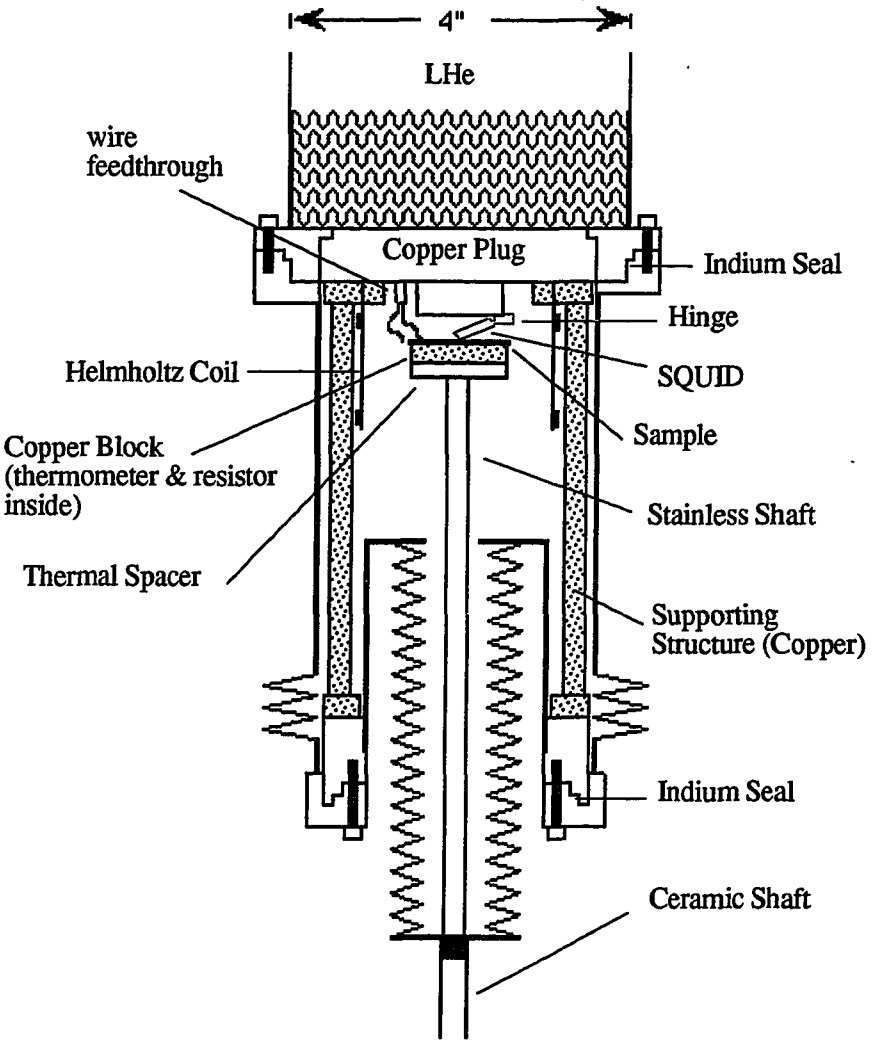

Figure 4.7 : A close-up view of the sample chamber of the SSM2.

into the sample chamber is through the scanning shaft. The 2" diameter quick-connect is not used here so heater tape is not necessary. Wires for the sample and the SQUID come in from the top. Liquid helium space is increased from 1.5 liters to about 6 liters. Since the heat leak has been dramatically minimized, continuous transferring of helium is unnecessary and we can expect to pump on the liquid helium bath to get the sample inside the chamber below 4K.

In this design, the top plate, where the liquid helium can and the liquid nitrogen can are welded, is held fixed by 4 strong threaded rods which are bolted to strong aluminum supports. To hold the top plate and the base plate fixed at all time, a skeleton of aluminum rods and rings is used. This structure can be taken off whenever necessary by unbolting the screws on the top plate and the screws on the bottom plate. With this feature, the 3 supporting tubes in the old SSM1 are eliminated.

To get into the sample chamber, the outer can must be lifted. By unbolting the screws outside on the top plate and the bottom plate, the outer housing can be lifted up to about one foot. The weakness of this design is the double O-ring concept. It is not usually practiced, but it is not a problem if the outer can and the aluminum skeleton can be machined to match within tolerance. The radiation shield is made of aluminum and its structure is made of two halves of a cylinder overlapping each other. This overlapping eliminates any direct line of sight to room temperature radiation. This liquid nitrogen shield can be taken off by unscrewing the bolts on the bottom of the liquid nitrogen bath.

The design of the sample chamber, again, utilizes the double indium O-ring seals. For the top seals and the bottom seals to seal simultaneously during tighten of the indium, the sample can must be machined very precisely. Precision machining to a few thousandth of an inch over 6 inches is nontrivial. We solved this stringent condition by using a short flexible spacer made of stainless steel bellows to allow stretching and contraction while tighten the Indium seal. By unbolting the screws on the top and bottom seals, the can of the

sample chamber can be dropped down 6 inches. The SQUID and the sample are now easily accessible.

The bellows in the sample chamber is inverted in this design. This is to minimize the torque on the scanning shaft from the bellows. This bellows is brazed to a short 1/4" solid stainless steel shaft which in turn is brazed to the stainless steel plate that has the Indium groove. This plate is held relative to the bottom of the liquid helium reservoir by a skeleton made of 3 copper shafts and 2 copper rings. This structure can be taken off by unbolting at both ends. It is important to note here that all of the pieces of the sample chamber can be taken off and be replaced if any vacuum leaks occur. In contrast, in the SSM1 any bending in the 3 supporting tubes or damage to other parts is irreplaceable.

Wires come down into the sample chamber through 3 stainless tubes that are hard soldered on the top plate and the copper plug block of the liquid helium reservoir. No liquid helium leaks into the sample chamber or into the vacuum space between the liquid helium and liquid nitrogen reservoirs through these 3 tubes . One of these 3 tubings brings in the helium exchange gas while the other two contain the wiring for the sample, SQUID, magnetic coils, and thermometers.

The unique feature about this design is that a sample or the SQUID that is attached directly to the copper plug always maintains the same temperature as the reservoir. The temperature of the end of the scanning shaft, depending on how loosely it couples to the reservoir or the pressure of the exchange gas, can be regulated with a heater. It is possible to do an experiment where the SQUID is at 4K and the sample is at 90K. In the SSM1, heating of the sample is not possible because of the high pressure of helium exchange gas used to cool the SQUID below its transition temperature (~ 9K); and heating the sample would heat up the SQUID.

4.3.2 Operation and Results

The SSM2 is in the advanced stage of completion. All the parts have been built and are waiting to be welded together. We estimate that the major heat leak of the SSM2 is in the scanning shaft. For a shaft of about 50cm long and diameter of 3/4" and 1/16" wall the heat entering the sample chamber is estimated to be about 100mW. One watt of heat entering the liquid helium reservoir boils off about 1.4 liters of liquid helium per hour. A full transfer of liquid helium should last about 8 hours of data acquisition. By pumping on the helium it is possible to get the temperature inside the sample chamber down to 1.2K. Images would be undistorted up to 1cm x 1cm with the new welded bellows.

In practice, we only image (128 pixels x 128pixels) a small region (~ 0.5mm x 0.5mm) of a 1cm x 1cm sample. A scanning range up to 1cm x 1cm allows us to image any region of the sample we wish. It is possible to study many interesting patterns such as triangular arrays, Penrose arrays, clusters, ladders, etc. packed into a sample. Once a sample is loaded (good luck Mark Wistrom!) many weeks of data acquisition are possible before opening up the system and changing the samples.

Chapter 5

Experimental Results

In this chapter we will present experimental results of imaging magnetic vortices in niobium networks by Scanning SQUID Microscopy. We will start out in section 5.1 by discussing magnetic images obtained by the SSM1 and explaining all the interesting features that are inherent in the instrument. In section 5.2, imaging vortex configurations at low rational f in large square Nb networks is demonstrated. We will compare the experimental data to the predicted ground state vortex configurations. Since our samples have few structural defects, disorder in the vortex lattice at low fields is attributed to rapid cooling of the sample. Vortex lattices at irrational f and $f=0$ are also shown. In section 5.3 we will show interesting experimental data on an ensemble of clusters(1x1, 2x2, and 3x3 cells) cooled under different fields f. By modeling the network as a Josephson junction array near the Niobium transition temperature, we attempt to explain the probability of achieving certain vortex configurations. Section 5.4 is the study of the dynamic of vortices in square networks. Here we injected current into the sample and studied how the trapped vortices move in the grids. The results indicate that vortices move perpendicular to the bias current (due to Lorentz force) as well as along and against the direction of the current. Creation and destruction of vortex-antivortex pairs are also observed.

5.1 Vortex Images

Figure 5.1 shows a typical vortex image of a square array (cell size of 20μm x 20μm) obtained with the SSM1. The sample is at 7K and is cooled through its transition temperature in a small residual field. The black dots in the image are trapped vortices in the network. The magnitude of the field measured with a SQUID at this point is about

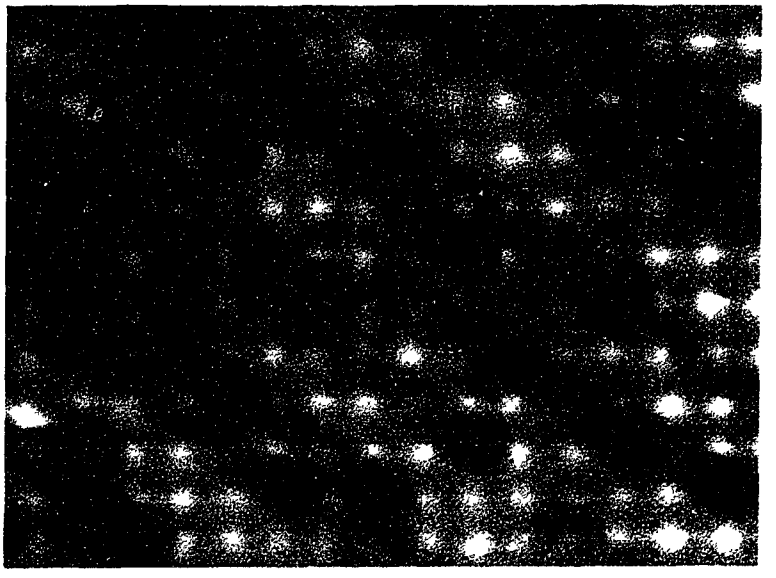

Figure 5.1 : Vortex image of square network at $f \sim 0.12$.

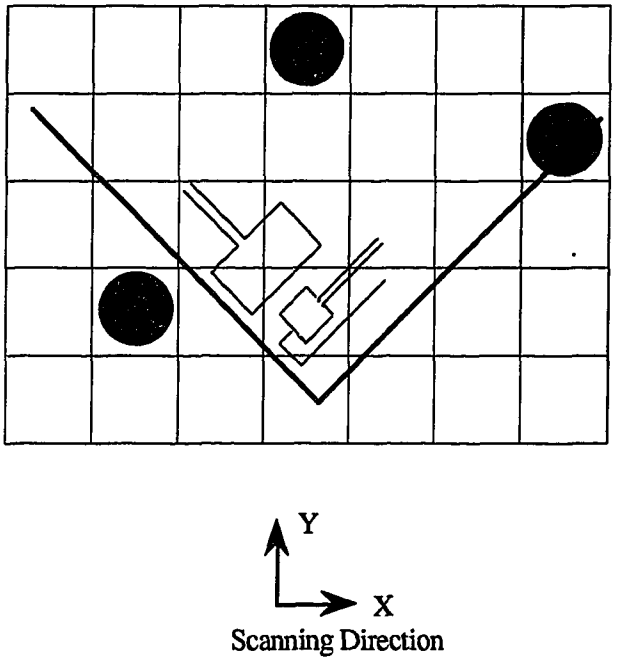

Figure 5.2 : SQUID orientation with respect to the array during scanning.

1/8 Φ_0. This field magnitude corresponds to a distance of 7μm (estimated from our calculations) from the SQUID to the sample surface. Furthermore, from observing the smallest feature in the image, we conclude that our system has achieved less than 10μm spatial resolution.

Besides the trapped vortices, we also see the underlying superconducting lattice. This is due to the Meissner effect in the niobium which shields out the field from the modulating coil to the SQUID. When the SQUID is over an island of the superconductor, the modulating coil must supply an extra amount of flux, which reads out as a voltage in the flux-locked mode. By changing the dc current in the modulating coil, we can tune the contrast of the grid with respect to the vortices. Changing the height of the SQUID to the sample also changes the contrast of vortex image to grid image in a similar manner. This effect in our system is not seen in other imaging techniques such as Hall probes[1] and is of great advantage when imaging vortices in non-periodic superconductor networks such as the Penrose array.

In our images we also see streaks at about 45° around the vortices. This is because our SQUID is rotated 45° (see figure 5.2) with respect to the sample during scanning and the asymmetry of the modulating coil with respect to the SQUID contributes to the smearing of the images. When the modulating coil is directly on top of a vortex, the field of the vortex opposes the modulating field and an extra field from the modulating coil is needed to maintain constant flux in the SQUID. This in effect causes streaks that extend over about 60μm distance, which corresponds to the loop size of the modulating coil. By aligning the SQUID parallel to the array, the streaks are no longer at 45° but are line up with the grids (figure 5.3). In principle, we can eliminate the smearing of the image by designing a SQUID so that the modulating coil will have rotational symmetry with respect to the SQUID loop. One configuration for obtaining rotational symmetry is to fabricate the modulating coil directly on top of the SQUID loop. Introducing symmetry in the SQUID

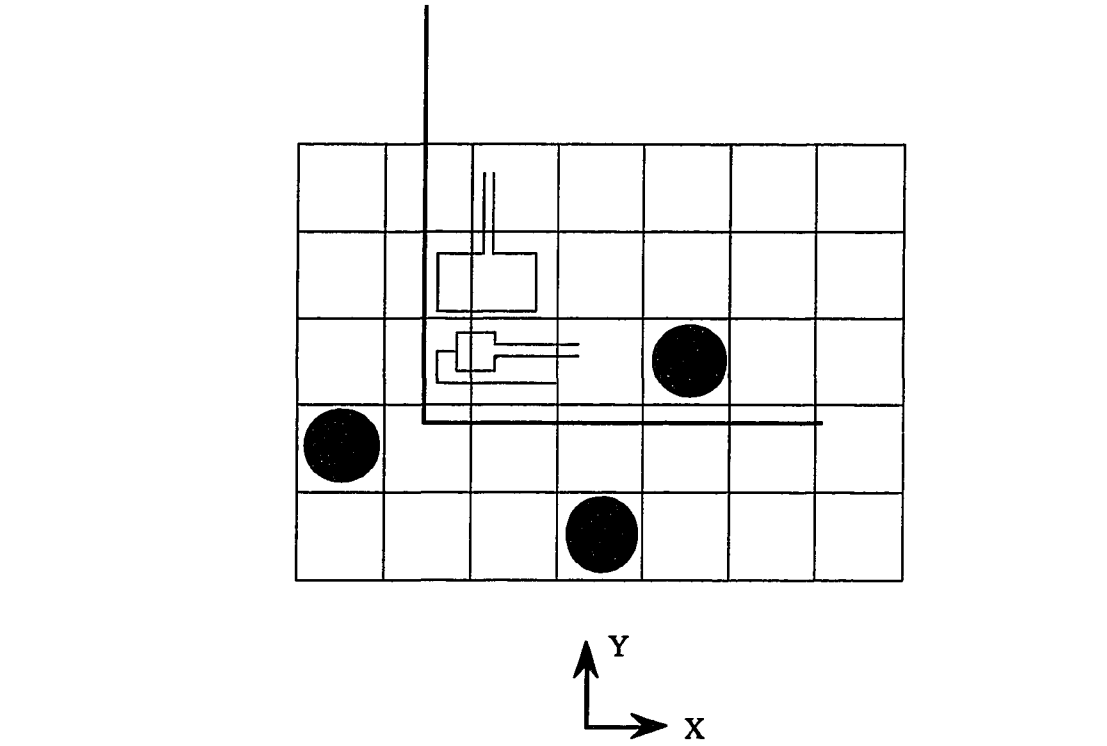

Figure 5.3 : Vortex image as a consequence of aligning the SQUID parallel to the array. Note that streaks are now along the Y-axis.

also reduces the contrast of the superconducting grids. It is interesting to note that in our asymmetric SQUID design, we can still see the superconducting grids of filament size as small as 0.2μm !

To establish that black dots in our images are really vortices, we cooled the array under different applied magnetic fields. In theory, the density of vortices in the array should be linear with the applied field. For a particular applied field we counted up all the vortices, regardless of the vortex configuration, in the scanned area. By dividing that by the total number of cells in that area we obtain the vortex density and this value is the same as $f \equiv \Phi_a/\Phi_0$. The result is shown in figure 5.4 . As expected, the current in the coil scales linearly with the vortex density. As the applied magnetic field is increased more vortices are induced in the network. From the linear slope, 1 mA in the Helmholtz coil can induce a vortex density of f=0.242 . For every milliamp of applied field the Helmholtz coil generates a uniform magnetic field of 17.4 mG to the array. For this set of data, no applied field corresponds to a residual field of about f~0.3. This is the earth field that is not shielded out by the mu-metal and is about 22mG. By applying an opposing field with the Helmholtz coil, we can null out the residual field entirely.

5.2 Vortex Configurations vs. f in Square Arrays

Ground states of vortex configurations in square arrays have been studied extensively by many theorists[2,3,4]. At rational values of f, vortices are predicted to be commensurate with the grid. In other words, vortices align themselves in a periodic lattice that 'matches' the underlying superconductor lattice. Not until recently has it been possible to image these vortices in the arrays. In this section we will present our experimental results of vortex configurations at low rational and irrational values of f. We will also show the result in zero field.

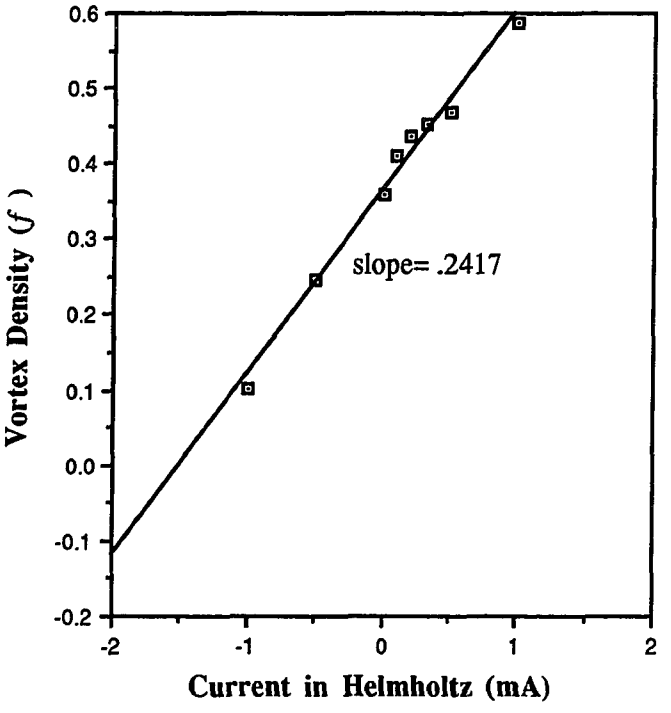

Figure 5.4 : Vortex density (f) versus current in the Helmholtz coil.

5.2.1 Vortex Images at Fractional f

Figure 5.5 shows experimental data of vortex configurations for $f \sim 0$, 1/5, 1/3, 1/2, 2/5, and 2/3 along with the predicted ground-state patterns. We first applied a magnetic field in the Helmholtz coil that corresponds closest to a fractional f and then rapidly cooled the sample (~5K /sec) through its transition temperature. The final temperature of the sample was about 6.5K and the images were taken with the applied field on at all time. We scanned only a small part near the center of a 1cm x 1cm sample.

In the image at f=1/2, the vortices distribute themselves in a checkerboard pattern with evidence of domain walls that separate regions of different chirality. The checkerboard pattern has the lowest value of free energy at f=1/2 (figure 3.3), and any disorder of this configuration will increase the free energy of the system immensely. Therefore, it is very likely to achieve the ground state vortex pattern when the array is cooled in a field of f=1/2. In our image, the checkerboard pattern extends over at least distance of 300μm before hitting another checkerboard pattern of different chirality. The cause for this is that the different regions of the array nucleate into a local vortex pattern independently and when the whole sample is 'frozen', regions of different vortex patterns meet and give rise to domain walls. Defects of cell sites and inhomogeneity in the superconducting film are regions where domain walls most likely to occur.

At f=1/3 there are six possible degeneracies competing. The vortex pattern never extends beyond distance of six lattice spacing. This is as expected since the dip at f=1/3 in the free energy curve is not as pronounced as f=1/2. The image for f= 2/3 looks just like f= 1/3 if the picture is made negative. This result agrees with theory since the Hamiltonian (equation 3.4) is invariant under (1-f) transformation where $0 \leq f \leq 1/2$. Images for f=2/5 agree very well with prediction while f=1/5 and 1/4 show more disorder. This is understood because the dip in free energy vs. f curve at f=2/5 is stronger

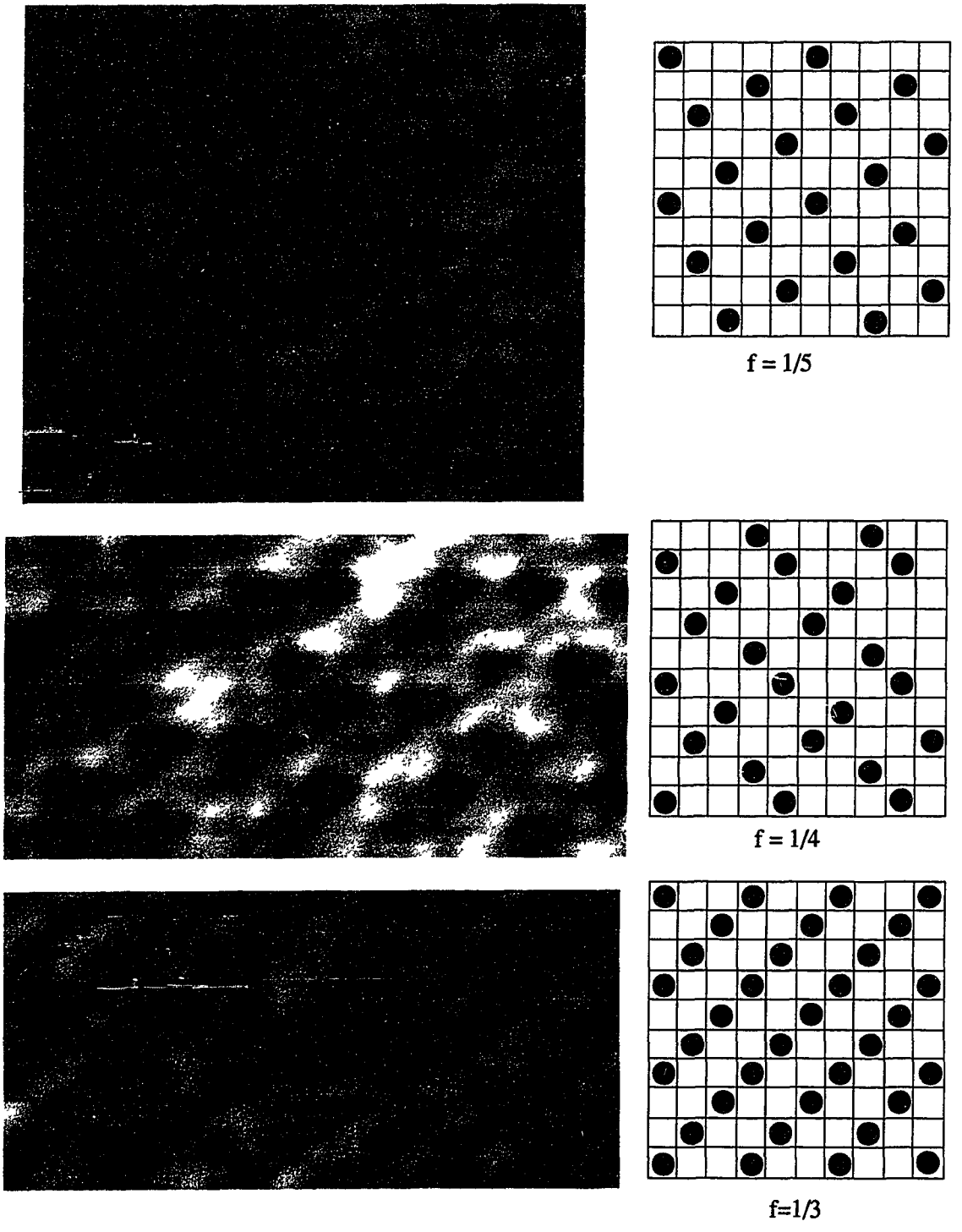

Figure 5.5 : Vortex images at rational values of f along with their predicted ground state configurations.

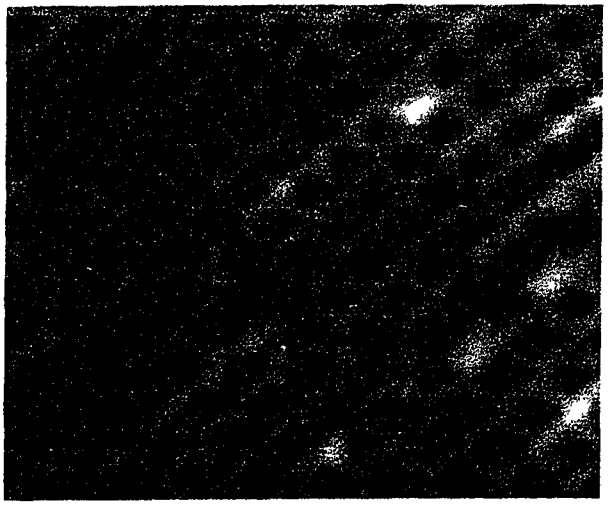

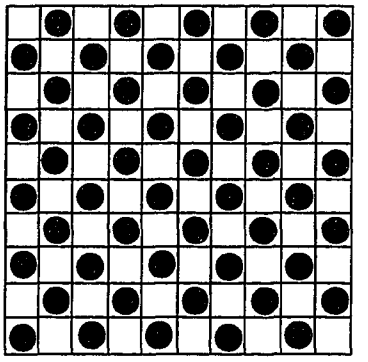

f = 1/2

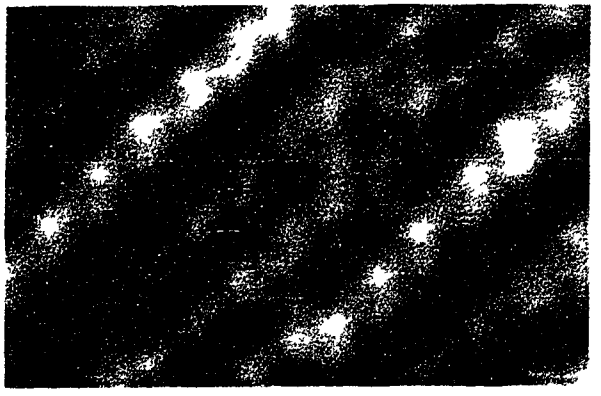

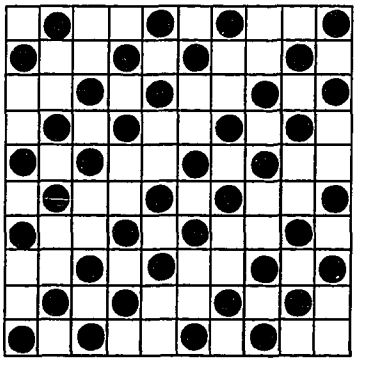

f = 2/5

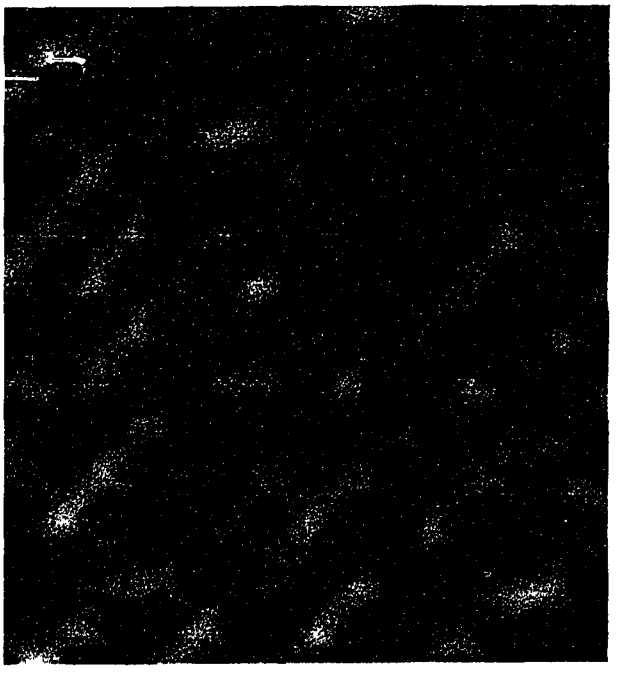

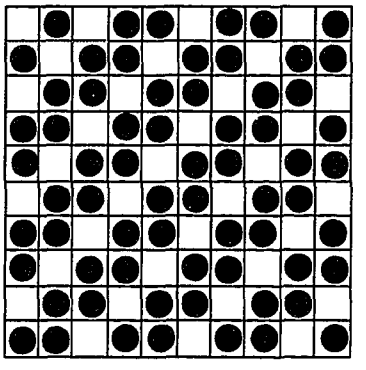

f = 2/3

Figure 5.5 (continued)

than f=1/5 and 1/4. At f=1/5 and 1/4 vortex spacing is far so interactions of vortices are weak and rapid cooling can cause vortices to trap in a nonequilibrium metastable state.

In our experiment, the Nb superconducting arms that define the cells of the network at 6.5K behave like a bulk superconductor. A vortex trapped in a cell at this temperature can not move by thermal activation and reducing the temperature of the sample down to 0K will not change the vortex configurations. Only very near the transition temperature do vortices move in networks. This range of temperature where vortex motion occurs is very narrow, < 100 mK in niobium. If the allowed time of cooling is not long enough, the vortices do not have enough time to align themselves into an ordered state of minimal energy. Defects in the array can also cause disorder in ground state vortex patterns. In our samples, the variation of cell areas across the sample is less than 1% and there are very few structural defects. We conclude that the main reason for disorder and the existence of domain walls in our vortex images is due to rapid cooling.

5.2.2 Vortex Images at Irrational f

The inverse of the golden mean defined as $\tau^{-1} = \frac{\sqrt{5}-1}{2} = 0.6180....$ is considered as the most irrational number. The number τ occurs in the form of the ratio of the areas of larger unit cell to the smaller unit cell in special quasi-periodic lattices (Penrose lattice); some crystals existing in nature have been identified to have quasi-periodic lattices. Halsey[5] predicted that at f=1-τ^{-1} (~0.382) the ground state vortex lattice in a square array is quasi-periodic locally. Figure 5.6 shows our results when the array is cooled in a field of f~0.38 along with the ground state vortex pattern proposed by Halsey. Our results do not indicate any similarity to the predicted ground state pattern. Fang Yu[6] has done some simulation in square arrays at f=1-τ^{-1}. In his 200 trials of cooling down the array, he never once reached the minimal energy state predicted by Halsey. The final energies of those 200

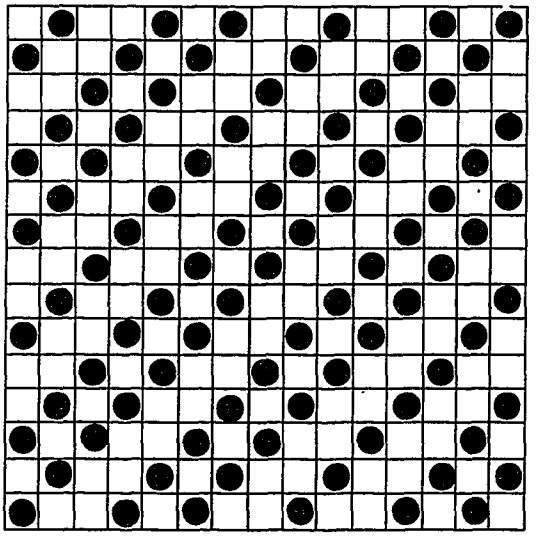

a) Ground state predicted by Halsey
Energy=9.5358 (arbitrary units)

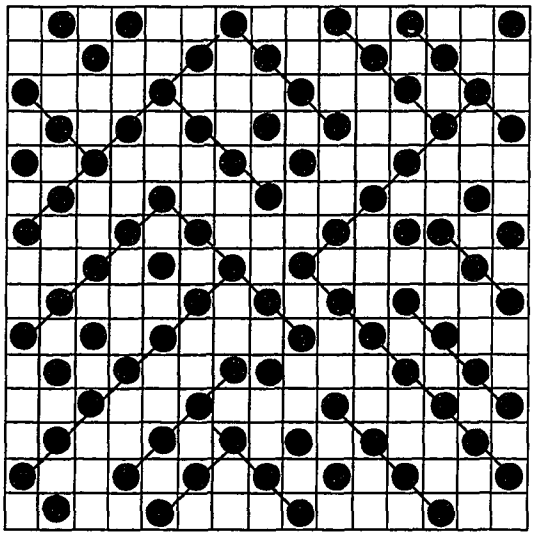

b) Lowest energy state simulated by F. Yu
Energy=9.6250 (arbitrary units)

c) Vortex image cooled in a field of $f \sim 0.38$

Figure 5.6 : Vortex pattern at $f=1-\tau^{-1}$ along with Fang Yu simulation (obtained using 200 random patterns) and Halsey's proposed ground state.

metastable states are very close to Halsey's prediction and for this reason it is very difficult to achieve the ground state if the sample has some defects and the cooling rate is too fast.

At other irrational f theorists have predicted that the ground state consists of vortices arranged diagonally. This is similar to the results obtained for the inverse golden mean. We have imaged vortices in arrays at a few irrational f (figure 5.7) and found that the vortex patterns always appeared to be random and not commensurate with the underlying grids. We believe that in order to achieve these ground state patterns, the sample must be cooled down adiabatically. This requires a decrease in the cooling rate of several orders of magnitude or fabricating a superconducting weakly-coupled array.

5.2.3 Vortex Images at f~0

In zero field, Josephson arrays are believed to undergo a Kosterlitz-Thouless phase transition.[7] In wire networks it is not clear that the system undergoes KT transition, although one group[8] has seen evidence that wire networks undergo Kosterlitz-Thouless (KT) phase transition in zero field. In the KT transition, vortices and antivortices are thermally created and bound in pairs in the array. Above a certain critical temperature, defined as T_{KT}, these pairs are screened and eventually break apart. These free vortices are free to move through the cells of the array in the presence of current and create a finite voltage. It is the statistics of the depairing process of vortex-antivortex pairs that characterizes a KT transition. If networks indeed exhibit a KT transition, then it is possible to trap vortex-antivortex pairs by quenching the sample through its transition temperature at $f = 0$.

Figure 5.8 shows a magnetic image of the wire network when cooled in zero field, $f = 0$. The image showed five vortices in the lower right corner and five antivortices in the upper left corner. Since there are no net vortices of one sign, it is likely that these vortices and antivortices are induced from cooling in a small nonuniform magnetic field.

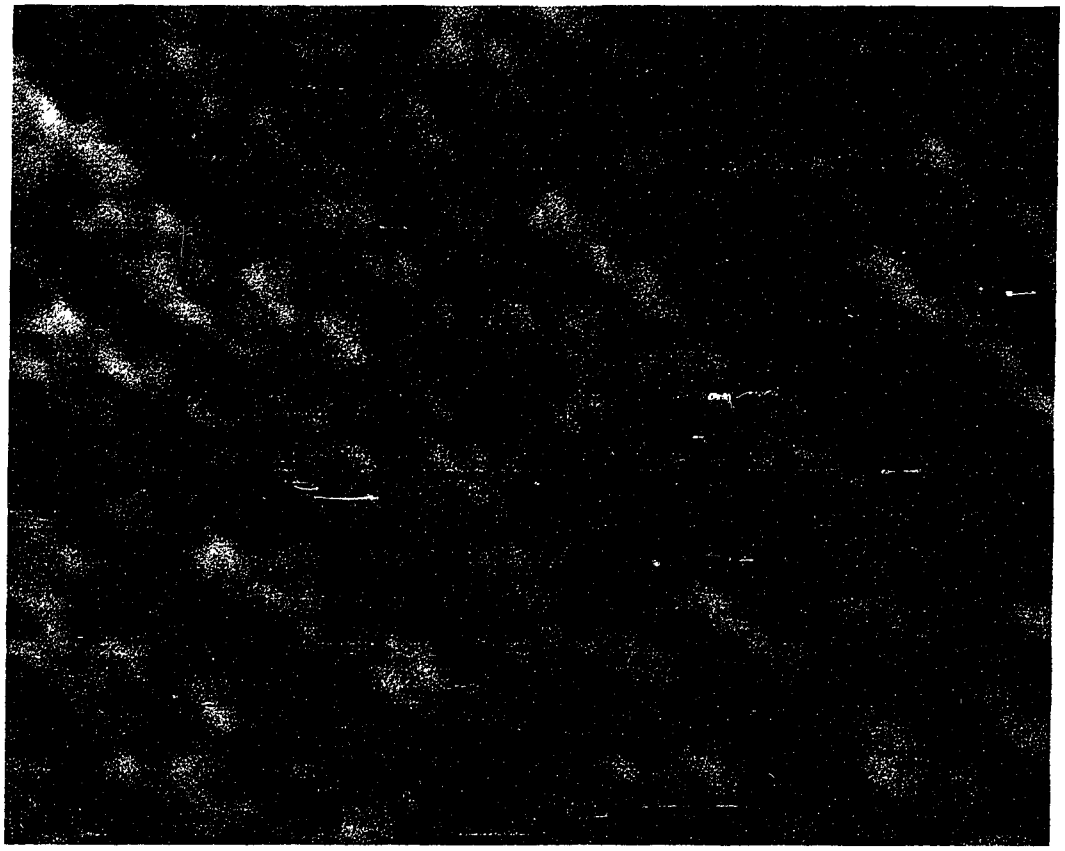

Figure 5.7 : Vortex pattern at $f \sim 0.28$, a nonspecial irrational number that does not correspond to any nearest rational f that have pronounced dips in the free energy vs. f curve.

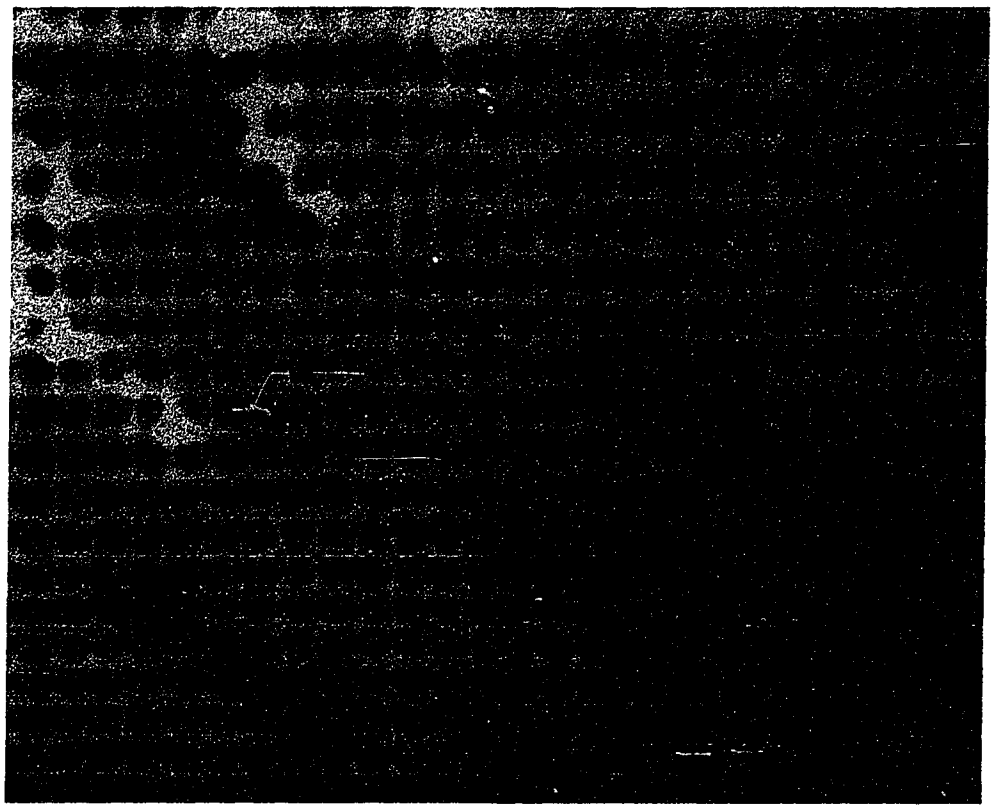

Figure 5.8 : Vortex pattern at $f=0$. Black dots are vortices and white dots are antivortices.

We have observed stable bound vortex-antivortex pairs in zero field. At finite f, however, we have occasionally observed vortex-antivortex pairs (figure 5.9). These pairs are stable but can annihilate at a later time because of thermal fluctuations. We found by injecting current into the array it is possible to create more vortex-antivortex pairs. We will discuss this effect in section 5.4.

5.3 Vortex Configurations in Clusters

The physics of large superconductor arrays is very complex because there are many possible vortex configurations at any applied field. As we have seen so far, only for values of rational f the ground state vortex lattices are commensurate with underlying grids. Experimentally, it is almost impossible to achieve a ground state vortex pattern unless the sample is cooled through its transition temperature infinitely slow. At finite cooling rate, fluctuations are important and a finite probability of trapping a system in other excited states exist, with the ground state being the most probable. The result is that some regions of the array would achieve the ground state pattern while other regions would show disorders. This is exactly what we saw when we scanned over a large region of the array at a fractional f. In theory, it is possible to predict the probability of achieving a vortex configuration at a value of f if the energy vs. f curve of all the possible vortex configurations are known. To limit the number of possible vortex configurations we turned to clusters which are defined as small arrays (usually less than 10cells x 10cells).

In this section we have studied the statistics of an ensemble of square clusters: 1x1, 2x2, and 3x3. At a particular f we imaged vortices in an ensemble of clusters and looked at the probability of capturing a vortex configuration. From the probability curve vs. f and a free parameter k_BT, we can deduce the energy curve using the partition function. By comparing this data to our simulation, where we have assumed each niobium wire defining a unit cell to represent a Josephson junction, we can deduce the barrier height of

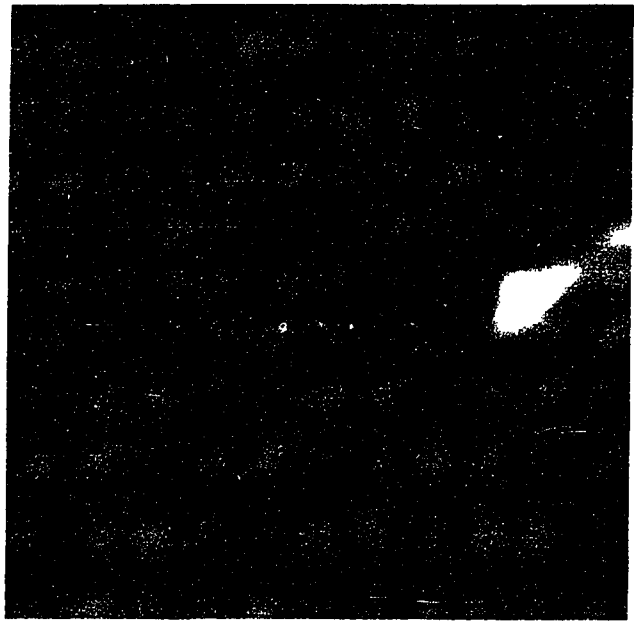

Figure 5.9 : Vortex-antivortex pair in large square array at f~0.3.

a potential well that a vortex sees when hopping into the next cell. Sections 5.3.1, 5.3.2, and 5.3.3 show the results of the 1x1, 2x2, and 3x3 clusters, respectively.

5.3.1 1x1 Clusters

Figure 5.10 shows the sample of an ensemble of 1x1 clusters (rings). The sample has 250 x 250 clusters where each 1x1 cluster is of size 20μm x 20μm. The center to center spacing of the rings is 40μm, which is large enough that the rings can be considered to be uncoupled. The clusters are fabricated by sputtering 1200Å niobium film on silicon substrates. The clusters have line width of ~ 2μm. The sample was cooled in a field through the transition temperature at a rate of 1K/sec. At a given value of field, we only scan a small region of the 1cm x 1cm (consisting of ~25 clusters) of the sample to obtain a distribution of clusters that have one vortex.

Figure 5.11 shows the probability data for 25 clusters. It is interesting to note that probability curve is a very slow varying function of f. Even at $f>0.7$, there is always a finite probability of capturing a zero vortex state.

Analysis:

We have done simulations by modeling the clusters as a ring with 4 Josephson junctions (see figure 3.8). Assuming all the junctions have a uniform coupling energy E_J, we can calculate the energy of the system for an applied field f by using equation 3.4. The result is shown in figure 3.9 for $\beta_L=2\pi L i_C/\Phi_0=0.12$. In figure 3.9, the black curve indicates the energy of a cluster with no trapped vortices, and the white curve shows the energy of a system for one trapped vortex. At a particular value of f, there are two possible states which we identify as $\varepsilon_0(f)$ and $\varepsilon_1(f)$, corresponding to a system of zero vortex and one vortex respectively. Assuming thermal equilibrium at a finite temperature and value of f, the probability of capturing a single vortex is just

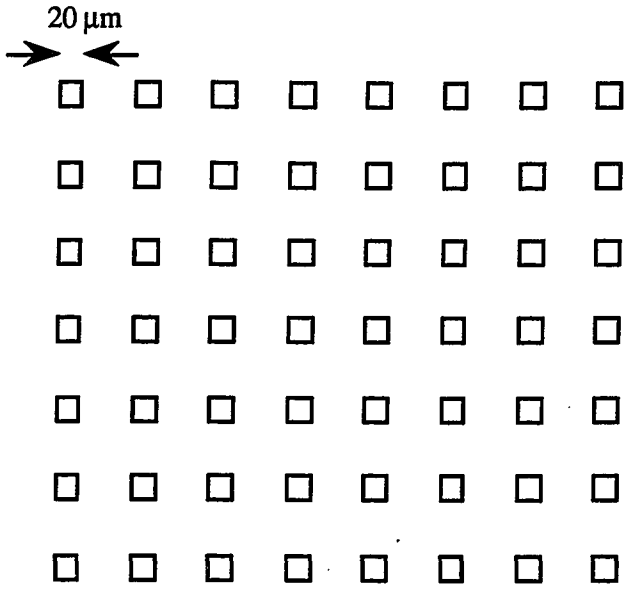

Figure 5.10 : Sample consisting of an ensemble of 1x1 clusters (rings). Each ring has size of 20µm x 20µm and niobium linewidth of 2mm. The spacing between each cluster is 40µm.

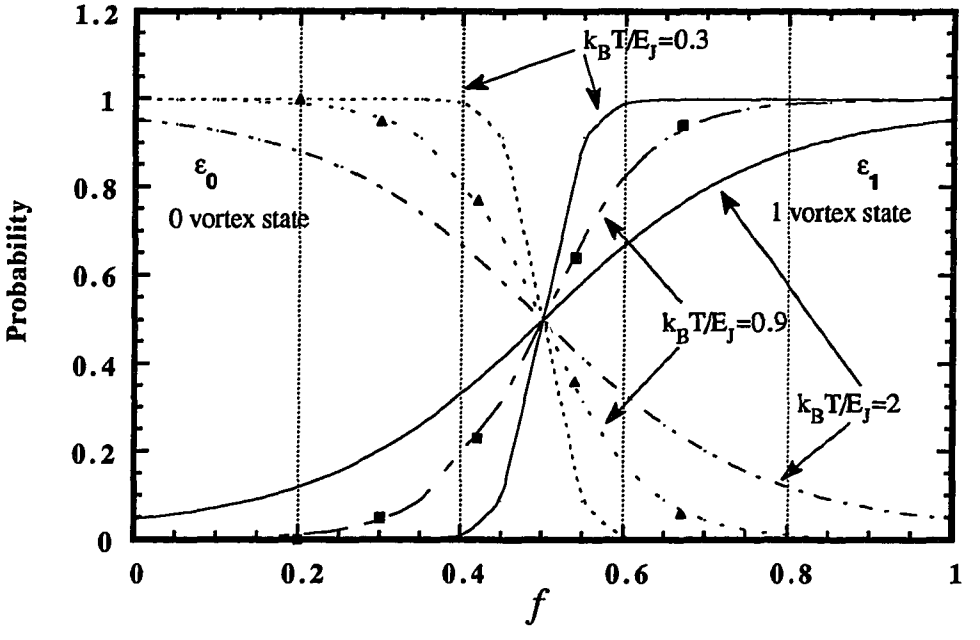

Figure 5.11 : Probability data and fitting curves (from our simulations) for 1x1 clusters vs. applied field f.

$$P_1(f) = \frac{e^{-\varepsilon_1/k_BT}}{Z} \tag{5.1}$$

where Z is the partition function defined as

$$Z = e^{-\varepsilon_0/k_BT} + e^{-\varepsilon_1/k_BT} \tag{5.2}$$

and T is the temperature. The probability for a cluster to be in a zero vortex state is just $P_0(f)=1-P_1(f)$. From the energy curve we have calculated the $P_0(f)$ and $P_1(f)$ and fitted to our data, shown in figure 5.11. From the fitting, we see that the probability curves, $\varepsilon_0(f)$ and $\varepsilon_1(f)$, vary greatly with temperature while the parameter β_L has little effect. Our data fit best when $k_BT \sim 0.9E_J$. Our interpretation of this result is that a vortex does not get trapped in the potential until the thermal energy of a vortex is equivalent to the barrier energy, $U_b=0.9E_J$ (see section 3.2.3), of the cluster as shown in figure 5.12. Since T_c of niobium is very sharp at about 9K, we can take $T \sim T_c$ and deduce that the Josephson energy of a junction in a 1x1 cell is just $E_J \sim k_BT_c/0.9 = 1.24 \times 10^{-24}$J. With this coupling energy we calculate the critical current of a junction to be $i_c=0.4\mu$A. The inductance of a superconducting loop is approximated by $L=\mu_0 s$, where s is the circumference. For a cell of 20μm x 20μm, the inductance is therefore about 100pH. With the known values of i_c and inductance, we calculate β_L to be about 0.12. So very near to the transition, a 20μm x 20μm superconducting loop can be treated as loop of four Josephson junctions loop of $\beta_L = 0.12$.

5.3.2 2x2 Clusters

Figure 5.13 shows a sample of 2x2 clusters. Again, we are interested in measuring the probability of capturing a certain vortex configuration at a value of f in a 2x2 cluster. Figure 5.14 shows a vortex image of an ensemble of 2x2 clusters at $f \sim 0.3$. We have measured the vortex configurations of 25 clusters for different values of applied field. The data is shown in figure 5.15.

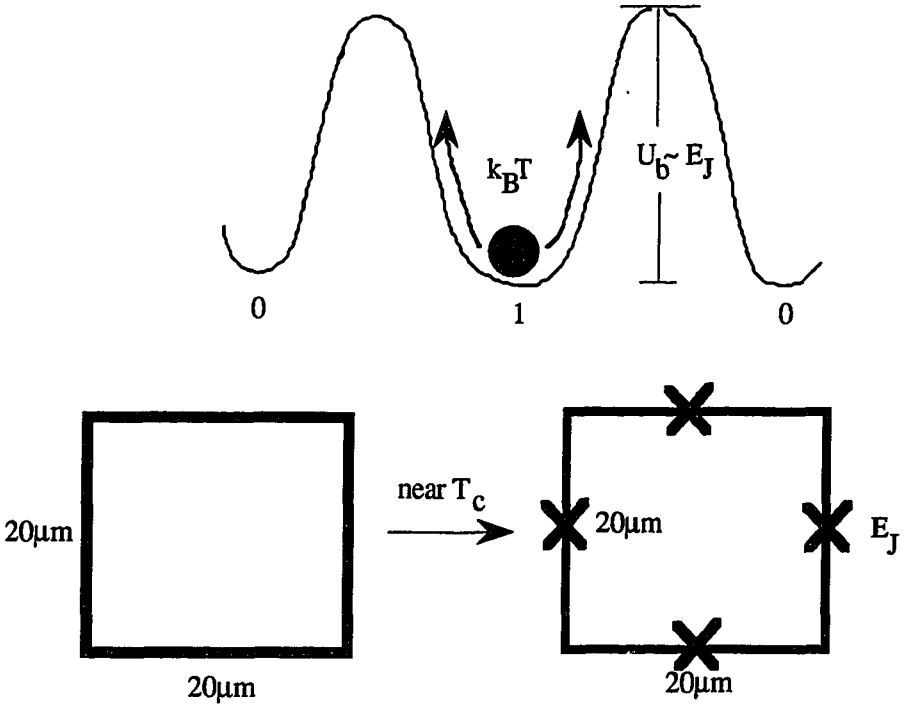

Figure 5.12 : Modeling of a 1x1 cluster with a 'single vortex model' near the transition temperature of niobium. At temperature where $k_BT=U_b$, the system has a finite probability of locking in a vortex.

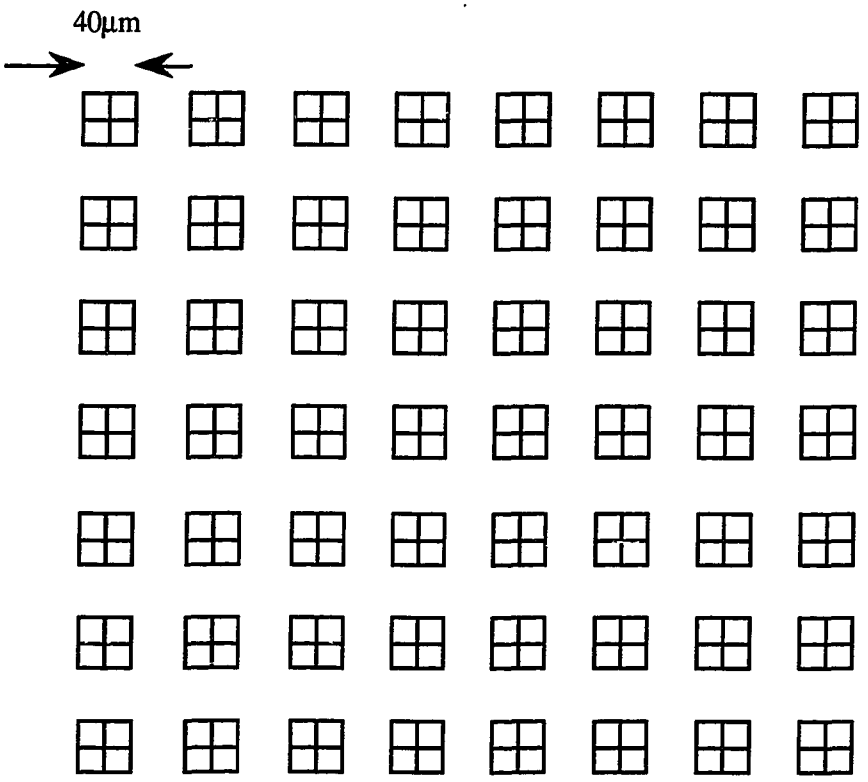

Figure 5.13 : Sample consisting of an ensemble of 2x2 clusters. Each unit cell of a ring 2x2 cluster has size of 20μm x 20μm and niobium linewidth of 2mm. The spacing between each cluster is 40μm.

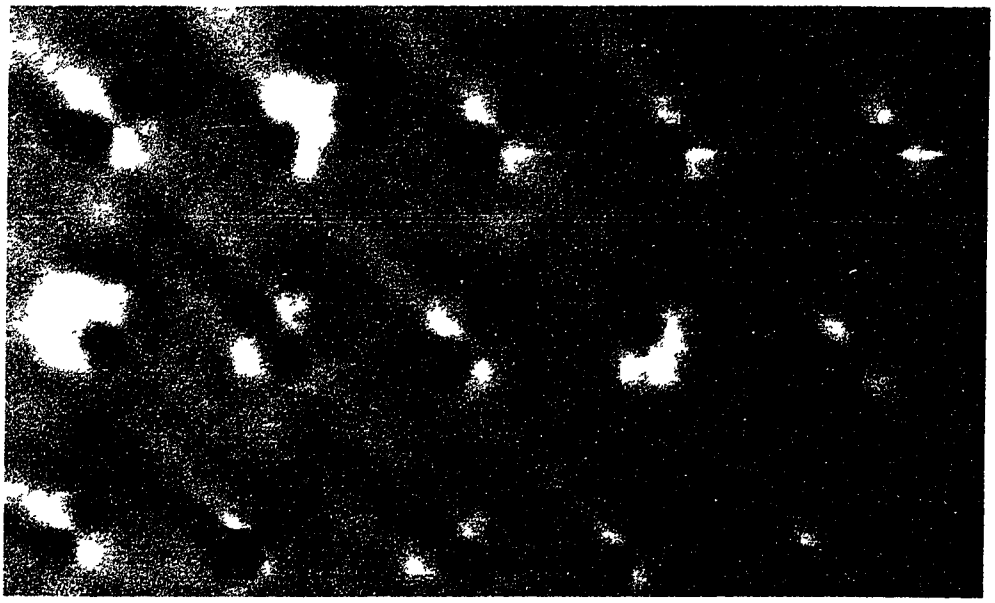

Figure 5.14 : Vortex image of an ensemble of 2x2 clusters at f ~0.3.

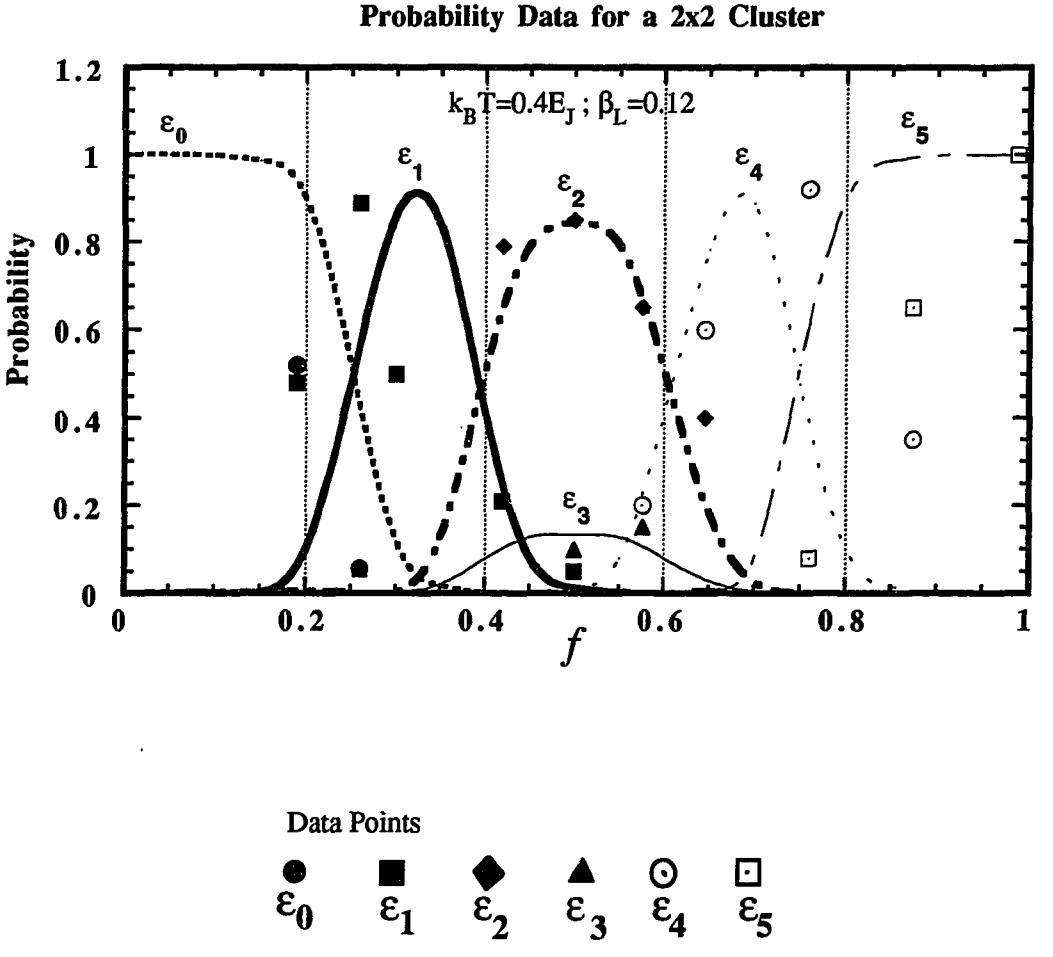

Figure 5.15 : Probability data and fitting curves (for β_L=0.12 at k_BT=0.4) for 2x2 clusters vs. applied field f.

Analysis:

We have done simulations for 2x2 Josephson junction clusters for β_L=0.12, the value deduced from the single cell clusters. The energy curve vs. f for a 2x2 Josephson junction cluster of parameter β_L=0.12 is shown in figure 3.9. From this energy curve we can calculate the probability of capturing a vortex configuration as described in section 5.3.1. For example, the probability of capturing a single vortex is just

$$P_1(f) = \frac{4e^{-\varepsilon_1/\beta}}{e^{-\varepsilon_0/\beta} + 4e^{-\varepsilon_1/\beta} + 4e^{-\varepsilon_2/\beta} + 2e^{-\varepsilon_3/\beta} + 4e^{-\varepsilon_4/\beta} + e^{-\varepsilon_5/\beta}} \qquad (5.3)$$

The coefficients in front of the exponential terms of equation 5.3 represent the degeneracies of that state. For example, state ε_3 has two vortices and there are two ways of rearranging the two vortices. Figure 5.15 shows the fit to our data. The probability function is very sensitive the temperature parameter. Our simulation result fits best to the data for $\beta=k_BT\sim0.4E_J$. This suggests that the barrier height of the 2x2 at which vortices locked in is about $0.4E_J$. According to the 'single vortex model', the potential for a 2x2 cluster is shown in figure 5.16a). This potential is not quite correct because of edge effects which were not considered in the 'single vortex model'. Rao and Van Harlingen[9] have accounted for the corrections and calculated the potential for a 2x2 cluster at T=0K for f~1/4. The result is shown in figure 5.16b). In this model there are two barrier heights, one is the barrier height ($U_1\sim0.3E_J$) of hopping from one cell into the adjacent cell and the other is the escaping barrier height ($U_2\sim0.8E_J$). What we measure is probably the mixture of U_1 and U_2.

5.3.3 3x3 Clusters

We have also obtained vortex images on an ensemble of 3x3 clusters for various values of f. In figure 5.17 at low value of field f~0.1, the cluster either has one or zero vortex. For larger field f~0.6, many possible configurations of 4, 5, 6, and 7 vortices

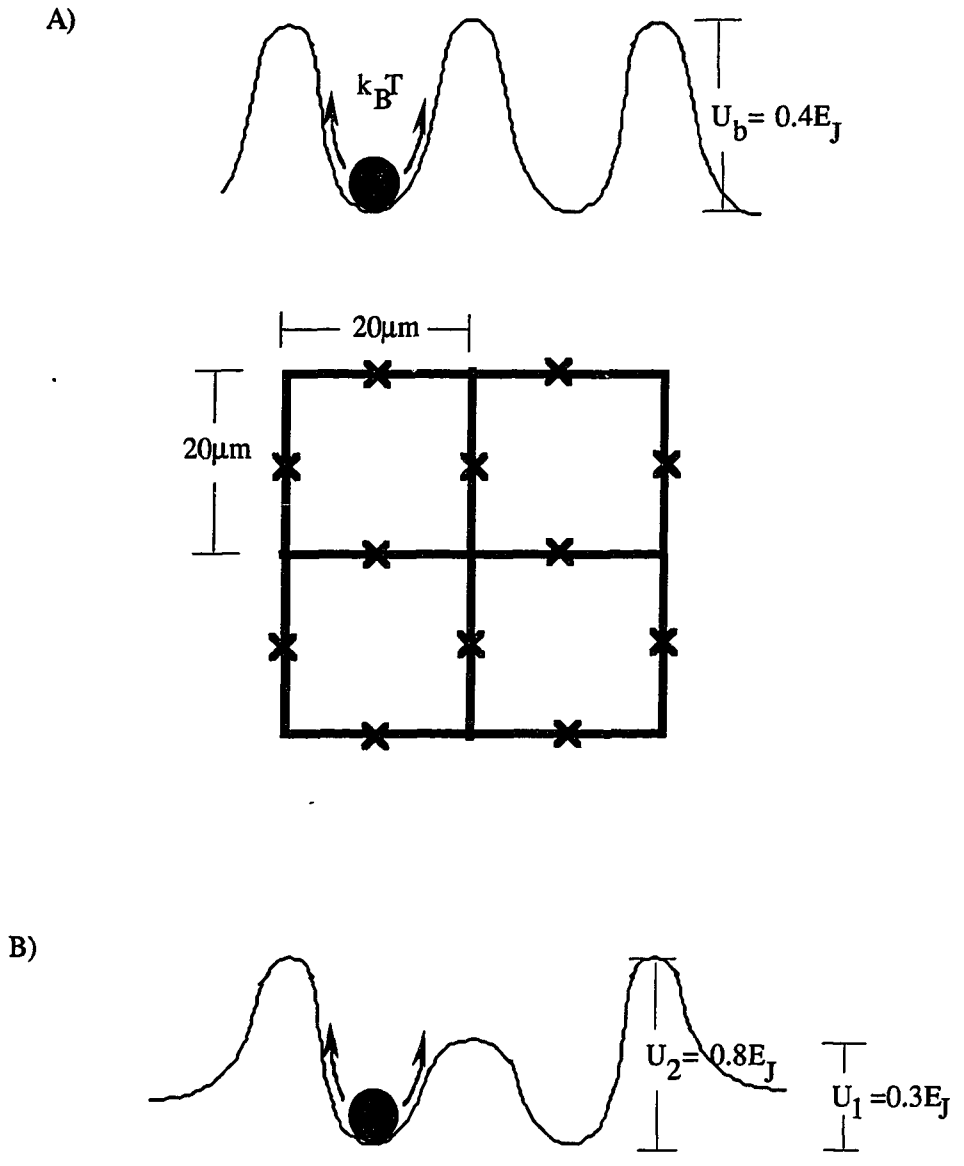

Figure 5.16 : Vortex potential for a 2x2 cluster A) using the 'single vortex model' B) from calculations (for T=0K and f=1/4)by Rao and Van Harlingen which have taken into account of edge effects.

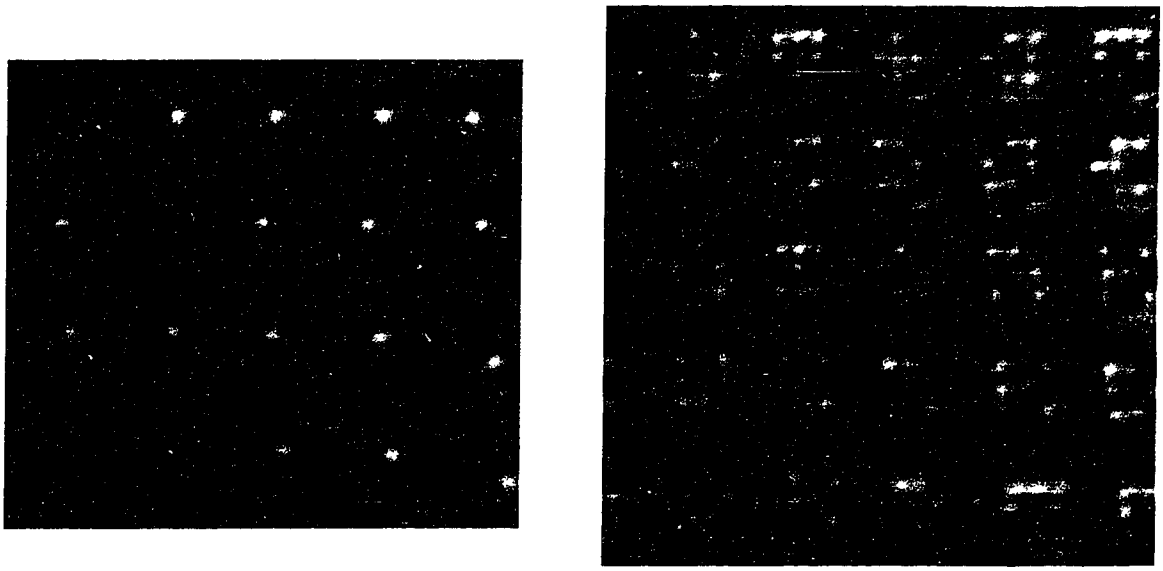

a) b)

Figure 5.17 : Vortex image for an ensemble of 3x3 clusters at a) f~0.1 and b) f ~0.6.

exist. For a 3x3 cluster the total number of vortex configurations is 2^9=512. In order to compare the calculated probabilities to the measured probabilities, all energy curves vs f are needed. Because such a calculation is very complex and we do not have many data points, the analysis has not been performed. The physics of large arrays, therefore, is very complex because the total possible vortex configurations is infinite.

5.4 Vortex Dynamics in Superconductor Square Networks

Our SSM is designed to image static vortex configurations in arrays and clusters. The instrument is also suited to study vortex dynamics. Here we made an attempt to study vortex dynamics in superconducting networks by current injection. In our experiment, the network is tightly coupled at T=7K. The range of current (up to 60μA/wire) we applied to the sample at this temperature is not sufficient (require ~ 4mA/wire) to depin vortices. We could not increase the temperature of the sample to reduce the pinning potential because raising the temperature of our sample would increase the temperature of our SQUID. We feel that the more appropriate system to study vortex dynamics is the Josephson junction array. Vortices in this system are weakly pinnned to the grid and a small injection current (greater than one microamp/wire) is enough to depin a trapped vortex. What we report here are vortex movements among defect sites in the network.

According to the 'single vortex model' (section 3.2.3 and 3.3.2), a current applied to a network will tilt the vortex potential. A vortex trapped in a cell of an array remains trapped until the applied current i is such that $i\Phi_0 \geq U_b$ (assuming the shape of the potential is sinuisoidal). When $i\Phi_0 \sim U_b$, a vortex falls out of its trapped state and travels from cell to cell in the direction perpendicular (due to the Lorentz force) to the applied current. This is known as flux creep. As i is further increased such that $i\Phi_0 >> U_b$, the vortex gains enough kinetic energy to overcome all the barrier heights in the array and

achieves the running state known as flux flow. In the running state, vortices flow resulting in a resistance across the sample. In this experiment, we are interested in measuring the barrier height energy, U_b, in our niobium square network.

Our sample is a square niobium network (unit cell size of 20μm x 20μm and 2μm linewidth) same as shown in figure 3.3. To lower U_b, we fabricated the sample of 800Å Nb thickness instead of 1200Å. Reducing the thickness below 800Å may increase inhomogeneity in the film. In our experiment, we induce a small density of vortices in the array by cooling the sample in a low field. A vortex image is then acquired. Without rewarming the sample, a known dc current (from a low noise, battery operated current supply) is injected into the sample. We then take another magnetic image with this applied current. The procedure is then repeated for a range of applied current. By comparing snap shots (take about 30minutes of scanning per snap shot) of the same region of the grids, we can deduce how the vortices move in the array with applied current. Since our sample has 500x500 cells, there are 501 strands of superconducting wires along the current direction. Therefore, an injection of current **I** induces a current i=**I**/501 into each wire. In our experiment we could not inject more than **I**=±30mA of current into the network without heating the substrate. Apparently, the contact resistance between the indium pad and niobium pad of the array is quite high (~10Ω).

Figure 5.18 a), b), c), d), e), f), g) h), and i) are the data obtained for different values of applied current at $f = 0.12$. The black dots are vortices and the **x** indicate antivortices. We also indicate the temperature of the sample during data acquisition. The temperatures of images f) and i) are slightly higher than others because of the heating due to high injection currents. From a) to f), the current is increased in steps of +5mA of applied current. From f) to g) we turned down the applied current from +30mA to 0mA. From g) to h) and i), we reversed the direction of current and increased in steps of 10mA. The left

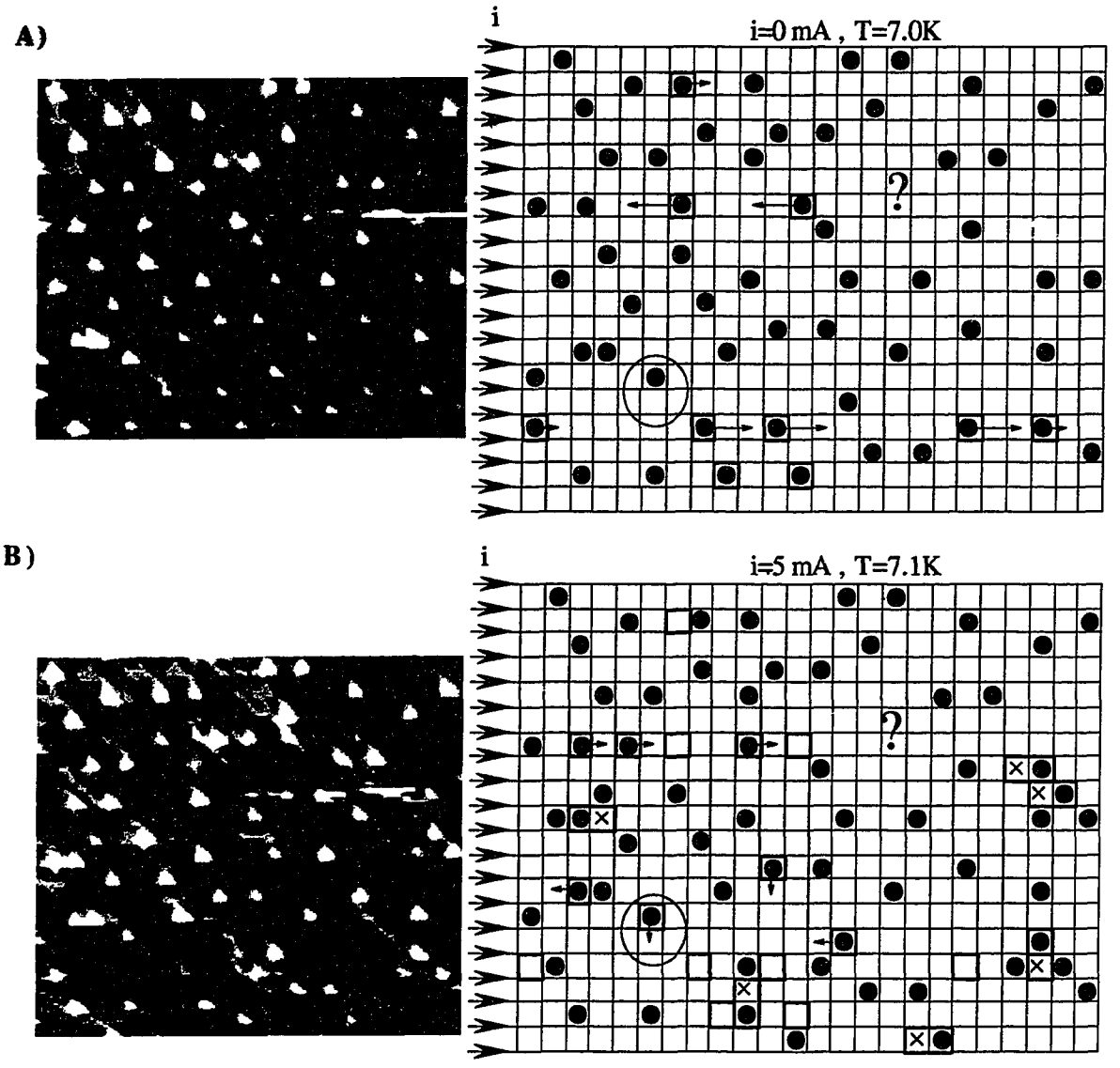

Figure 5.18 : Vortex images for various applied currents. The left side is the raw data and the right side is the digitized image of the data. In all images a) to i) the arrows indicate the motion of vortices. The dark squares mark cells that were previously occupied by vortices. These sites could be defect cells in the network. The region encirced inicate the location where a vortex is observed to hop back and forth between two cells. We label ? to show the region where the SQUID became unlocked.

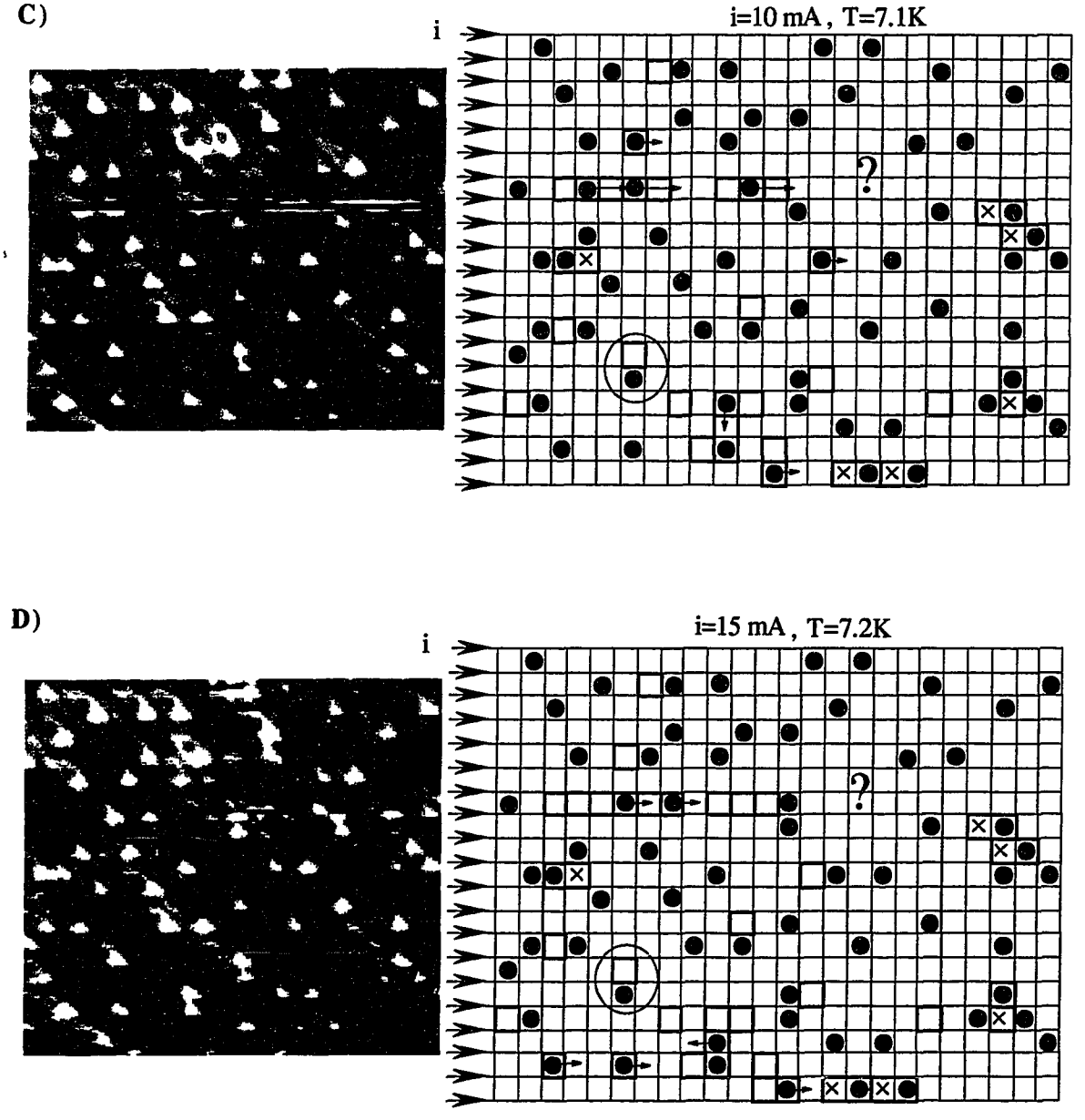

Figure 5.18 (continued)

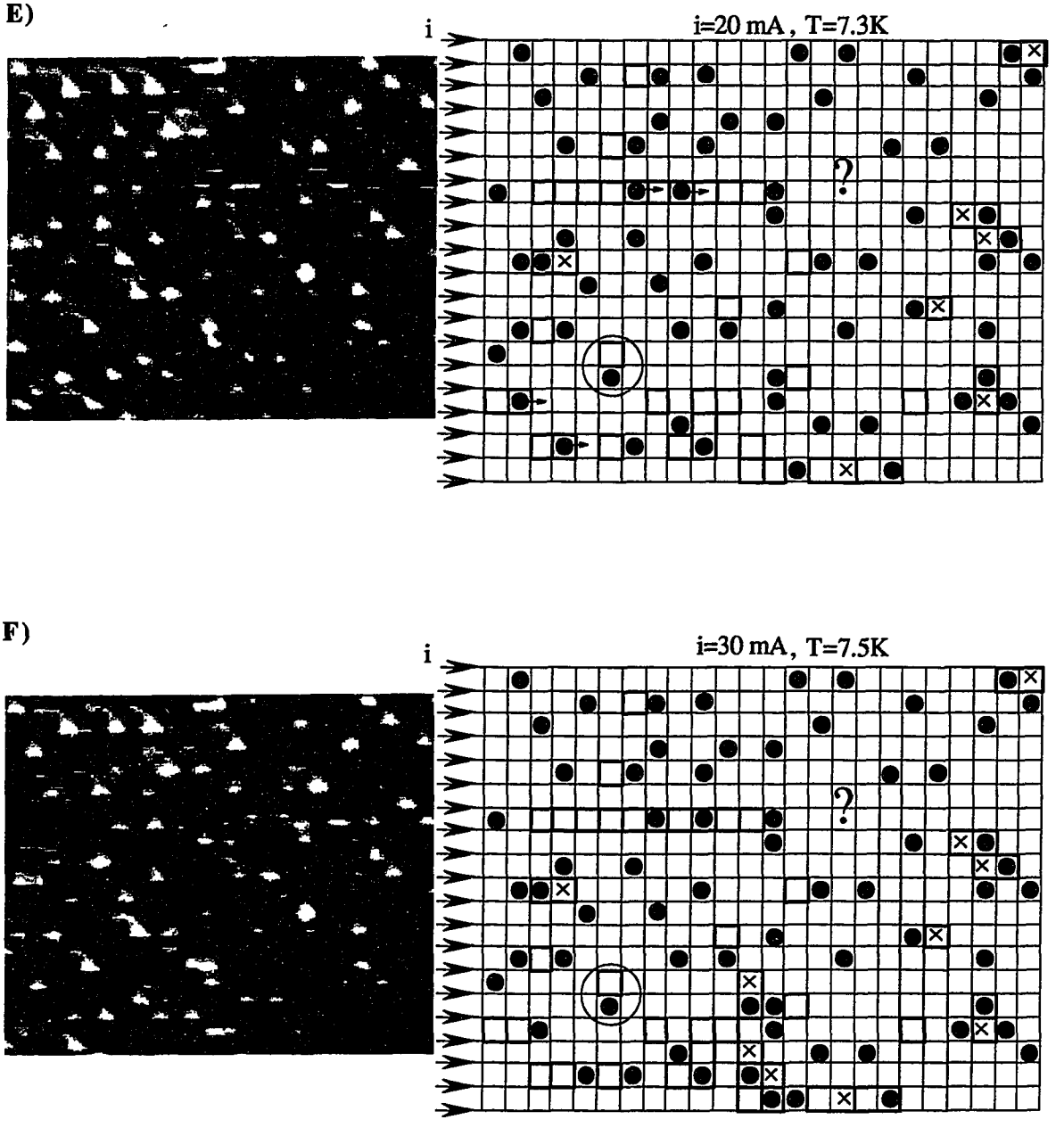

Figure 5.18 (continued)

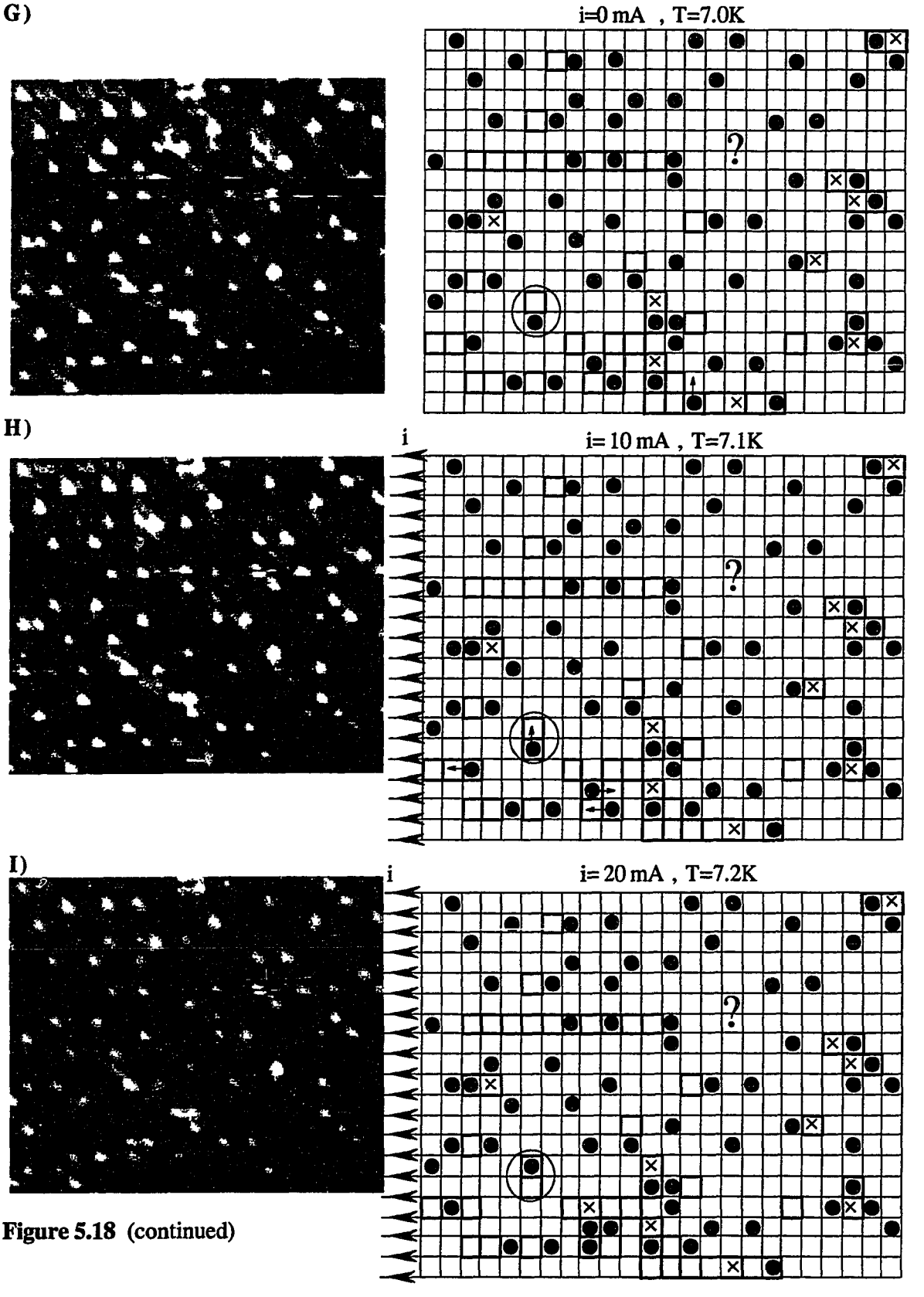

Figure 5.18 (continued)

side of the figure 5.18 shows the raw data and the right side is the digitized image of the raw data. The arrows drawn in the digitized images indicate the movement of vortices. For example in figure 5.18 a) , six arrows are drawn on 6 vortices. These arrows indicate where these vortices will go when a current of **I**=5mA is applied to the sample. We further marked these cells in heavy black lines to indicate that a vortex was previously occupied. The question mark (?) indicates the region where the SQUID detector became unlocked. We could not identify the vortex pattern in this region. The circled region indicate a defect region of a vortex hopping between the two cell sites.

Analysis:

From studying images a) to i) in figure 5.18, we find that most vortices are pinned to the grids for the applied current up to 30mA. A current of 30mA applied to the sample supplies each wire in a network along the direction of current of 60μA. This value of current is not sufficient to depin a trapped vortex. The current required for depinning vortices in a uniform array is $i_d \equiv U_b/\Phi_o$. Using equation 3.19 and 3.20 and assuming $l/\xi >> 1$ ($l/\xi \sim 200$ for our sample), then $i_d = 0.4 i_c$, where i_c is the critical current of the niobium wire. From measurements, we estimated that i_c of niobium wire of width 2μm and thickness 0.8μm is about 10mA at T=7K. The depinning current therefore is about 4mA. For the values of current we applied to the sample, only a few vortices depinned. We suspect the reason we observed only a few vortices depinning at $i < 30\mu A$ is that the cells in these regions have weak links. These weak links are probably due to defects in the grids during fabrication. These defects may be niobium lines that have linewidth smaller than 2μm.

We found only 3 vortices (6% of trapped vortices) moved in the $-y$ direction (see e) and f)) as the applied current in the $+x$ direction is increased from 0mA to 30mA. This is the expected behavior due to the Lorentz force. Reversing the current from 0mA

to -20mA causes only two vortices to move in the +y direction. One of these vortices, which is encircled in all images a) to i), is observed to hop back and forth between two cells. This suggests that the vortex potential is not symmetric in the y-direction. This asymmetry is probably caused by interactions of nearby vortices. Figure 5.19 shows the potential seen by a vortex in the circled region of the images. The barrier heights are obtained when the vortex is observed to hop into adjacent cell. Away from these two cells, the barrier heights along the y direction are huge and hopping over these barriers are prohibited for $i < (0.4)i_c$=4mA.

To our surprise, we also observed formation and annihilation of vortex-antivortex pairs as the array is injected with current (images b) and e)). Vortex-antivortex pairs have been predicted to nucleate in a superconducting sample at 'hot spots' regions[10] of high temperature or regions of defects[11] in the presence of a bias current, figure 5.20. We have not only detected this process but also seen vortex-antivortex pairs created along the direction of current as shown in figure 5.21. A vortex-antivortex pair is always observed to nucleate next to a pinned vortex. This pair is arranged such that the antivortex is sitting next to the pinned vortex. Besides 'hot spots' and defect sites, we suspect that pinned vortex also forms a favorable site for nucleation (by causing distortion of the current) of a vortex-antivortex pair when a current is applied to the array.

Besides vortices hopping perpendicular (y direction) to the applied current, some vortices are observed to travel along the x direction, both against and with the flow of current. The cause for vortices to move along the axis of current is unclear, but our simulations of clusters of asymmetric barrier heights, have given us some clue to this effect. In the simulation, we sometime observe a vortex travel in the axis of current because of lower barrier height (due to defect) before hopping into adjacent cell as shown in figure 5.22. Vortex interactions are also important in this process. We noticed that a

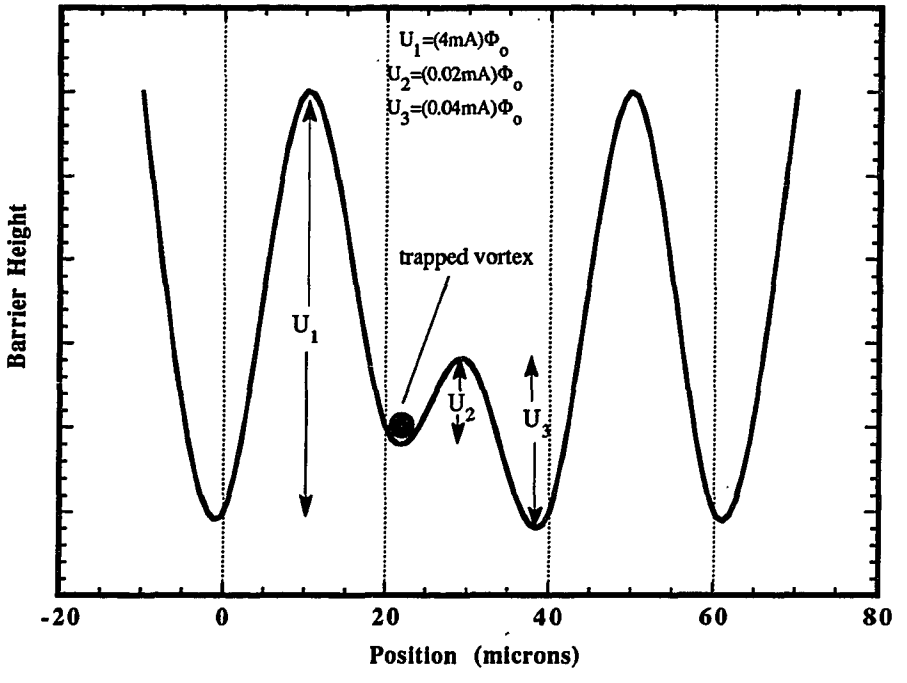

Figure 5.19 : Vortex potential seen by a trapped vortex encircled in the images a) to i) of figure 5.18.

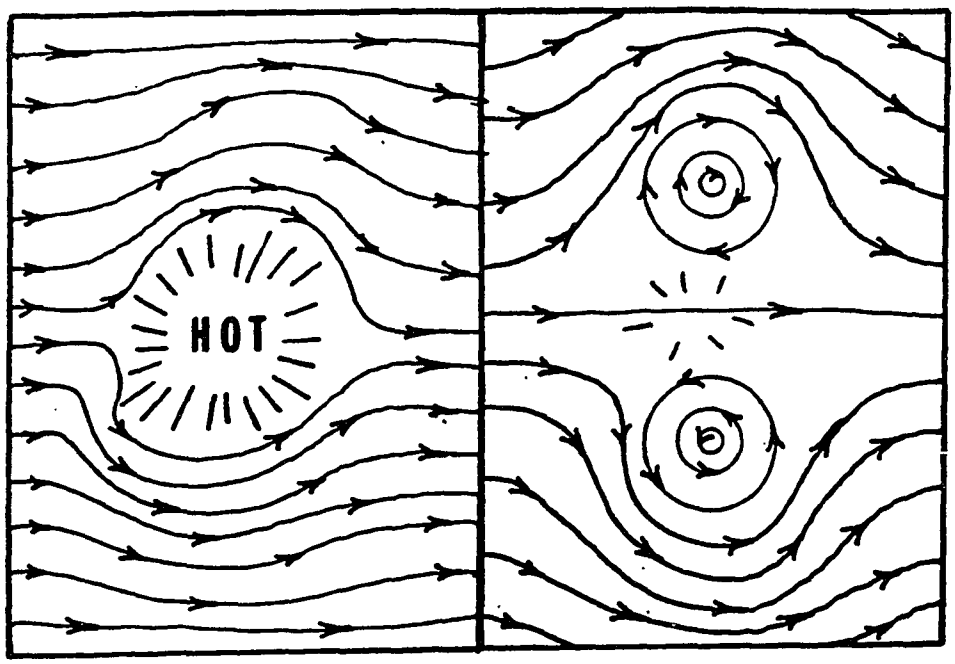

Figure 5.20 : Vortex-antivortex pair has been predicted to nucleate in superconducting films or arrays in a presence of a current in regions of defects or high temperature.

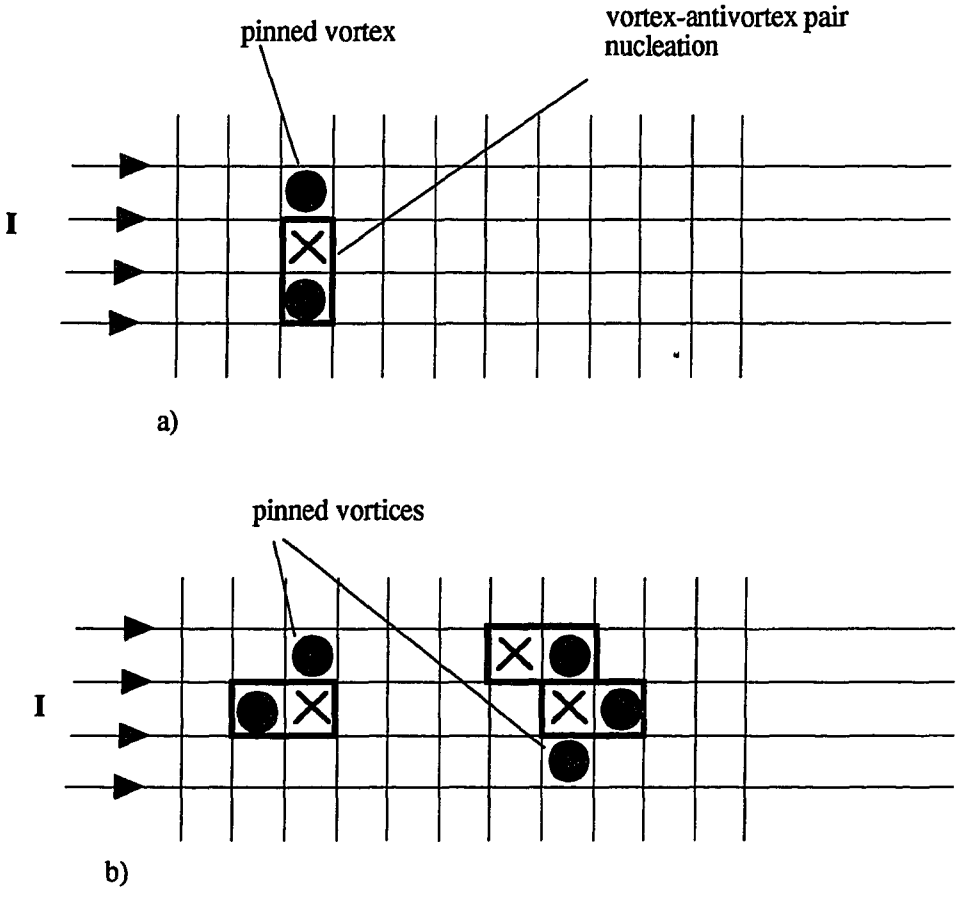

Figure 5.21 Nucleation of vortex-antivortex pairs has been observed as current is applied to the array. Scenarios a) and b) have been observed. Process a) has been predicted while process b) is due to pinned vortex-antivortex interaction.

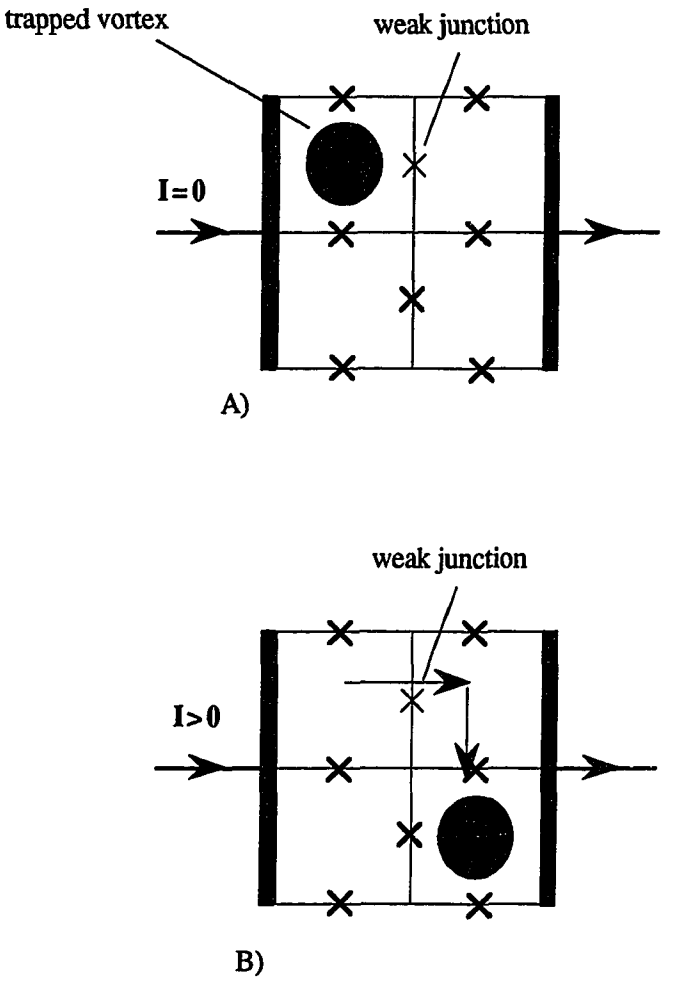

Figure 5.22 A) A trapped vortex in a 2x2 Josephson junction cluster with one weak junction. B) As current is injected into the cluster, a trapped vortex sometime moves in the axis of current over a weak link before hopping to the adjacent cell by the Lorentz force.

vortex has a tendency to move away from a nearby vortex when a current is applied. Several of these events have been observed and are illustrated in figure 5.23.

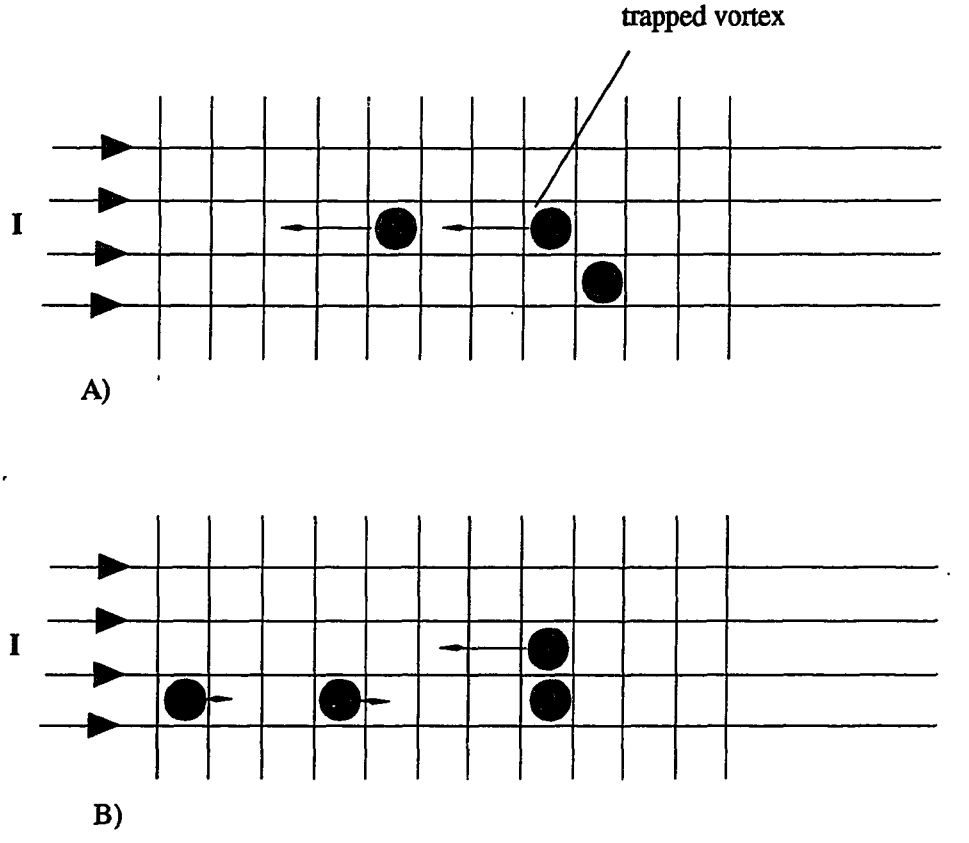

Figure 5.23 Several possible events of vortices moving along the axis of current are shown above which have been observed. The reason for this process is probably due to vortex interactions and defects in the grids.

References

1. A. M. Chang, H. Allen, L. Harriott, H. Hess, H. Kao, J. Kwo, R. Miller, R. Wolfe, J. van der Ziel, and T. Chang, "Scanning Hall Probe Microscopy". *Appl. Phys. Lett.* **61**, 1974-1976 (1992).

2. S. Teitel and C. Jayaprakash, "Josephson-Junction Arrays in Transverse Magnetic Fields". *Phys. Rev. Lett.* **51**, 1999-2002 (1983).

3. Wan Y. Shih and D. Stroud, "Molecular-Field Approximation for Josephson-Coupled Superconducting Arrays in a Magnetic Field". *Phys. Rev. B* **28**, 6575-6577 (1983).

4. Thomas C. Halsey, "Josephson-Junction Arrays in Transverse Magnetic Fields: Ground States and Critical Currents". *Phys. Rev. B* **31**, 5728-5745 (1985).

5. Thomas C. Halsey, "Josephson-Junction Array in an Irrational Field: A Superconducting Glass?". *Phys. Rev. Lett.* **55**, 1018 (1985).

6. Fang Yu's Thesis, "Superconducting Phase Transition of Artificial Wire Networks".

7. J. M. Kosterlitz and D. J. Thouless, "Ordering, Metastability and Phase Transitions in Two-Dimensional Systems". *J. Phys. C* **6**, 1181 (1973).

8. H. S. J. van der Zant, M. N. Webster, J. Romijn, and J. E. Mooij, "Phase Fluctuations in Two-Dimensional Superconducting Weakly Coupled Wire Networks". *Phys. Rev. B* **42**, 2647 (1990).

9. S. Rao and Van Harlingen, "Effects of Disorder in Proximity Coupled Clusters", sumitted to *Phys. Rev. B.*

10. A. M. Kadin, M. Leung, A. D. Smith, and J. M. Murduck, "Photofluxonic Detection: A New Mechanism for Infrared Detection in Superconducting Thin Films". *Appl. Phys. Lett.* **57**, 2847 (1990).

11. Y. Cai, P. L. Leath, and Z. Yu, "Simulation of Below-Gap Photoresponse of Thin Film Superconductors by Josephson Junction Arrays". (submitted to *Phys. Rev. B* 1993)

Chapter 6

Conclusions and Future Directions

In conclusion, we have built a novel instrument which we call it the Scanning SQUID Microscope (SSM) to observe magnetic vortices in niobium networks. At values of rational f in a large square network, we confirmed the theory that vortices align in a lattice that is commensurate with the underlying array lattice. For rational values of f lower than 1/3, vortex interactions at large separation are weak and effect of disorder increases. As f approaches an irrational number, vortices align randomly and never achieve ground state configurations.

Our experiments on clusters provide a simple and elegant way of understanding the physics of vortices in clusters in terms of statistical processes. The experiment also supports the 'single vortex model' which is used in interpreting the resistance data in arrays. Modeling of networks by Josephson junction arrays proved to be somewhat successful. The discrepancies suggest that a more complex model is needed.

Our results on dynamics of vortices in arrays are preliminary. It seems most of our observations are due to inhomogeneity in the network. It is clear that a system of lower barrier heights than networks is needed to study vortex dynamics. Weakly-coupled arrays offer such characteristics. Because of temperature constraint in the SSM1, Josephson junction arrays cannot be studied at this point and have to wait until the completion of the SSM2.

The experiments we have shown in this thesis are only a few examples of the many possible experiments for understanding the physics of arrays. The physics of the array is complex and many more experiments need to be done before a comprehensive model of the array can be obtained.

Besides detecting vortices in superconductor networks, the SSM is a powerful tool

for imaging ferromagnetic and diamagnetic samples non-invasively. In the ferromagnetic mode, the SQUID can directly detect the permanent fields of the sample. For diamagnetic materials, the modulating field of the SQUID interacts with the diamagnetic object to give the image. In both modes, the field sensitivity is determined by the SQUID. The spatial resolution, on the other hand, is determined by how small the SQUID loop can be fabricated and how close the SQUID is scanned over a sample. Our SQUID design is aimed at ~ 10μm spatial resolution. At this resolution, we cannot look at magnetic domains (usually of size submicrons) in ferromagnetic materials but we can look at larger features which give details about grain boundaries and defects.

The ultimate spatial resolution of the SSM is probably about 2μm. To look at vortices in high T_c films we need a sensitive magnetic detector of spatial resolution of at least 0.1μm x 0.1μm. We have begun to develop a similar instrument to the SSM which can achieve such resolution. In this instrument, a submicron junction (size ~0.1μm x 0.1μm) is scanned at a distance of 0.1μm above the sample to image trapped vortices in superconducting thin films. The junction can operate in a flux-locked mode similar to a dc SQUID and achieve the same field sensitivity as a SQUID. The scanning mechanism is a combination of stepping motors and piezo-tube. We call this technique the Scanning Junction Microscope, SJM. We will reserve this topic for a later thesis, which will be done by Mark Wistrom.

Vita

Lan Vu was born on June 21, 1966 in Saigon, Vietnam. He immigrated to United States in 1975 and resided in Texas. Upon graduating from Newman Smith High School in Carrollton, TX in 1984 he attended The University of Texas at Austin. He received his B.S. in physics at Texas in 1987 and continued his graduate school at State University of New York at Stony Brook. He transferred to University of Illinois at Urbana-Champaign in 1988. In 1990 he received his M.S. degree in physics at Illinois and finished his Ph.D. three years later.